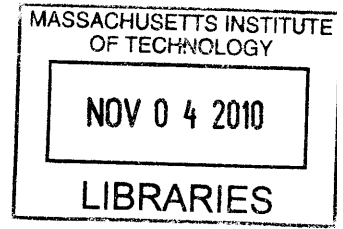# Modeling and Simulation of an All Electric Ship in Random Seas

by

Kyle Schmitt

B.S., University of Wisconsin - Madison (2008)

Submitted to the Department of Mechanical Engineering
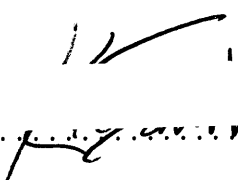in partial fulfillment of the requirements for the degree of

Master of Science in Mechanical Engineering

at the

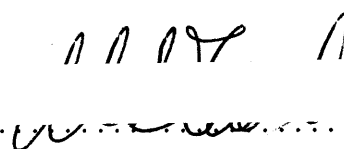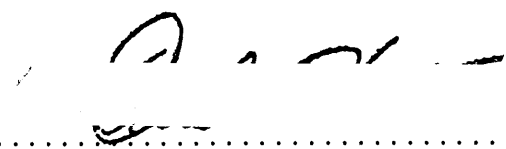MASSACHUSETTS INSTITUTE OF TECHNOLOGY

September 2010

Author . . . .
Department of Mechanical Engineering
August 13, 2010

Certified by. . . . .
Michael Triantafyllou
William I. Koch Professor of Marine Technology
Thesis Supervisor

Accepted by . . . .
David E. Hardt
Chairman, Committee on Graduate Students

Modeling and Simulation of an All Electric Ship

in Random Seas

by

Kyle Schmitt

Abstract

This Masters thesis, conducted in support of the All Electric Ship (AES) early design effort, presents two computational programs for analysis and simulation: a full-scale, end-to-end AES simulator and an analytical performance and stability assessment tool for the ship's propulsion drive; the integrated power system (IPS).

The AES simulator incorporates high order techniques for the hull modeling with low order, low effort models for the propellers, IPS, and prime movers, culminating in a fully-coupled, end-to-end, simulation environment, which is still practical for high effort studies like uncertainty quantification or optimization. The most appealing characteristic of this program is the time domain hull model with combines nonlinear maneuvering equations, seakeeping equations, and second order wave force equations. This allows for the prediction of propeller elevation and inflow velocity in random seas, and effectively the high fidelity modeling of propeller load schedules. This capability is vital for AES design where propeller load fluctuations can lead to large electrical power transients onboard.

To demonstrate the capability of the AES simulator, ship trails are run in calm and random seas. IPS state evolutions are given to show the propagation of load disturbances. Monte Carlo methods are applied to assess transients in the inherently random sea environment.

The IPS assessment tool attempts analytical quantification of the performance and stability of the Purdue MVDC Testbed, a scaled IPS composed of analagous elements: electric machinery, power converters, MVDC distribution, and bus voltage/induction motor torque control schemes. The thesis details the applicable nonlinear equations and the tools for identifying system equilibrium points. Then, small displacement theory is used to attain linear state space matrices valid near the operating points, from which traditional stability and performance techniques can be applied. Methods for closed loop analysis are suggested including ways to assess the hysteretic control elements used for induction motor torque control. Results from experiments with the high fidelity, high effort, Purude MVDC Testbed model are used for validation.

Acknowledgments

My plenary acknowledgement and expression of thanks go to the MIT faculty and Sea Grant staff for investing in my work without question. I was truly blown away by the readiness of my superiors to aid in my endeavors. No matter the department, no matter the query, MIT faculty and staff were willing to address my needs duly and unfailingly. In specific, I would like to thank Michael Triantafyllou, Franz Hover, James Kirtley, Chryssostomos Chryssostomidis, Mirjana Marden, George Karniadakis, Julie Chalfant, Mark Welsh, and Trent Gooding for their technical guidance.

From an administration standpoint, I'd like to thank Michael Triantafyllou, Chryssostomos Chryssostomidis, and Franz Hover for keeping me on task and motivating new avenues for self-education and research. Prof. Triantafyllou and Chrys, without your immense patience and resolve, I could not have produced the work to follow. Prof. Hover, without your unique perspective, I could not have garnered nearly the same intellectual experience from my time at MIT.

Both in my lab group and outside of it, I am indebted to several MIT students for moral and technical support. I'd like to give special recognition to Brenden Englot for always allowing me to verbalize my ideas on a near daily basis and for supplementing them with his experience. I'd also like Ilkay Erselscan for his infinite patience, help, and kindness during the development of my seakeeping model. Additional recognition needs to be given to Charlie Ambler, Brendon Epps, Josh Taylor, Phil Menard, Steve Englebretson, Lynn Sarcione, and Kevin Cedrone.

Thank you to the Office of Naval Research for providing the financial means that fueled this thesis.

Finally, thank you to my parents Patrick and Peggy Schmitt for building on an already significant debt of gratitude. Without your unyielding support, I would not be the student, engineer, person, that I am today.

Contents

List of Figures

List of Tables

10

Chapter 1

Introduction

All the research presented in this Master's thesis is in support of the effort to bring an all electric naval fleet from conception to reality. This work focuses on computational approaches to early design that run in parallel with physical testing of scale models being conducted by collaborators nationwide.

The All Electric Ship (AES) typifies the chief aim for this research. It is characterized by an electrically driven propulsion element that is coupled to the onboard support systems and weaponry, together called the Integrated Power System (IPS). The main components of the general IPS are electric generators, power electronics, transmission lines, storage and filter elements, weaponry and radar, and drive elements, i.e. advanced induction motors or permanent magnetic motors [41].

Indeed, this paradigm of power system architecture has been actualized on ships of lesser magnitude for decades, but the AES that is referred to herein is one conceived and designed for implementation on cruisers and destroyers of the utmost level of scale, maneuverability, defense, and weapons technology, for example, in the United States, the CG(X) and the DDG or DD(X) models.

1.1 An Historical Introduction to the All Electric Ship

The history of the United States destroyer is marked by the tireless pursuit of excellence and innovation. It is this pursuit that has, in the last century, made the US Navy one of the most

dominant and technologically advanced forces in the world, ensuring the safety of our domestic borders, bestowing the power to intervene for peace overseas, and allowing for reconnaissance in nearly every major body of water. Still, as history has shown, the next great advancement is always right around the corner, and it is our obligation to get there first.

Of course, the United States has not always possessed a superior Navy [25]. The first great push for better US sea forces was a result of Alfred Mahan's affirmation of proper naval strategy in *The Influence of Sea Power on History*. Quickly after 1890, Mahan's ideas were adopted by the US; the government became engaged and proactive in the area of oceans science, and we never looked back.

The largest-to-date technological advance to ship propulsion came in 1897, with Parson's patent of the steam turbine. The rotating turbine mechanism superseded that of the reciprocating piston mechanism in terms of thermal efficiency and power-to-weight ratio and was adopted quickly thereafter. This change in power paradigm was a harbinger for the experimentation and research to be done in this area in the century to follow.

The first US destroyers, the Bainbridge-class, were commissioned in the opening years of the 20th century. Their displaced tonnage was about 500 tons (1/20 of today's generation) and onboard power about 6 MW. These earlier generations of destroyer were "conceived as a specialized and rather fragile auxiliary to the battle line, [but] grew into an invaluable general-purpose warship, known in both world wars for its combination of compactness, hitting power, and toughness" [25]. Today, the destroyer is perhaps the most critical element to the US Navy fleet, requiring an optimization of speed, maneuverability, defense/weaponry, endurance, and survivability.

The decade before and after World War I saw great advancements in destroyer technology. Some new ships, including the Paulding class, began burning oil instead of coal to bring down fuel tonnage onboard. Many designs called for more complicated drive systems, with multiple prime movers and two propellers, to increase the power capacity of the ship. This led to the first destroyers over 1,000 tons and the first destroyers with over 20 MW of power onboard, i.e. the Wickes and Clemson classes. With prime mover and drive system technology progressing, destroyer classes were reaching power levels of beyond 40 MW by the onset of WWII.

The advances to the destroyer following the war were mainly related to anti-submarine and anti-aircraft, resulting in the guided missile destroyer (DDG) class. The next major advancement to propulsion was the replacement of the steam engines with GE LM2500 gas turbines in the mid-1970s, first with two turbines on the FFG-7 class of frigate and
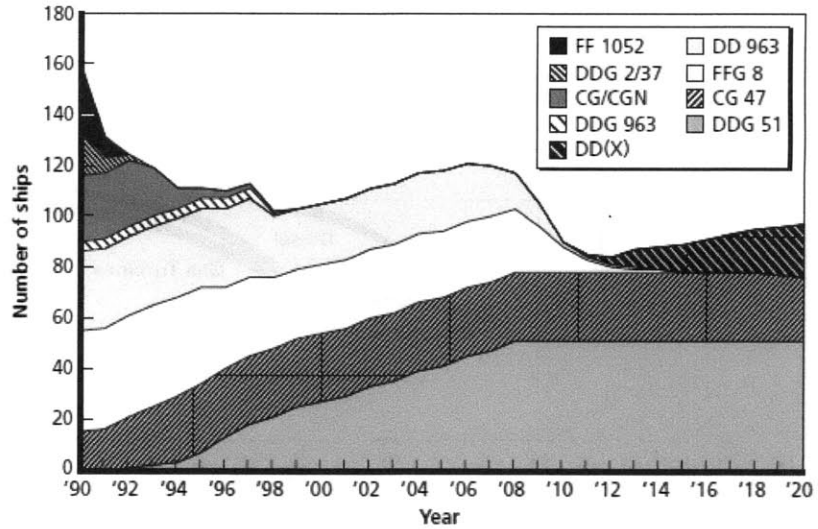
Figure 1-1: Recent past and near future composition of the surface combatant force [63].

subsequently 4 turbines on the Spruance class of destroyers. This resulted in approximately 15 % more thermal efficiency from the prime movers. The DDG with gas turbine propulsion is the current standard for US destroyers, as shown in Figure 1-1, but many other systems are investigated. Hybridization is a popular choice for smaller craft, allowing for high prime mover efficiencies over the ships entire performance range, see Figure 1-2. Several viable permutations of steam, gas, diesel, nuclear, and even electric, have been implemented for propulsion on naval craft, but have yet to be installed on a DDG class warship.

In the last decade, an All Electric Ship has been widely accepted as the next propulsion paradigm for the US destroyer due to the preponderance of advantages discussed in the subsection to follow. Prof. Welsh, Director of the Naval Construction and Engineering program at MIT, said he does see the AES as the inevitable next step in ship propulsion due to the improved efficiency and the increased power availability for weapons and radar [73]. "As a result, the Office of Naval Research established the Electric Ship Research and Development Consortium in 2002 to stimulate a multidisciplinary approach to the electric naval force system complexity, and to develop the necessary tools for the complex system design and engineering to reduce the risk and costs of early decisions" [19].

Engine Output Power vs. efficiency chart
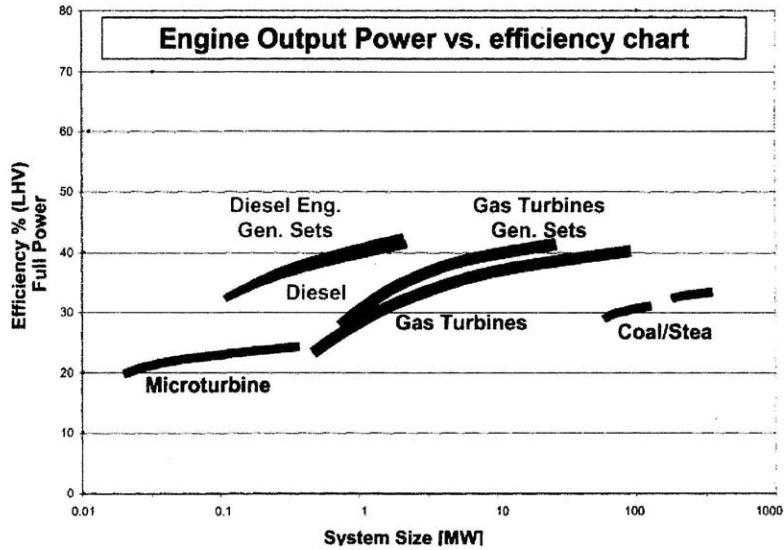
Figure 1-2: Thermal efficiency vs. size for several options of propulsion power [66].

1.1.1 Advantages and Challenges

The AES presents several important opportunities for overall ship improvement, though they are accompanied by unique challenges as well. The aim of the Electric Ship Research and Development Consortium [ESRDC] is to address the challenges while allowing the advantages to flourish.

Advantages	Challenges
-Higher Fuel Efficiency	-Increased System Complexity
-More Power Available	-Increased External Load Uncertainty
-More Powerful Weaponry and Radar	-Increased Weight
-Improved Survivability	-Increased Construction Cost
-Improved Volume Capacity	-Thermal Management
-Improved Life Cycle Costs	-Louder Electromagnetic Signature
-Quieter Acoustic Signature	

Table 1.1: Key advantages and challenges of the AES.

Perhaps, the number one reason for the change in propulsion paradigm are the efficiency gains that inherently come with it. The versatility of the multi-generator power plant and electrical distribution/storage allows for better efficiencies at nearly any point in the ship's operating range. A Navy study in 2001 projected 10-25 % better fuel consumption for the AES ship over an aggregate campaign [63].

14

The AES also increases the onboard electrical power potential and will allow for large capacitors able to store unprecedented levels of electrical energy with fast or slow release. These elements will make next-generation weaponry (like rail guns and high energy lasers) and next-generation radar (requiring up to 10 times the electrical power necessitated by its predecessor [73]) a reality. The AES must be realized before these systems can function at sea.

Other advantages of the AES include increased volume capacity, a new tier of ship survivability, and improved overhead costs.

The overarching challenge when imagining the AES is the extraordinary system complexity it will require to accommodate for the scale, the distributed generation and the uncertain loading [11]. Early AES designs involve a highly intricate and inter-connected IPS, which will be managing 60-80 MW of power at cruising speeds. At a system level, this effort will require an optimized distribution and communications topology, a carefully planned grounding configuration, harmonic mitigation, orchestrated control systems, and redundancies/backup systems in place in the case of emergency. At the component level, engineers face the hurdle of designing motors and power electronics robust enough to manage the huge power levels and transients onboard while incorporating cutting edge technologies like nuclear and fuel cell power, inventive energy harvesting techniques and new age weaponry and defense systems.

The penultimate challenge arises from the coupling between the propellers and the shipboard systems. The AES design must take into account the effects of propeller load transients on the IPS and, likewise, the effects of pulse power loads onboard on the propulsion. Designs for control and filtering must buffer the propulsion effects from the distribution bus. At its core, this thesis addresses this challenge.

Other significant challenges include cost, weight, qualification and thermal management.

1.2   Current Focus Areas for AES Research

All ESRDC members meet every May to present work and coordinate efforts for the following year [21]. The current focus areas presented in Figure 1-3 reflect the latest consortium meeting.

Generally speaking, the largest area of current effort is the conceptualization and selection

Computational Analysis*	Physical Testing
-Component and system level models*	-UT Center for Electromechanics
-Rapid model generation	-FSU Center for Advanced Power Sys.
-New integration techniques	-Purude MVDC Testbed
-Multivariable and multi-objective optimization methods	-USC Power Routing Lab
	-MSU High Voltage Laboratory
-Uncertainty and sensitivity analysis*	-MIT Test Tank and Marine Robotics Lab

I. Architecture Considerations
-MVDC,MVAC,HVAC distribution

-System topology*
-Reconfiguration
-Grounding
-Converter, filter, and switch placement

II. Component Level Analysis
-Generator and motor cost/weight optimization
-Design of lighter high power components
-Bidirectional motor for energy harvesting during braking

III. Stability & Control*
-System stability analysis*
-Adaptive control
-Inter-converter control
-Reduction of impact of propeller load changes and pulse power

IV. Diagnostics
-Communication
-Fault detection methods
-Non-intrusive sensing

V. Thermal Management

-Finite element thermal ship simulation and visualization
-Innovative heat removal and cooling

Figure 1-3: Current focus areas in AES development. The asterisks designate areas of research directly related to the work presented in this Master's thesis.

of the optimal electrical distribution network. There still exist many different schools of thought on even the most top-level architecture and topology decisions: AC or DC distribution, medium (5-6 kV) or high voltage distribution, and number of generators/induction motors. To complicate things, the set of metrics (and the weighted importance of each) used to assess different designs is not set in stone. The AES simulator presented in this paper uses a four generator split plant topology with MVDC distribution [15], see Figure 2-1.

The other general areas of research are power system components, stability and control, diagnostics, and thermal management.

To the direct interest of this Master's thesis, several universities are developing full computational models of the IPS for use in simulation and analysis. Models are developed in Matlab & Simulink and PSCAD, often calling subroutines in ship analysis tools like Paramarine. For example, members of MIT Sea Grant have conducted sensitivity analysis on a high fidelity 19 MW IPS model to quantify the effects of extreme events like propeller emergence and pulse power weapons [59], members from CAPS at FSU have built a real time digital

simulator (RTDS) electric ship model [3], and members at USC are working on a program for the rapid evaluation of user-defined IPS topologies [16]. Because of the abundance of electrical engineers in the ESRDC, these models often fall short on the modeling of the prime mover, propeller, and ship motion; often, constant assumptions or proxies are used in place of high fidelity hydrodynamic simulation. A second criticism of IPS models are their long runtimes due to the level of detail of the electrical component models. These criticisms are attended to by the work presented in this Masters thesis.

The hydrodynamic simulator presented in this thesis combines nonlinear maneuvering equations with seakeeping equations, culminating in a 6 degree of freedom (6DOF), time domain ship motion simulator. Programs like ASSET [55] and Paramarine are robust analysis tools for ship design, but cannot to the author's knowledge, conduct event-type time domain simulations in 6DOF, in random seaways. LAMP and SWAN are commercial, three dimensional, time domain ship simulators, but have gained little popularity due to their long computation times [48]. Perhaps, [22] gives the best presentation of a framework for unified time domain nonlinear ship simulation in 6DOF; some of its ideas, including the superposition of low frequency and high frequency motions, are leveraged in this thesis. To the author's knowledge, however, the program presented in this thesis is the first end-to-end AES simulator with high fidelity 6DOF hydrodynamic subroutines.

Another direction of research intimately tied to this thesis is the system level stability analysis of the IPS being approached by several universities. Approaches vary from linearization and traditional tools [43], [35], continuation power flow [10], immittance based stability tests [68] and large-signal stability with Lyapunov theory [45].

1.3 Thesis Deliverables

The statement of deliverables for this thesis is twofold. The first deliverable is a program for computational AES simulation and analysis. The second deliverable is a program for the stability analysis of the MVDC IPS.

1.3.1 AES Simulator

The AES simulator is built in MATLAB & Simulink with Fortran subroutines. The model is conceived with three objectives: true end-to-end functionality, simplification of the IPS model where plausible, and modularity. The product of this research is a novel, fast AES time domain simulator capable of predicting, for instance, prime mover fuel consumption for a ship in a random sea environment, or power bus fluctuation during execution of low radius turn.

The ESRDC has produced dozens of useful IPS models, some of immense detail, for analyses including event simulation, design optimization, and stability analysis. However, because of the disciplinary make-up of the ESRDC, few of the current models succeed in incorporating a scheme to access propeller loading in a high fidelity way, as a function of ship motion and wave elevation. Instead, analyses either use 1) a constant speed assumption for the turbine and propeller shafts, or 2) first order propeller load proxies (step or hat functions). The emphasis of the work presented in this thesis is the inclusion of propeller, rudder, and hull hydrodynamics in an AES model. At the latest ESRDC meeting, in May 2010, Robert Hebner, Director of the Center for Electromechanics at The University of Texas at Austin, applauded these efforts and espoused their growing importance.

IPS models available through the ESRDC exchange tend to offer extremely high fidelity capabilities, at the expense of runtime and storage proficiency. For example, simulation of the Purdue Testbed computational model, a scale model of the AES IPS, for 10 seconds in Simulink rapid accelerator mode, on the author s Dell M1530 laptop, requires about 25 minutes and a 1.6e6 entry vector for each state (compared to other models, the Purdue Testbed model is small since it only includes the propulsion subsystem). Runtimes of this magnitude, or even one order less, are unacceptable for real time simulation and analyses where multiple simulations are required, namely optimization procedures. For this reason, simplification of the IPS component models is one of the goals of this work. High order, complex, models have been replaced with representative, reduced order models. The result is a much more rapid, less stiff, IPS simulator which still allows for accurate propagation of information across the system true to second-order effects including power conservation.

The program, in its default state, is composed of low order IPS component models, a low order propeller model, and high order maneuvering/seakeeping models. The program,

arranged in Simulink with MATLAB and Fortran subroutines, is set up to allow for easy substitution of higher order models. With this in mind, Chapter 3 suggests higher order models for the prime mover and the propeller and Chapter 4 presents higher order IPS componentry models.

1.3.2 Performance and Stability Analysis of the IPS

The analysis tools presented in Chapter 4 of this thesis accompany an effort within the ES-RDC to assess the stability and performance of the IPS for a wide range of parameters and operating conditions. Stability is a major concern for the IPS because of the uncertain loading conditions imposed by propellers and the large power transients imposed by high power weapons. Furthermore, the magnitude of the power system makes the result of instability all the more catastrophic. The importance of a robust stability tool is due to the relatively large design space still being considered for AES implementation; the tool should be such that it can assess a wide range of conditions and identify the degree of stability of each, all in a timely manner.

The aim of work presented here is an analytical and fairly austere approach to analysis of an MVDC IPS. The model equations, while nonlinear, are time averaged and simplified where applicable. Small displacement theory is used to linearize the governing equations and extract the state space matrices about operating conditions at equilibrium. These matrices become the engineer's best friend for quick performance and stability analysis.

The IM includes hysteretic elements in its feedback control which complicate the problem. One method is introduced to assess the performance and stability for systems of this type. Results are encouraging.

1.4   Outline of Thesis

This thesis is organized into the following chapters:

- Chapter 2 presents the models used in the default program for the gas turbine prime mover, the IPS including a synchronous machine (SM), power electronics, an induction

19

motor (IM), and control systems, the propeller, and maneuvering/seakeeping models. The key contribution of Chapter 2 is a 6DOF time domain ship simulator.

- Chapter 3 presents higher order model alternatives for the prime mover and the propeller. This chapter is mostly a restatement of others' work, but it is included for the sake of completeness.

- Chapter 4 attempts performance and stability analyses of the Purude Testbed model, an example of a MVDC IPS. Small displacement theory is used to conduct the analyses about equilibrium points. The key contributions of Chapter 4 are validated open loop state space matrices as well as early closed loop analyses.

- Chapter 5 presents the simulation capabilities of the model presented in Chapter 2 including maneuvering and seakeeping trials in calm and random seaways.

- Chapter 6 summarizes the contributions of this thesis and suggests next steps for the programs presented.

Chapter 2

An End-to-End Model of the AES

In this chapter, the model components of the AES simulator are described in detail. A medium voltage, direct current (MVDC) distribution is used; this distribution type is one favored among ESRDC members [21]. Four LM2500 gas turbines provide approximately 80 MW of power, just as with present day destroyers. The AES model subcomponents are the prime movers, the IPS, the propeller, maneuvering, and seakeeping, see Figure 2-1. The two propellers receive power from independent plants; split plant operation [15]. The key advantage of such an arrangement is the redundancy provided in the event of damage. Each IPS submodel includes two 22 MW synchronous machine (SM) models, distribution and power electronic models, and a notional 38 MW IM model. Control systems are described to regulate turbine speed, bus voltage, IM speed, and ship heading/stability. The maneuvering model is specific to a hull shape resembling the DDG51. The seakeeping model is for arbitrary hull shapes.

Some results are shown to verify the models including a demonstration of power conservation across the IPS, in Chapter 5.

2.1 Gas Turbine Model

Many AES models assume a constant input speed to the electric generator obviating the need to model the prime mover. One of the incorporations here is simple gas turbine model to drive the SM. This way, the effects of propeller load changes on the gas turbines can be examined.

21
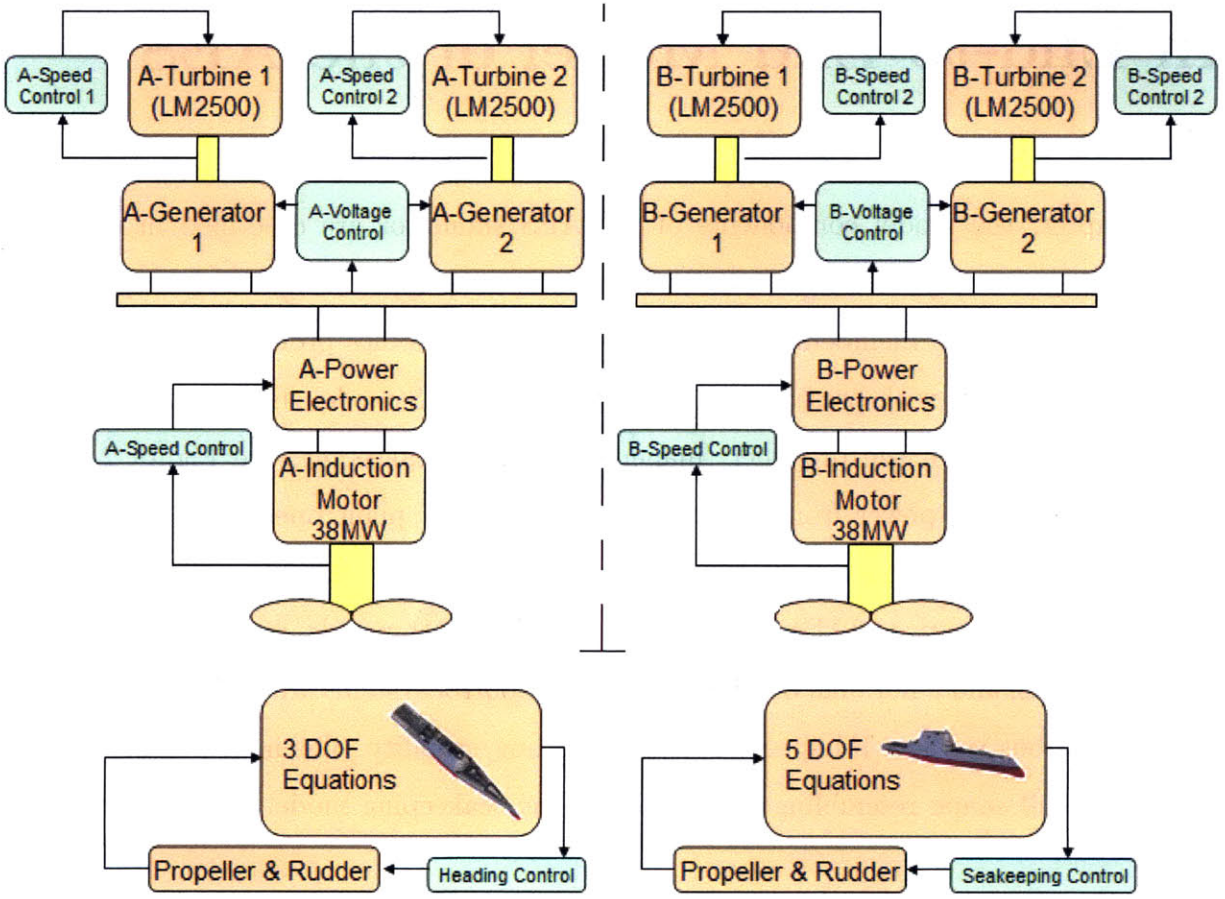
Figure 2-1: A schematic of the AES model presented in this thesis.

A first-generation GE LM2500 gas turbine model is used with rated maximum power output of 21.5 MW, a full-locking torque of approximately 123 kN-m (at full throttle), and a no-load speed of 6875 rpm (at full throttle) [26]. Torque input of gas turbine is linearly interpolated with the input shaft speed and fuel flow rate

$$Q_t = Q_{lock} \left[\frac{f}{f_{max}} (1 - \frac{n_t}{n_{t,max}}) \right] \tag{2.1}$$

where $\frac{f}{f_{max}}$ is the throttle ratio.

To maintain the turbine speed about $n_t^* = 60$ Hz, a discrete PI feedback control is used to actuate the throttle, with gains $K_{p,t}$ and $K_{i,t}$. A saturation limit, $0 < \frac{f}{f_{max}} \leq 1$, is imposed to represent machine bounds and a slew rate limiter, $|\frac{df}{dt}| \leq \Delta_t$, is imposed to prevent engine surge due to rapid changes in fuel flow rate.

This linear model is sufficient for predicting performance near an operating speed of 60 Hz. Nonlinear models account for thermodynamic and hydraulic states and can predict machine limitations, but this is not necessary for the studies conducted in this thesis. In [37], utilities are provided for the construction of a higher order turbine model. In [36], an experimentally derived, 23 state, optimally controlled jet turbine model is presented that may be applicable to shipboard power; this is discussed further in Chapter 3.

2.2 IPS Model

As discussed in Section 1.3.1, efforts were made to reduce the complexity and order of the IPS, while preserving the average dynamics of the propagation of energy from the propeller to the prime mover. Time averaged equivalent circuit models for the electric machinery have been drawn from [46]. The simulation for these equivalent circuits uses a quasi-steady approximation allowing for the use of steady-state sinusoidal analysis with complex impedances. For a ship system, with high inertia hydrodynamic states, this is well justified by the method of averaging [29]. *Note: the IPS model presented here is accurate only for dynamics with time constants approximately $\tau >> 0.01$. Also, all electrical model "states" do not exactly translate to reality, but are representative of the actual electrical states. Higher fidelity IPS component models are presented in Chapter 4.*

2.2.1 Synchronous Machine

The SM is modeled as an input voltage source, E_a, a stator resistance, R_{sg}, a stator winding inductance L_{sg}, and the separate excitement [46]. The separate excitement is modeled as a controllable DC voltage source, v_f, a field resistance, R_{fg}, and a field winding inductance, L_{fg}. The state equation for the excitement current is

$$\frac{di_f}{dt} = \frac{1}{L_{fg}}(v_f - i_f R_{fg}) \qquad (2.2)$$

The rms voltage inputted by a SM is widely defined as $E_a = M_g \omega i_f / \sqrt{2}$, where M_g is the mutual inductance of

Figure 2-2: Equivalent circuit (SM).

the generator windings, $\omega = \frac{P_g}{2}\omega_t$ is the electrical excitement frequency applied by the turbine, and i_f is the controlled field current. ω_t is the rotational speed of the turbine shaft, in units rad/s. The excitement voltage is actuated by a PI controller to maintain a desired bus voltage, with gains $K_{p,v}$ and $K_{i,v}$.

The SM produces torque opposing the shaft velocity both from friction and the electromotive force produced by the windings. This model uses a linear friction model, $Q_{fric} = \mu_1 + \mu_2 \omega_t$. The electromotive torque created by the generator is formulated to conserve power between mechanical to electrical domains,

$$Q_g = 3\frac{\mathrm{Re}\{E_a i_s^*\}}{\omega}, \qquad (2.3)$$

where the numerator represents the real (in-phase) power produced by all three phases of the SM.

Finally, the state equation for the turbine shaft angular velocity (with shaft inertia I_t) is

$$\frac{dn_t}{dt} = \frac{60}{2\pi I_t}(Q_t - (Q_{fric} + Q_g)) \tag{2.4}$$

2.2.2 Induction Motor

The IM is modeled as a power conservation device instead of explicitly deriving torque and magnetic flux [46]. The controllable inputs to the system are applied voltage, v_m, and excitement frequency, ω_e. The output of the system is motor torque, Q_m. The motor performance is a function of slip, $s = \frac{\omega_e - \omega_r}{\omega_e}$, where $\omega_r = \frac{P_m}{2}\omega_{rm}$

Figure 2-3: Equivalent Circuit (IM).

is rotor electrical speed . ω_{rm} is the angular velocity of the propeller shaft and P_m is the number of motor pole pairs. The equivalent circuit in Figure 2-3 represents the preceding by combining stator resistance, R_{sm}, and winding inductance, L_{sm}, with an air gap leakage inductance, L_m, in parallel with a rotor resistance, R_{rm}, a rotor winding inductance, L_{rm}, and a electromechanical "resistor," $R_{rm}\frac{1-s}{s}$. The "losses" in the electromechanical resistor are converted to mechanical power

$$Q_m = \frac{3\eta_m |I_r|^2 R_{rm}}{\omega_{rm}}. \tag{2.5}$$

where η_m is an efficiency term to factor in frictional or complex magnetic losses.

The current computation is done with sinusoidal steady-state analysis with general impedances defined $Z = R + j\omega L$ where R is a general resistance, L is a general inductance, and ω is a

Figure 2-4: Operation curves for a notional 38 MW IM with volts per Hertz control.

general frequency [46].

The state equation for the propeller shaft angular velocity is derived

$$\frac{dn_p}{dt} = \frac{60}{2\pi I_p}(Q_m - Q_p) \tag{2.6}$$

where I_p is the propeller moment of inertia and Q_p is the hydrodynamic torque discussed in Section 2.3.

$L_{sm} = 0.198$ mH	$L_{rm} = 0.330$ mH	$L_m = 11.74$ mH
$R_{sm} = 2.2$ mΩ	$R_{rm} = 3.4$ mΩ	P=12

Table 2.1: Electrical parameters for a 38 MW, 60 Hz, 4160 l-l voltage IM.

Table 2.1 gives the IM parameters for a notional 38 MW motor conceived and tested by Steven Englebretson, PhD., of the MIT Laboratory for Electromagnetic and Electronic Systems. A motor of this power capacity is envisioned for use on the first destroyers to be powered by the IPS. Operating curves for this motor are shown in Figure 2-4; note that slip regulation is to be used at high speeds to prevent operation beyond the IM rated power.

2.2.3 Rectification, Transmission, and Inversion Models

DC transmission between the SM and IM in the IPS is favored among ESRDC members due to its increased power capacity and reduction of transmission losses, among other things. The pitfall of such an architecture is the inclusion of costly power converters instead of low cost transformers. While an IPS architecture has not yet been rigidly defined within the ESRDC, it is the author's experience that the most convincing cases have been made for MVDC distribution. A MVDC architecture is used in this AES program.

In its simplest form, a MVDC transmission system is composed of a rectifier, inverter, and power storage element [52]. Additionally, auxiliary loads can be added onto the DC bus in parallel. Also, filter elements can be included to reduce the transmission of high order harmonics. The inverter is often composed of controllable switches in order to actuate applied voltage magnitude and frequency for the purposes of speed or torque control of the motor. Figure 2-5 shows a general MVDC model equipped with a three phase full-wave rectifier, and an inverter consisting of ideal switches (approximately attained with IGBTs).
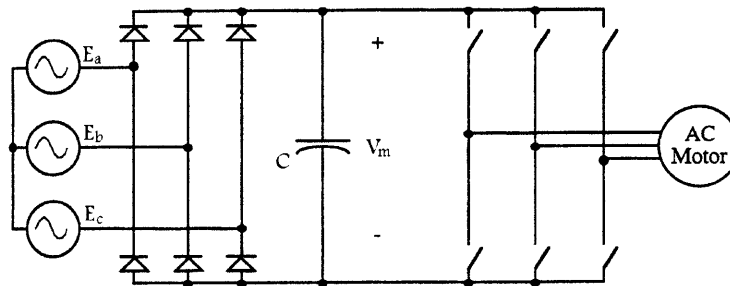
Figure 2-5: Traditional three phase rectifier-inverter [52].

Simulating this model in a high fidelity manner, with true AC states, requires an increase in computing effort between one and two orders of magnitude. For example, modern power converters are capable of thousands of ON/OFF cycles per second; modeling these effects can slow simulation beyond practical use. To maintain the simplicity of the IPS model while maintaining an acceptable level of fidelity, average models for the power converters, constrained to uphold power conservation, are used [40]. A schematic of the IPS model for this AES simulator is shown in Figure 2-6. The average rectifier model consists of diodes. The average inverter model consists of active IGBTs. A resistance, R_p, is added to the DC bus to add the

effect of losses due to notching. Note: The convention used in the below equations is that E_a is RMS and line-to-line.
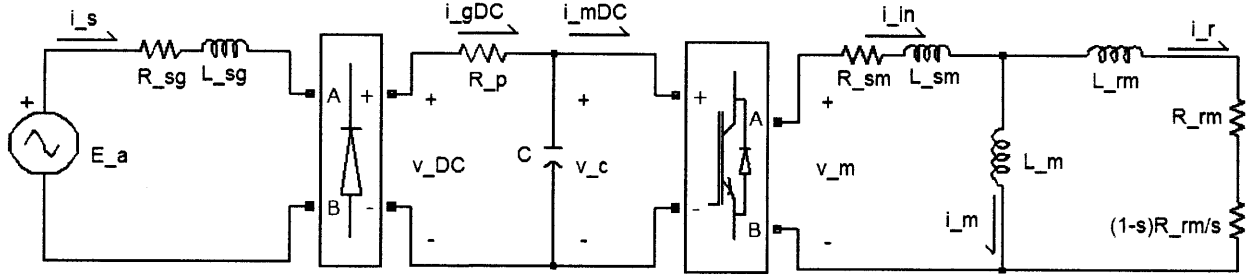
Figure 2-6: Schematic of lower order rectifier-inverter model.

The state equation for voltage across the power storage element, v_c, is

$$\frac{dv_c}{dt} = \frac{1}{C}(i_{gDC} - i_{mDC}). \tag{2.7}$$

If a zero firing angle is assumed, the average DC voltage output of a rectifier can be approximated as

$$v_{DC} = \frac{3}{\pi}\sqrt{6}E_a - \frac{3}{\pi}X_{co}i_{gDC} \tag{2.8}$$

where X_{co} is the commuting reactance of the device [57].

The DC current out of the rectifier, i_{gDC}, is found by applying KVL to the loop containing the rectifier and the capacitor:

$$i_{gDC} = \frac{v_{DC} - v_c}{R_p}. \tag{2.9}$$

The inverter DC current, i_{mDC}, can be found by asserting power conservation across the inverter resulting in

$$i_{mDC} = \frac{3\text{Re}\left\{v_m i_{in}^*\right\}}{v_c} \tag{2.10}$$

where i_{in} is the AC current out of the inverter, to the IM.

Last, power conservation can be added across the rectifier to compute i_s: $\text{Re}\left\{3(E_a i_s^* - R_p i_s)\right\} = v_{DC} i_{gDC}$.

28

Note: this model effectively propagates power demands of the motor to the IPS but does not accurately predict the propagation of IPS loads, like pulse power, to the motor. Essentially, the motor always gets the power it wants, dictated by the volts per Hertz control. The resulting required motor power is then propagated back on the IPS by Eq. 2.10. To allow propagation the other way, a higher order inverter model is necessitated though this is the most computationally expensive element in all of AES simulation. A clever approximation used here is to add a dynamic saturation to the motor voltage such that the power drawn cannot exceed the power available on the right side of the capacitor.

2.2.4 Volts per Hertz IM Control

The actuation of voltage magnitude and frequency by the inverter will likely be achieved with hysteresis control. It will be assumed that the switching of the controlled inverter is orders faster than the IM bandwidth. In this case, the average output from the perspective of the IM can be approximated by a smooth sine wave with a commanded voltage magnitude v_m and command frequency ω_e. The control strategy for selecting v_m and ω_e is introduced here.

A volts per Hertz control strategy is used [52]. In this procedure, ω_e is computed using PI feedback control of the IM rotor speed. v_m is then selected to achieve a constant ratio $\frac{v_m}{\omega_e}$.

In greater detail, the command slip speed to the IM, ω_s, is actuated with PI control based on the rotor velocity error, $\omega_r^* - \omega_r$, where ω_r^* is the target electrical speed for the rotor. The excitement frequency delivered to the motor by the rapidly switching inverter is the sum of the rotor speed and the slip speed command $\omega_e = \omega_r + \omega_s$.

Dynamic saturation is added to prevent the controlled slip speed, ω_s, from becoming greater than $\omega_{s,max}$, the slip at which the IM torque output peaks. This measure is taken to keep the control in the monotonically increasing region of the IM torque-slip relationship. An inline numerical solver is required to solve for $\omega_{s,max}$ at different rotor speeds. Additional saturation is added at high speeds to prevent power transmission across the IM greater than its rated 38 MW.

The applied voltage command is related to the excitement frequency linearly, $v_m = \frac{\omega_e}{\omega_{rated}} v_{rated}$ where ω_{rated} and v_{rated} are rated speed and voltage for the motor. This protocol is commonly employed in IM control and ensures a maximum magnetic flux and results in an identical

torque-speed curve for any excitement frequency, for a constant rotor speed. The schematic in the Figure 2-7 describes the entire protocol as a flow diagram.
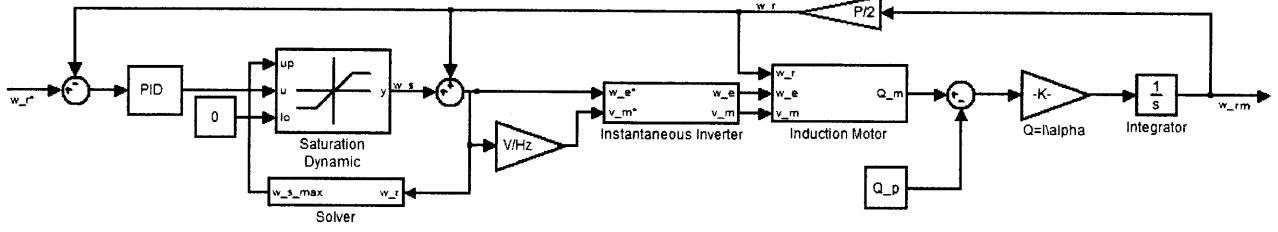
Figure 2-7: Volts per Hertz control protocol.

2.3 Propeller and Surge Model

An empirical, single quadrant propeller model is the current default for the AES simulator. Here, it is assumed that the ship is in forward motion and the propeller is rotating to create forward thrust. Data for a Wageningen B-class propeller is used [6]. In Section 3.2, a more advanced, less generic, propeller design program, OpenProp, is presented that considers approximately 20 different propeller parameters in the evaluation of the propeller performance.

Propeller thrust and torque, in deep and calm water, are modeled much the same way that lift and drag, respectively, are modeled for an airfoil [70]

$$
\begin{aligned}
T_{p0} &= k_T \rho n_p^2 D^4 \\
Q_{p0} &= k_Q \rho n_p^2 D^5 / \eta_R
\end{aligned}
\tag{2.11}
$$

where n_p is the propeller shaft angular velocity [Hz]. η_R is the empirically derived rotative efficiency of the propeller due to variations of the wake distribution and turbulence caused by the ship hull. The coefficients k_T and k_Q are the thrust and torque coefficients for the Wageningen B-class and can be uniquely interpolated from data given the pitch ratio of the

30

propeller and the dimensionless advance coefficient

$$J = \frac{u(1-w)}{n_p D} \qquad (2.12)$$

where u is the ship surge speed and $0 < w < 1$ is the experimentally derived wake fraction.

To account for shallow or disturbed water effects, loss coefficients can be introduced to Eqs. 2.11

$$
\begin{aligned}
T_p &= \beta_T k_T \rho n_p^2 D^4 \\
Q_p &= \beta_Q k_Q \rho n_p^2 D^5 / \eta_R.
\end{aligned}
\qquad (2.13)
$$

In [65] modeling techniques for losses occurring from inflow changes, cavitation, and out-of-water-effects, are presented. Inflow losses are considered by substituting V_a, the advance velocity, for u in Eq. 2.12. Traverse flow effects are not considered in the current version of the AES simulator.

Out-of-water effects are quantified by

$$\beta_{TA} = \text{Re}\left(1 - \frac{\arccos(h/R)}{\pi} + \frac{h/R}{\pi}\sqrt{1-(h/R)^2}\right). \qquad (2.14)$$

where h/R is the ratio of the hub distance to free distance and propeller radius.

Cavitation effects, for high propeller speeds, are hysteretic in nature because there is a delay in the collapse of ventilation funnel, the vanishing of air cavities on the propeller, and the build up of blade lift. The Wagner function of lift transience predicts that a foil must travel 20 chord lengths to recover its full lift; for a typical P/D=1 propeller, this is approximately 4 revolutions [56]. A rate limiter is imposed on the recovery of thrust to approximate the hysteretic behavior. The onset and offset of cavitation effects are taken to be $h/R = 1.3$ and $h/R = 1.1$, respectively. A common total cavitation loss, derived from experiments, is 70 % [65].

The thrust loss coefficient is computed by multiplying the loss effects $\beta_T = \beta_{TA}\beta_{TV}$. The

corresponding torque loss coefficient should always be larger than the thrust coefficient so efficiency is reduced; previous results show the relationship $\beta_Q = \beta_T^m$ is sufficient relation for $0 < m < 1$ [56]. For an open propeller, $m = 0.85$ has been applied with success. Figure 2-8 shows the propeller thrust/torque coefficients in a sample wave.
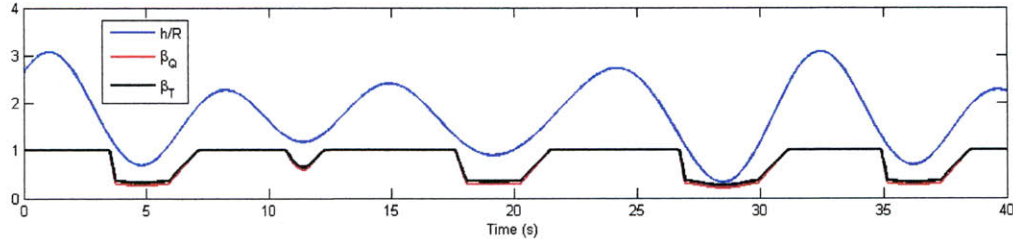
Figure 2-8: Demonstration of propeller loss model.

The hull/prop resistance, or fluid drag, has been studied to follow the relationship

$$R_{sp} = \frac{1}{2}\rho C_r A_w u^2 / (1 - t) \tag{2.15}$$

where C_r is an empirical parameter of the ship hull which is approximately a constant at the high value of Reynold's number common to ship travel, A_w is the wetted area of the ship, and t is the experimentally derived thrust deduction. With resistance computed our final state equation is

$$\frac{du}{dt} = \frac{1}{m + m_a}(T_p - R_{sp}) \tag{2.16}$$

where m is the ship mass and m_a is the mass of the entrained water.

2.4 Nonlinear Maneuvering Model

A marine vehicle experiences motions in six degrees of freedom. Employing notation and graphics from [23], these degrees of freedom are described in Table 2.2 and Figure 2-9.

Maneuvering refers to the study of large amplitude motion of a ship in calm seas. Traditionally, heave, roll, and pitch are not considered in maneuvering equations due to their relatively low excitement in calm seas; only planar motions are factored in. Maneuvering dynamics are distinctly slower than the other variety of ship motions - seakeeping - to be ad-

DOF		Forces and Moments	Body-Fixed Velocities	Inertial Positions and Euler Angles
1	motions in x-direction (surge)	X	u	x
2	motions in y-direction (sway)	Y	v	y
3	motions in z-direction (heave)	Z	w	z
4	rotation about the x-axis (roll)	K	p	ϕ
5	rotation about the y-axis (pitch)	M	q	θ
6	rotation about the z-axis (yaw)	N	r	Ψ

Table 2.2: 6 DOF motion components for a marine vehicle
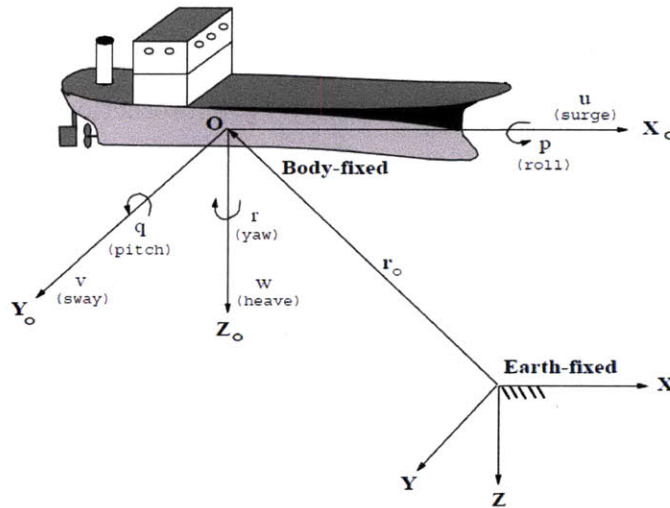
Figure 2-9: Body-fixed and earth-fixed reference frames [23].

dressed in the following section. Because maneuvering by definition is large amplitude motion, nonlinear viscous forces cannot be excluded from the equations of motion. Combined maneuvering equations of motion can be written with second-order, third-order or other nonlinear expansions of the hydrodynamic forces, for example the Abkowitz maneuvering models, [1]. Here Abkowitz's third order expansion about an operating speed u_0 we be used. Note that several terms have been left out due to symmetry and homogeneity assumptions.

$$m(\dot{u} - rv - x_{cg}r^2) = X_0 + X_{\dot{u}}\dot{u} + X_u\Delta u + X_{uu}\Delta u^2 + X_{uuu}\Delta u^3 \qquad (2.17)$$

$$+X_{vv}v^2 + X_{rr}r^2 + X_{vvu}v^2\Delta u + X_{rru}r^2\Delta u + X_{vr}vr + X_{vru}vr\Delta u$$

$$+F_x + \text{interaction terms}$$

$$m(\dot{v} + ru + x_{cg}\dot{r}) = Y_0 + Y_{0u}\Delta u + Y_{0uu}\Delta u^2 + Y_{\dot{v}}\dot{v} + Y_v v \qquad (2.18)$$

$$+Y_{vvv}v^3 + Y_{\dot{r}}\dot{r} + Y_r r + Y_{rrr}r^3 + Y_{vrr}vr^2 + Y_{vu}v\Delta u + Y_{vuu}v\Delta u^2$$

$$+Y_{rvv}rv^2 + Y_{ru}r\Delta u + Y_{ruu}r\Delta u^2 + F_y + \text{interaction terms}$$

$$I_z\dot{r} + mx_{cg}(\dot{v} + ru) = N_0 + N_{0u}\Delta u + N_{0uu}\Delta u^2 + N_{\dot{v}}\dot{v} + N_v v \qquad (2.19)$$

$$+N_{\dot{r}}\dot{r} + N_r r + N_{vvv}v^3 + N_{vrr}vr^2 + N_{vu}v\Delta u + N_{vuu}v\Delta u^2$$

$$+N_{rrr}r^3 + N_{rvv}rv^2 + N_{ru}r\Delta u + N_{ruu}r\Delta u^2 - x_pF_y + M_{add}$$

$$+\text{interaction terms}$$

$$(\Delta u \equiv u - u_0)$$

$F_x = T_p + F_{x,r} + F_{x,add}$ includes propulsion surge force, the rudder force in the longitudinal direction, added resistance from waves. $F_y = F_{y,r} + F_{y,add}$ includes the lateral rudder force and the drift force from waves. M_{add} is the drift moment from waves. The interaction terms represent the effects of non-bare hull elements like the propeller.

It is assumed that our body-fixed coordinate system has its origin at the planar center of mass and that there is not resistance to sway or yaw when $v = 0$ or $r = 0$, respectively (ie $Y_0 = N_0 = 0$). Interaction terms will be neglected. After manipulation, the equations can be

stately as a neat set of ODEs:

$$M \begin{bmatrix} \dot{u} \\ \dot{v} \\ \dot{r} \end{bmatrix} = \begin{bmatrix} f_1 \\ f_2 \\ f_3 \end{bmatrix} \tag{2.20}$$

where

$$M = \begin{bmatrix} m - X_{\dot{u}} & 0 & 0 \\ 0 & m - Y_{\dot{v}} & -Y_{\dot{r}} \\ 0 & -N_{\dot{v}} & I_z - N_{\dot{r}} \end{bmatrix} \tag{2.21}$$

and

$$f_1 = X_0 + X_u \Delta u + X_{uu} \Delta u^2 + X_{uuu} \Delta u^3 + X_{vv} v^2 + X_{rr} r^2 \tag{2.22}$$

$$+ X_{vvu} v^2 \Delta u + X_{rru} r^2 \Delta u + (m + X_{vr}) vr + X_{vru} vr \Delta u + F_x$$

$$f_2 = Y_{0u} \Delta u + Y_{0uu} \Delta u^2 + Y_v v + Y_{vvv} v^3 + (Y_r - mu) r + Y_{rrr} r^3 \tag{2.23}$$

$$+ Y_{vrr} vr^2 + Y_{vu} v \Delta u + Y_{vuu} v \Delta u^2 + Y_{rvv} rv^2 + Y_{ru} r \Delta u + Y_{ruu} r$$

$$\Delta u^2 + F_y$$

$$f_3 = N_{0u} \Delta u + N_{0uu} \Delta u^2 + N_v v + N_r r + N_{vvv} v^3 + N_{vrr} vr^2 \tag{2.24}$$

$$+ N_{vu} v \Delta u + N_{vuu} v \Delta u^2 + N_{rrr} r^3 + N_{rvv} rv^2 + N_{ru} r \Delta u + N_{ruu} r \Delta u^2$$

$$- x_p F_y + M_r.$$

No tractable analytical method exists for the calculation of the hydrodynamic coefficients. Each new hull shape must be tested experimentally to derive the coefficients. The most common approach for this purpose is to use a precision measurement machine (PMM). The coefficients used for this thesis's AES simulator were attained from PMM experimentation of

35

Surge	Value (10^{-5})	Sway	Value (10^{-5})	Yaw	Value (10^{-5})
$(X_{\dot{u}} - m)$	-646.9	$(Y_{\dot{v}} - m)$	-939.0	$N_{\dot{r}} - I_z$	-55.08
X_0	-65.01	Y_0	3.216	N_0	-6.813
X_u	-167.3	Y_{0u}	6.836	N_{0u}	-17.38
X_{uu}	-178.1	Y_{0uu}	3.590	N_{0uu}	-10.57
X_{uuu}	-80.78	$Y_{\dot{r}}$	-13.17	$N_{\dot{v}}$	16.85
$(X_{vr} + m)$	93.65	$(Y_r - mu)$	-381.6	N_v	-308.8
X_{vv}	-268.7	Y_{rr}	-156.8	N_{vvv}	-3857
X_{rr}	-101.58	Y_v	-124.6	N_r	-219.9
X_{vvu}	-496.4	Y_{vvv}	-39.94	N_{rrr}	-442.0
X_{rru}	-79.74	Y_{vvr}	-3704	N_{vvr}	-1666
X_{vru}	117.2	Y_{vrr}	-4580	N_{vrr}	-14820
		Y_{vu}	-2140	N_{vu}	-900.5
		Y_{vuu}	-1332	N_{vuu}	-671.1
		Y_{ru}	-543.5	N_{ru}	-607.0
		Y_{ruu}	-111.4	N_{ruu}	-561.8

Table 2.3: Non-dimensional hydrodynamic coefficients for third order Abkowitz expansion of DDG maneuvering model [67].

a 12'2" kayak (the Chesapeake Pro model by Wilderness Systems) by MIT's Jeff Stettler [67]. The coefficients were extracted for trials at u_0 =2.62 ft/s and u_0 =5.24 ft/s, or equivalently, preserving Froude similitude for a DDG51 hull at $u_0 = 11$ knots and u_0 =22 knots, respectively. In ship scale studies like this, Reynolds similitude is not preserved, though operation of the scale model in the turbulent region is essential; for the 22 knots test, $Re = 5.9e6$, conditions are safely in the turbulent region. The results for the 22 knots study will be used and are presented in Table 2.3.

Figure 2-10 shows a beam comparison of the kayak with the DDG51 model - the similarities are apparent. Also, the draft for each vessel is near-constant for the majority of the its length. In [51], this maneuvering model was implemented with coefficients from Stettler and the computational results were compared with DDG51 sea trials to draw the conclusion of model accuracy within 10-20 %. Certainly, the transom sterm of the DDG51 will cause conflicts with the kayak, and refinements could be made with a scale DDG51 model, but this is outside of the scope of this thesis.

The kinematic transformation to the global reference frame is
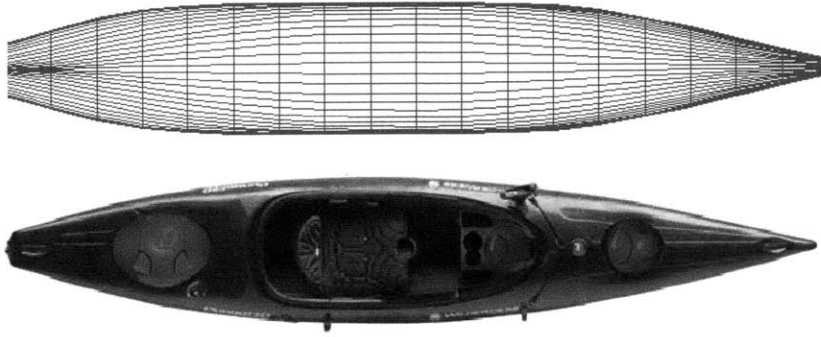
Figure 2-10: Beam comparison between DDG51 hull and Chesapeake Pro kayak.

$$
\begin{aligned}
\dot{x} &= u\cos\psi - v\sin\psi \tag{2.25}\\
\dot{y} &= u\sin\psi + v\cos\psi \\
\dot{\psi} &= r.
\end{aligned}
$$

The effective inflow velocity and angle are

$$
\begin{aligned}
V_a &= [u^2 + (v + x_p r)^2]^{1/2} \tag{2.26}\\
\alpha_a &= tan^{-1}\left(\frac{v + x_p r}{u}\right). \tag{2.27}
\end{aligned}
$$

where x_p is the distance from the body-fixed origin to the stern.

2.4.1 Rudder Model

The rudder is modeled with control surface theory. Notation is given in Figure 2-11. F_L is the lift force and is perpendicular to the inflow. Similarly, F_D is the drag force and is parallel to the inflow. Using a small angle of attack assumption, the lift and drag forces are

$$F_L = \frac{1}{2}\rho A_r V_a^2 C_L \text{ where } C_L = \frac{\partial C_L}{\partial \phi}(\alpha_a - \delta) \qquad (2.28)$$

$$F_D = \frac{1}{2}\rho A_r V_a^2 C_D \text{ where } C_D = \frac{\partial C_D}{\partial \phi}(\alpha_a - \delta)$$

where A is the area of the control surface and δ is the controlled angle of the control surface.

The lift gradient is approximated using [70]

$$\frac{\partial C_L}{\partial \phi} = \frac{1}{\frac{1}{2\pi\phi} + \frac{1}{\pi AR} + \frac{1}{2\pi AR^2}} \qquad (2.29)$$

where AR is the aspect ratio of the control surface. For No.1 rudder shape in [42], the lift gradient is 3.31 and the drag gradient, tested at a Reynold's number of 1.23e6, is 0.46.

Finally, the lift and drag forces can be converted to the body-fixed coordinate system

$$n = \text{sign}(\alpha_a - \delta) \qquad (2.30)$$

$$F_{x,r} = nF_L \sin\alpha_a - F_D \cos\alpha_a$$

$$F_{y,r} = -nF_L \cos\alpha_a - F_D \sin\alpha_a.$$
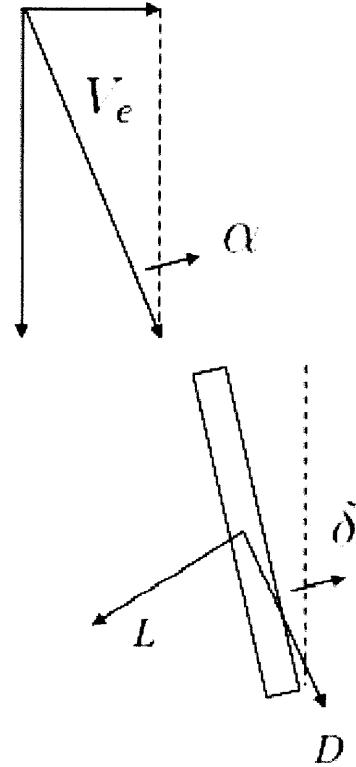
Figure 2-11: Rudder schematic.

In marine science, there is a focus on maneuvering control via rudder or azimuthing propulsor actuation [70], [28]. As a default, this AES simulator will employ saturated PID control of the rudder angle to meet a heading or to execute a maneuver. The saturation is added to prevent hydrodynamic stall around 20°. A swing rate limiter Δ_r is added to approximate added mass and damping of the rudder.

2.5 Time Domain Seakeeping Model

Seakeeping refers to the study of wave forces on an arbitrary body at sea and the subsequent motions of that body. The aim of a seakeeping program like the one developed here is the prediction of ship motions in regular sinusoidal waves and, using superposition [14], the prediction of responses in irregular waves. The primary attraction of a seakeeping program for AES analysis is that it allows the relative position of the propeller to be tracked during maneuvers in random seas. Then, employing the propeller loss model discussed in 2.3, the ship simulation can be coupled to the IPS through propeller loading.

Of course, in ship design, seakeeping performance is one of the most important considerations. In 1970, Salvesen, Tuck, and Faltinsen published a vital paper in the seakeeping field titled *Ship Motions and Sea Loads* [62] where they presented a new strip theory for seakeeping analysis that effectively made the problem analytically tractable and paved the way for the computational models still used today. Shortly after this paper, MIT combined their strip theory with conformal mapping techniques for the computation of hydrodynamic sectional coefficients, to develop a fully-capable frequency domain seakeeping program called MIT5D [47]. Recently, an MIT graduate student, Ilkay Erselcan, combined their strip theory with Frank's close-fit method [24] for the computation of hydrodynamic sectional coefficients, to develop a fully-capable frequency domain seakeeping program [20]. Between, [62], [47], and [20], the methodology employed in this thesis is covered in detail for first order seakeeping as well as roll damping. [61] presents a method for the computation of second-order wave effects including added resistance and drift forces.

Seakeeping is ordinarily presented as Newton's 2nd Law applied in 6DOF with the assumption that the responses are linear and harmonic; the Salvesen, Tuck, and Faltinsen notation will be used to represent the seakeeping states [η_2 = sway η_3 = heave η_4 = roll η_5 = pitch η_6 = yaw]. Seakeeping computation in the surge direction is neglected for long slender hull forms because the hydrodynamic seakeeping forces are much smaller than the viscous friction forces from maneuvering equations. The general equations of motion are

$$\sum_{k=2}^{6} [(M_{jk} + A_{jk})\ddot{\eta}_k + (B_{jk} + B_{j,v})\dot{\eta}_k + C_{jk}\eta_k] = \text{Re}\left\{F_j e^{i\omega t}\right\}; \quad j = 2...6 \qquad (2.31)$$

39

where M_{jk} are components of the generalized mass matrix, A_{jk} and B_{jk} are the added mass and damping (radiation) coefficients, $B_{j,v}$ are viscous damping coefficients, C_{jk} are the hydrostatic restoring coefficients, and F_j are the complex wave excitations. The jk notation indicates a force in the j direction due to motion or displacement in the k direction. The radiation coefficients and wave excitations are functions of wave frequency ω_0, ship speed U, and heading β. The ship experiences the forces with the encounter frequency

$$\omega = \omega_0 - kU \sin \beta \qquad (2.32)$$

where k is the wave number. For a linear system, the response frequencies should be the same as the wave encounter frequency.

Now a short description of each relevant force. Added mass accounts for the accelerated fluid that must be displaced for the body to accelerate; added damping accounts for the energy loss required to create free surface waves. Froude-Krylov force accounts for the pressure gradients most substantial in long waves; diffraction accounts for the forces required to disrupt a wave pattern most substantial in short waves. Viscous wave forces are ignored in ship seakeeping analysis because of the low relative amplitude of the waves. The restoring forces are due to buoyancy. All of the above forces are computed with potential theory discussed in Section 2.5.2. For seakeeping motions, viscous effects have been shown to be significant only in roll, for instance, friction and separation effects; these will be addressed in Section 2.5.2. Second-order wave forces for a surface ship are most important in surge, sway, and yaw and include a constant force as well as oscillatory wave interaction forces; in Section 2.5.4 it will be seen that these forces are added to the maneuvering equations as opposed to the seakeeping equations.

The subsections to follow present in some detail the subroutines of this thesis's time domain seakeeping program, including 1) the computation of sectional coefficients with MIT5D's conformal mapping techniques, 2) the use of strip theory to compute response amplitude operators (RAOs) in 5DOF, 3) the calculation of second-order forces, and 4) the generalization of the frequency domain results to time domain. Results are included in these sections to show correspondence with their parent papers' results.

2.5.1 Conformal Mapping

MIT5D, a seakeeping program written in the 1970s, is employed to compute the sectional coefficients using a conformal mapping technique for Lewis and Bulb forms. Though the section geometry for the conformal mapping technique is not as flexible as Frank's closed fit method, conformal mapping provides a much faster runtime and does not break down at critical frequencies. In this section, the key theoretical points will be discussed.

Conformal mapping is the mathematical transformation of one complex function to another while preserving all infinitesimal angles. In hydrodynamics, a conformal map can be used to map between a potential flow problem about a convenient geometry and one without, while preserving Laplace's equation and boundary conditions. For instance, if one can find a the proper conformal mapping function $f : \phi_{cyl} \rightarrow \phi_X$, it can be used to attain a valid potential field ϕ_X from the classic half-cylinder solution ϕ_{cyl}. ϕ_{cyl} is a potential that satisfies the linear boundary conditions for an oscillating half-cylinder and was originally presented in [34].

ϕ_{cyl} can be mapped to a Lewis form [7] with

$$\phi_{Lewis} = \phi_{cyl} + a_1 \phi_{cyl}^{-1} + a_3 \phi_{cyl}^{-3} \tag{2.33}$$

where

$$\begin{aligned} \lambda &= \frac{b}{2d} = \frac{1 + a_1 + a_3}{1 - a_1 + a_3} \\ s &= \frac{\pi}{4} \frac{1 - a_1^2 - 3a_3^2}{4(1 + a_3^2) - a_1^2} \end{aligned} \tag{2.34}$$

where b, d and s are the sectional beam, draft, and area coefficient, respectively.

ϕ_{cyl} can be mapped to a Bulb form with

$$\phi_{Bulb} = \phi_{cyl} + \frac{B \phi_{cyl}}{\phi_{cyl}^2 + A} \tag{2.35}$$

where

41

$$\lambda = \frac{1 - A^2 + AB + B}{1 - A^2 + AB - B} \qquad (2.36)$$

$$s = \frac{\pi}{4}\left(1 + A\frac{1 - \lambda^2}{2\lambda}\right)$$

The pressure per length can be found for each section by substituting the sectional potentials into the unsteady Bernoulli equation and linearizing about the mean hull position. Sectional coefficients and forces are attained by integrating the sectional pressures on the mean section boundary assuming that only small displacements of the boundary occur.

In Figures 2-12 and 2-13, MIT5D derived sectional added mass/damping in sway and heave are shown. These results are nearly identical to those presented in Vugts famous 1968 experiments [71].
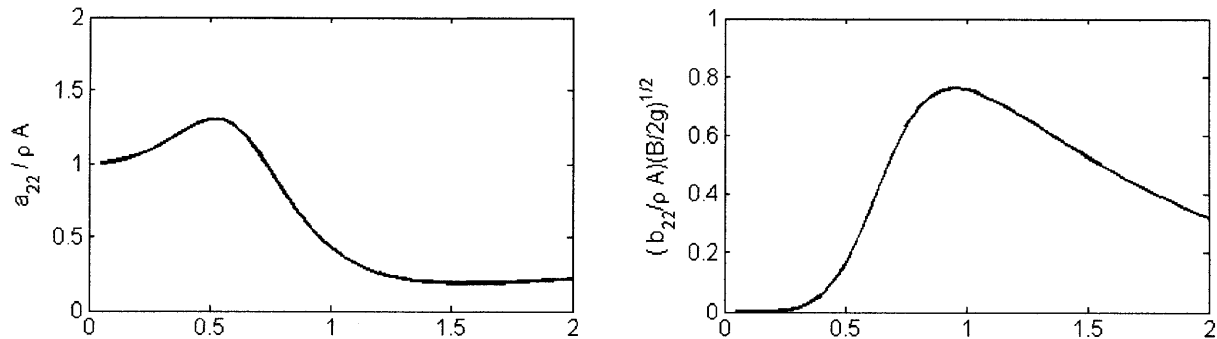
Figure 2-12: Non-dimensional sectional added mass and damping in sway direction for a half-cylinder.

2.5.2 Strip Theory

The strip theory equations used in the AES simulator are taken verbatim from the original strip theory paper by Salvesen, Tuck and Faltinsen. The same right-handed coordinate system is used, fixed such that the z-axis is vertically upward through the ship center of gravity and the x-axis runs the ships longitudinal axis, on the undisturbed free surface.

Begin with Eq. 2.31. If the ship has lateral symmetry, the equations of motion reduce to two coupled sets of ordinary differential equations. The heave-pitch set

42
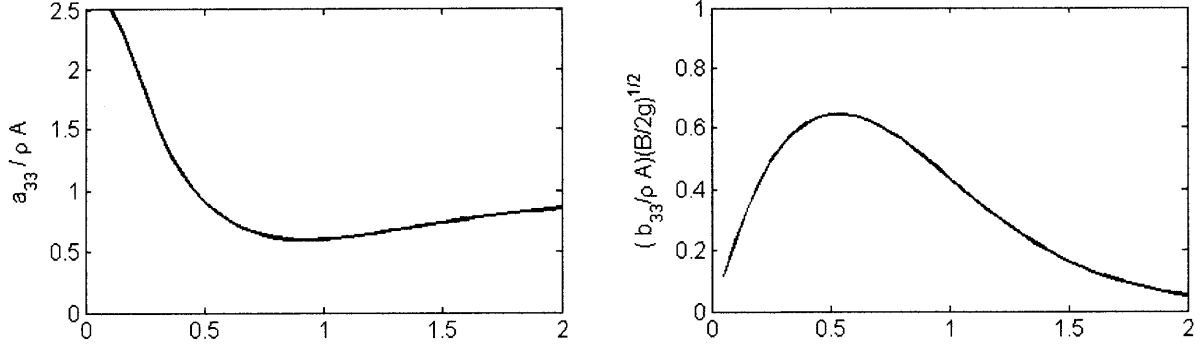
Figure 2-13: Non-dimensional sectional added mass and damping in heave direction for a half-cylinder.

$$(M + A_{33})\ddot{\eta}_3 + B_{33}\dot{\eta}_3 + C_{33}\eta_3 + A_{35}\ddot{\eta}_5 + B_{35}\dot{\eta}_5 + C_{35}\eta_5 = F_3 e^{i\omega t} \qquad (2.37)$$

$$A_{53}\ddot{\eta}_3 + B_{53}\dot{\eta}_3 + C_{53}\eta_3 + (I_5 + A_{55})\ddot{\eta}_5 + B_{55}\dot{\eta}_5 + C_{55}\eta_5 = F_5 e^{i\omega t} \qquad (2.38)$$

and the sway-roll-yaw set

$$(M + A_{22})\ddot{\eta}_2 + B_{22}\dot{\eta}_2 + (A_{24} - Mz_c)\ddot{\eta}_4 + B_{24}\dot{\eta}_4 + A_{26}\ddot{\eta}_6 + B_{26}\dot{\eta}_6 = F_2 e^{i\omega t} \qquad (2.39)$$

$$(A_{42} - Mz_c)\ddot{\eta}_2 + B_{42}\dot{\eta}_2 + (I_4 + A_{44})\ddot{\eta}_4 + B_{44}\dot{\eta}_4 \qquad (2.40)$$

$$+C_{44}\eta_4 + (A_{46} - I_{46})\ddot{\eta}_6 + B_{46}\dot{\eta}_6 = F_4 e^{i\omega t}$$

$$A_{62}\ddot{\eta}_2 + B_{62}\dot{\eta}_2 + (A_{64} - I_{46})\ddot{\eta}_4 + B_{64}\dot{\eta}_4 + (A_{66} + I_6)\ddot{\eta}_6 + B_{66}\dot{\eta}_6 = F_6 e^{i\omega t} \qquad (2.41)$$

where z_c is the distance from the waterline to the ship's cross-sectional center of gravity.

The basis of modern strip theory is as follows: by making the assumptions that 1) the beam of the ship varies smoothly and 2) the waves generated by the ship are short in comparison to its length, one can accurately reduce the three-dimensional problem to an integration of two dimensional problems, so long as the increment between two-dimensional sections is sufficiently small (usually accomplished with 20 ship sections). That is, all the aggregate ship coefficients

43

in the equations of motion above can be computed by integrating the sectional coefficients and adding speed effects to satisfy the boundary condition of the translating ship. All of the strip theory coefficient equations are given in Appendix A; for details of their derivation, see Appendix 1 of [62].

If one assumes that the responses are harmonic with frequency ω,

$$\eta_j = |\eta_j|\sin(\omega t + \angle\eta_j), \tag{2.42}$$

then substitutes, and cancels, the set of second order ODEs reduce to linear equations [69]. Complex response amplitude operators (RAOs) can be computed by solving the resulting sets of linear equations at any discrete set of ω, U and β:

$$\tilde{H}_j(\omega, U, \beta) = \frac{1}{\alpha}|\eta_j(\omega, U, \beta)|\angle\eta_j(\omega, U, \beta). \tag{2.43}$$

The remaining issue is the nonlinear roll damping introduced as B_{44}^* in Eq. 18 in Appendix A. The nonlinear damping coefficient contains components from a variety of different mechanisms including skin friction, eddy making dissipation, and bilge keel separation, [32]. In general, these added damping forces are quadratic in nature

$$F_{44}^* = \delta\dot{\eta}_4|\dot{\eta}_4| \tag{2.44}$$

where δ is a function of hull geometry and roughness solved for analytically or with look-up tables. To fit into the linear framework accurately, B_{44}^* is chosen such that the energy dissipation per cycle is the same as the quadratic case:

$$\int \delta\dot{\eta}_4{}^2|\dot{\eta}_4|dt = \int B_{44}^*\dot{\eta}_4{}^2 dt. \tag{2.45}$$

After assuming a harmonic roll motion, Eq. 2.45 can be satisfied by $B_{44}^* = \frac{8}{3\pi}\delta(\omega)|\eta_4|$. To solve for B_{44}^*, an iterative procedure is used. First, a guess is given for the roll amplitude, $|\eta_4^i|$. Then $B_{44}^{*,i}$ is computed, substituted into Eq. 18 in Appendix A, and a new roll amplitude $|\eta_4^{i+1}|$ is solved for with linear RAOs. $B_{44}^{*,i+1}$ is recomputed at the new roll amplitude. This is continued until convergence is achieved.

In Figures 2-14 and 2-15, normalized RAOs are shown for a half-cylinder, for each of the 5DOF; all RAOs are at a ship speed of 25 knots. These results match well with physical experiments and other numerical results. Electronic comparison has been conducted successfully against results attained from an independent program written by a fellow MIT graduate student [20].
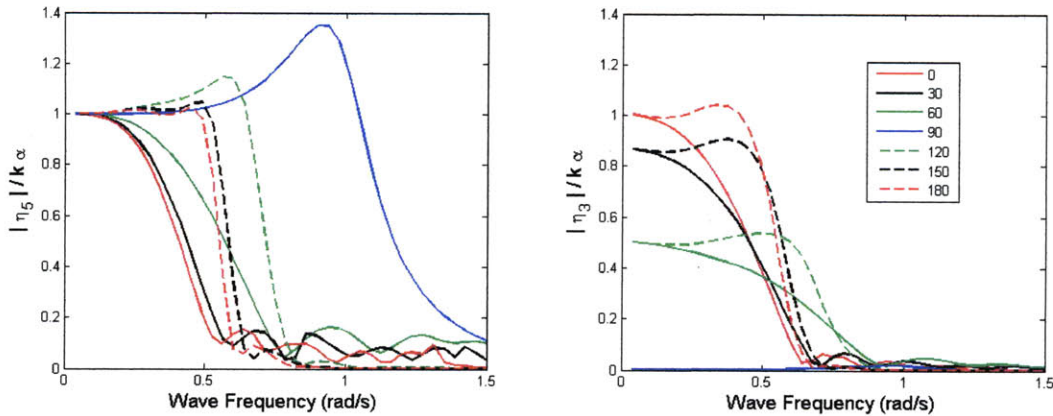
Figure 2-14: RAOs for half-cylinder in heave and pitch.

Sway, roll, and yaw results are not shown for seas less than 90 degrees because strip theory appears to break down as encounter frequencies approach zero. As $\omega_0 \rightarrow kU \cos \beta$, the predicted RAOs spike to, in some cases, greater than 10. This is of low concern to this AES research because it is only heave and pitch dynamics used to assess the propeller loading changes due to surface effects. In [30], a more accurate procedure for following seas simulation is given.

Experiments with the DDG51 hull give heave and pitch results that compare well with the seakeeping programs of others. However, as $\omega_0 \rightarrow 0$ the pitch RAO does not converge properly (at the same rate at the wave number). This will be acceptable for the time simulator since there are no wind waves and accordingly only a very small fraction of the wave components have energy at frequencies below 0.25 rad/s.

2.5.3 Second Order Forces

The seakeeping analysis presented above only accounts for first order wave forces. While second-order wave forces are in general much smaller in magnitude, they, unlike the first-order
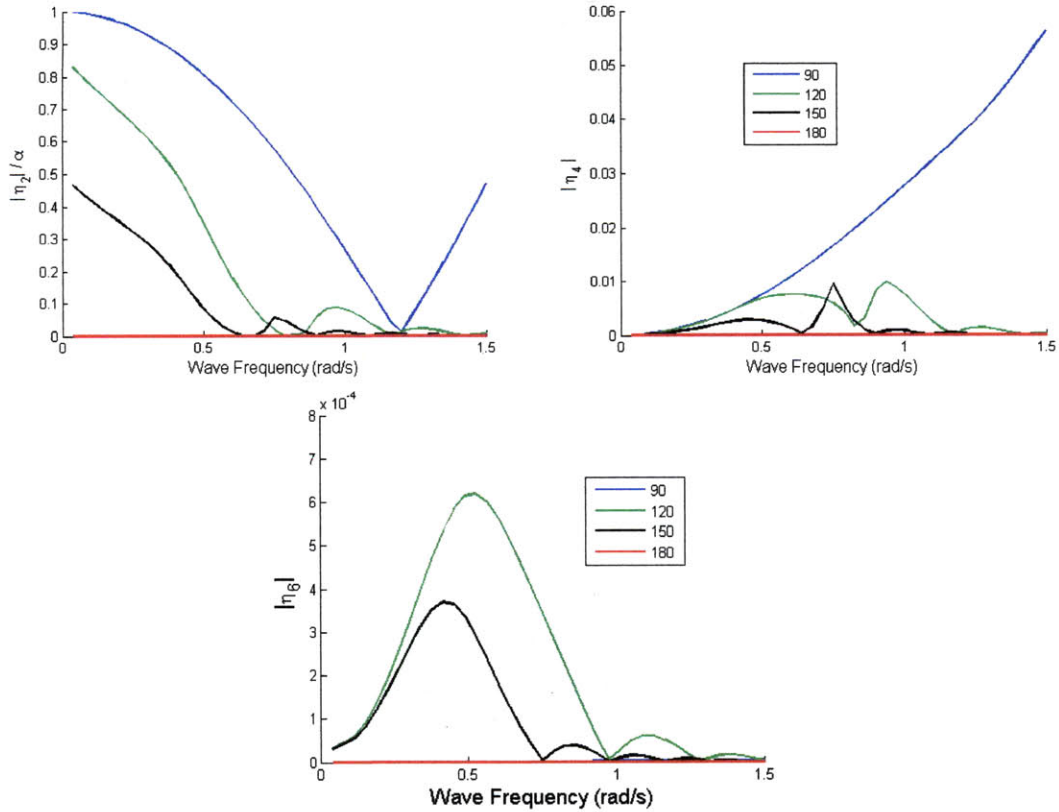
Figure 2-15: RAOs for half-cylinder in sway, roll, and yaw.

forces, have substantial low- and zero-frequency content. These slowly varying forces, called added resistance (surge), drift force (in sway), and drift moment (in yaw), contribute significantly to the position of a floating body over time. Since a key metric in AES development is fuel consumption, it is desirable to account for these second order forces which can add 20-30 % resistance.

Drawing off of work by Havelock, Gerritsma, and Maruo, [61] gives the most refined and robust method for the computation of second order forces using strip theory. The added resistance and drift force are derived

$$
\begin{aligned}
F_{x,add} &= (\cos \beta) F_{add} \\
F_{y,add} &= (\sin \beta) F_{add}
\end{aligned}
\tag{2.46}
$$

46

where

$$F_{add}(\omega, U, \beta) = \sum_{j=2}^{6} \left\{ \frac{i}{2} k \tilde{H}_j ((F_j^I)' + \hat{F}_j^D) \right\} + F_7. \qquad (2.47)$$

$(F_j^I)'$ is the complex conjugate of the Froude-Krylov wave force component. $\hat{F}_j^D$ is the same as the diffraction wave force component, but derived with the complex conjugate of the wave potential. Then, F_7 is

$$F_7 = \frac{1}{2} \alpha^2 k \frac{\omega_0^2}{\omega} \int e^{-2kds} (b_{33} \sin^2 b_{22}) d\xi. \qquad (2.48)$$

In Figure 2-16, added resistance and drift force results are compared with [61] to demonstrate proper implementation.
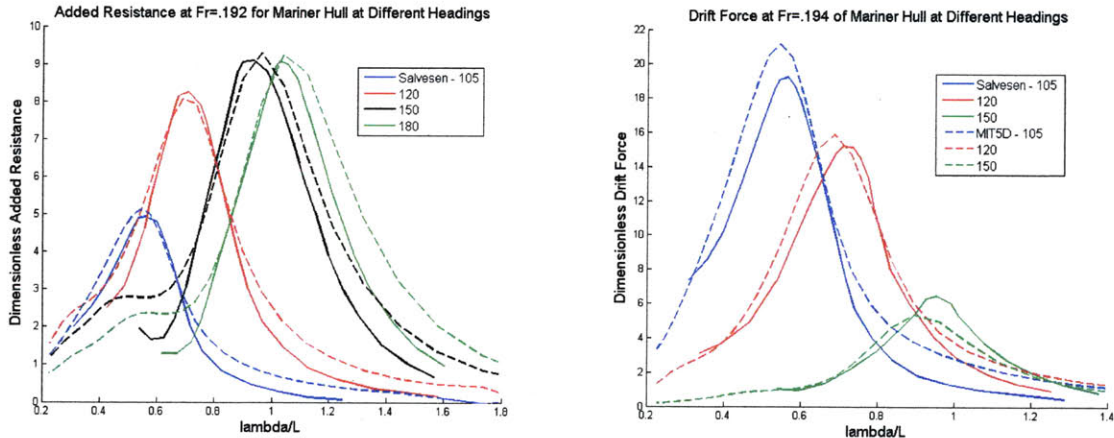
Figure 2-16: Second order force result comparison with [61].

2.5.4   Time Domain Generalization

In this section, the theoretical groundwork is laid for the generalization of frequency domain seakeeping equations to time domain equations. Then, the random sea model is described. Finally, practical simulation issues are addressed.

This simulator applies a quasi-steady approach for time domain simulation. True time domain solutions to seakeeping have been derived which satisfy boundary conditions for the instantaneous hull position, allowing for larger amplitude motion fidelity [5]. They are not

applied here due to their complexity and larger computational effort.

Begin with the second-order ODEs for heave-pitch in discrete seas with frequency ω_0, amplitude α, and phase γ, and direction μ. Assuming the ship is stationary and oriented in the direction of the global x-axis

$$(M + A_{33})\ddot{\eta_3} + B_{33}\dot{\eta_3} + C_{33}\eta_3 + A_{35}\ddot{\eta_5} + B_{35}\dot{\eta_5} + C_{35}\eta_5 = \alpha\hat{F}_3 e^{i\omega_0 t + \gamma} \tag{2.49}$$

$$A_{53}\ddot{\eta_3} + B_{53}\dot{\eta_3} + C_{53}\eta_3 + (I_5 + A_{55})\ddot{\eta_5} + B_{55}\dot{\eta_5} + C_{55}\eta_5 = \alpha\hat{F}_5 e^{i\omega_0 t + \gamma} \tag{2.50}$$

The added mass and damping are functions of the wave frequency, for instance $A_{33}(\omega_0)$. The unit wave excitements are functions of both wave frequency and wave direction, for instance $\hat{F}_3(\omega_0, \mu)$. For the remainder of this derivation, a matrix form will be used

$$[M_{35} + A_{35}]\frac{d^2}{dt^2}\vec{\eta_{35}} + B_{35}\frac{d}{dt}\vec{\eta_{35}} + C_{35}\vec{\eta_{35}} = \alpha\vec{\hat{F}}_{35} e^{i\omega_0 t + \gamma}. \tag{2.51}$$

If the ship is not stationary, for instance with speed U and heading Ψ, the equation becomes

$$[M_{35} + A_{35}]\frac{d^2}{dt^2}\vec{\eta_{35}} + B_{35}\frac{d}{dt}\vec{\eta_{35}} + C_{35}\vec{\eta_{35}} = \alpha\vec{\hat{F}}_{35} e^{i\omega t - k(x\cos\mu + y\sin\mu) + \gamma} \tag{2.52}$$

where the encounter frequency $\omega = |\omega_0 - kU\cos\beta|$ and $\beta = \Psi - \mu$. x and y are the global coordinates of the ship as determined by the maneuvering equations. Now the added mass and damping matrices are functions of encounter frequency and speed, for instance $A_{35}(\omega, U)$, and the unit wave excitement is a function of encounter frequency, speed, and heading, $\vec{\hat{F}}_{35}(\omega, U, \beta)$.

A solution for this equation, assuming a steady speed and heading, can be attained by assuming that the heave and pitch responses are harmonic with frequency ω:

$$\eta_3(t) = \alpha|\tilde{H}_3(\omega, U, \beta)|\cos(\omega t - k(x\cos\mu + y\sin\mu) + \gamma + \angle\tilde{H}_3(\omega, U, \beta)) \tag{2.53}$$

$$\eta_5(t) = \alpha|\tilde{H}_5(\omega, U, \beta)|\cos(\omega t - k(x\cos\mu + y\sin\mu) + \gamma + \angle\tilde{H}_5(\omega, U, \beta))$$

48

where $|\tilde{H}_j|$ is the unit response magnitude and $\angle\tilde{H}_j$ is the response phase delay for state j.

After substitution, rearrangement, and cancelling, an expression is attained for the complex response amplitude operator of both heave and pitch

$$\begin{bmatrix} \tilde{H}_3(\omega, U, \beta) \\ \tilde{H}_5(\omega, U, \beta) \end{bmatrix} = \frac{\vec{F}_{35}(\omega, U, \beta)}{-\omega^2[M_{35} + A_{35}(\omega, U)] + i\omega B_{35}(\omega, U) + C_{35}} \tag{2.54}$$

When coupled with the maneuvering model, the speed and heading of the ship become time variant. A quasi-steady approach for the seakeeping simulation in the time domain is used

$$\eta_3(t) = \alpha|\tilde{H}_3(\omega, U(t), \beta(t))|\cos(\omega t - k(x\cos\mu + y\sin\mu) + \gamma + \angle\tilde{H}_3(\omega, U(t), \beta(t)) \tag{2.55}$$

$$\eta_5(t) = \alpha|\tilde{H}_5(\omega, U(t), \beta(t))|\cos(\omega t - k(x\cos\mu + y\sin\mu) + \gamma + \angle\tilde{H}_5(\omega, U(t), \beta(t)).$$

The wave surface elevation at the stern, by the propeller, is

$$\eta_s(t) = \alpha(\omega t - k[(x - x_p\cos(\Psi))\cos\mu + (y - x_p\sin(\Psi))\sin\mu] + \gamma). \tag{2.56}$$

Finally, the distance from the propeller hub to the free surface is

$$\eta_{prop}(t) = h_0 + \eta_s(t) - \eta_3(t) + x_p\eta_5(t) \tag{2.57}$$

where h_0 is the calm water distance.

This quasi-steady approach is acceptable for large ships because of the vastly different time constants between the maneuvering and seakeeping states. The changes in speed and heading occur very slowly so the seakeeping dynamics due to these changes are negligible.

The Bretschneider spectrum is used for random wave generation

$$S(\omega_0) = \frac{5}{16}\frac{\omega_n^4}{\omega_0^5}H_{1/3}^2 e^{-5\omega_n^4/(4\omega_0^4)} \tag{2.58}$$

49

SeaState	ω_n (rad/s)	$H_{1/3}$ (ft)
2	0.997	0.984
3	0.838	2.952
4	0.714	6.232
5	0.648	10.824
6	0.507	16.400

Table 2.4: Bretschneider parameters for different sea states.

where ω_n is the peak frequency and $H_{1/3}$ is the significant wave height. Table 2.4 shows Bretscneider parameters for a variety of sea states [31]. Figure 2-17 shows the spectrums for different sea states.
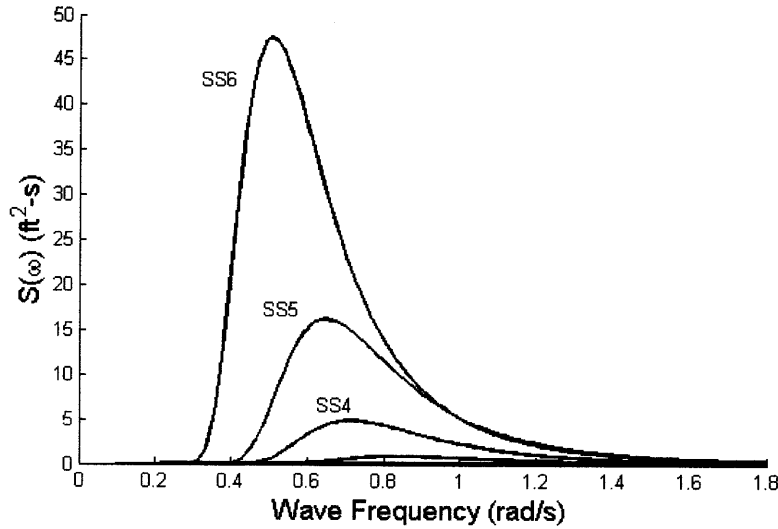
Figure 2-17: Bretschneider spectrums for different sea states.

Wave frequencies and amplitudes are conventionally sampled from a spectrum using the following procedure. First, the number of components N_s is selected; for seakeeping programs, $100 < N_s < 500$. Next, spectrum bounds are selected, ω_{min} and ω_{max}. The spectrum is than uniformly stratified with increment $\delta\omega = (\omega_{max} - \omega_{min})/N_s$. Each of the strata are sampled randomly to get the wave frequencies $\omega_0 = [\omega_{01}, \omega_{02}, ..., \omega_{0N_s}]$. The paired amplitudes are selected so that the sampled wave has the same energy content as the spectrum, $\alpha_i = \sqrt{2S(\omega_{0i})\delta\omega}$.

A $\cos^h(\Delta\mu)$ spreading function is added to the discrete user-inputted wave direction μ to add more fidelity to the random sea model. h is a parameter that defines the bandwidth of

the spreading function. Values of $\Delta\mu$ are sampled with a rejection sampling method. The set of N_s wave directions are computed $\mu_i = \mu + \Delta\mu_i$.

N_s wave phases are selected randomly from a uniform distribution.

For each wave component $z_i(x, y, t) = \alpha_i \cos(\omega_{0i}t - k(x\cos\mu_i + y\sin\mu_i) + \gamma_i)$, the seakeeping analysis is computed and the motions are superimposed.

$$\eta_j(t) = \sum_i^{N_s} \alpha_i |\tilde{H}_j| \cos\left(\omega_i t - k_i(x\cos\mu_i + y\sin\mu_i) + \angle\tilde{H}_j + \gamma_i\right) \tag{2.59}$$

where $\omega_i = \omega_{0i} - k_i U \cos\beta_i$ with $\beta_i = \Psi - \mu_i$ and $k_i = \omega_{0i}^2/g$.

The time domain second order forces are modeled using Newman's first approximation to slowly varying second order forces [54]:

$$F^2(t, \omega, U, \beta) = \sum_{i=1}^{N_s} \alpha_i^2 F_{add}(\omega_i, U, \beta) \tag{2.60}$$

$$+ \ 2\sum_{i=1}^{N_s} \sum_{j=1}^{M_s < N_s} \alpha_i \alpha_j F_{add}\left(\frac{\omega_i + \omega_j}{2}, U, \beta\right) \cos((\omega_i - \omega_j)t + \gamma_i + \gamma_j + \lambda_i - \lambda_j)$$

where λ_i represents the lag or lead of wave component i due to the ships global position, not shown for the sake of space.

The seakeeping analysis is not done serially with the time integration of the seakeeping-maneuvering model for practical reasons; this simulation framework would require hours, if not days, to carry out simulations over only a few wave periods. Instead, all seakeeping analysis is carried out pre-simulation. Added mass and damping coefficients are stored in 2-dimensional matrices indexed by encounter frequency and ship speed. First and second order wave forces and RAOs are stored in 3-dimensional matrices indexed by wave frequency, ship speed, and ship heading. For each time step, the RAO matrix is interpolated for each wave component, superimposing each motion component to attain instantaneous motions. For each time step, Newman's approximation is used to attain the instantaneous second-order forces.

Results are given in Chapter 5 for the results of the seakeeping-maneuvering model coupled with the IPS.

Chapter 3

High Fidelity Component Model Alternatives

In Chapter 2, descriptions were given for submodels of the default end-to-end AES simulator. While the AES simulator boasts high order maneuvering and seakeeping submodels, the prime mover, IPS, and propeller submodels are relatively low order.

The choice of low order modeling leads to extremely fast runtimes allowing for iterative simulation analysis like optimization or statistical analysis by way of Monte Carlo simulation. Of course, there is no free lunch. Lower order models try to capture the fundamental input-output dynamics of a model by reducing, combining, and averaging the internal states, but often, on top of losing explicit internal state information, model fidelity is compromised. For the sake of completeness, the next subsections will present higher order models for the prime mover and the propeller. Higher order models for IPS componentry are discussed in Chapter 4.

- The low order gas turbine model employed by the AES simulator uses the quasi-steady application of a speed-torque-throttle curve, a dynamic turbine shaft, and PI speed control. This model provides a good fidelity representation of the key prime mover dynamics and a working feedback control system. However, the higher order model presented here 1) functions with optimal control and 2) includes thermodynamic and hydraulic states allowing for the prediction of machine limitations, engine surge, and failures.

52

- The low order IPS submodel employed by the AES simulator is a time-averaged, combined phase representation of the true IPS. It is accurate to second-order effects across the IPS, like the conservation of power, but its internal states are not explicitly representative of physical states. The higher order model presented in Chapter 4 includes the true AC dynamics, three-phase electric machinery, true inverter switching dynamics, and current hysteresis control of the induction motor. This model predicts 1) physically representative internal state information and 2) higher order harmonic effects, both at the expense of runtime.

- The low order propeller submodel employed by the AES simulator uses the quasi-steady application of kq-kt curves for a generic Waginingen B-class propeller in open sea. Cavitation effects are estimated with a first-order approximation. Traverse flow effects are not captured. The higher order modeling techniques discussed here provide 1) more degrees of freedom for the propeller model and 2) propeller flow dynamics.

3.1   A LQG-LTR Controlled Jet Turbine Model

In Kappos 1983 thesis [36], a linearized 23 state, 4 input, 4 output, F-100 jet turbine model is presented. The paper goes on to do modal decomposition on the full order model, eliminating the modes with low magnitude and the modes significantly faster than the target control bandwidth. This process as a whole is called model reduction. The result is a 17 state system to be used for controller design. The control is a multi-input multi-output (MIMO) linear-quadratic Gaussian - loop transfer recovery (LQG-LTR) controller. Loop shaping of the singular value curves is used to deduce the Kalman filter gain matrix and loop transfer recovery is used to recover the open loop Kalman filter model singular value curves when linear quadratic regression (LQR) feedback control is added.

In its Appendix, Kappos gives the closed loop state space matrices. When implemented, these matrices do not elicit the results given in the body of the paper; in fact, the result turns out to be instable. Efforts were made in this Master's thesis to repeat the mathematical procedures for LQG derivation, detailed in [36], in order to attain a working closed loop system.

53

3.1.1 Development of LQG-LTR Controller

Figure 3-1 shows the closed loop framework for the control of the jet turbine as designed by Kappos.
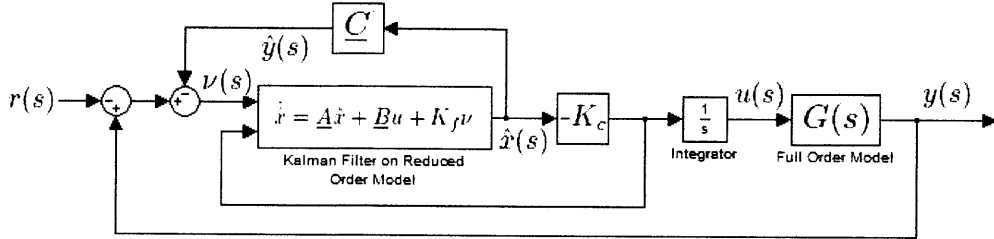
Figure 3-1: Closed loop schematic for LQG-LTR controlled F-100.

The plant model $G(s) = C_g(sI - A_g)^{-1}B_g$ is a linearized 23 state model of the jet turbine about an operating point (0.92 throttle). $G(s)$ has four inputs (throttle, stator vane angle, fan vane angle and nozzle exit radius) and four measureable outputs (compressor speed, fan speed, compressor discharge pressure, and fan inlet pressure). The measureable outputs are controlled by a LQG-LTR controller which uses a reduced order model of the jet turbine for the Kalman filter design; the reduced order model is achieved with model reduction of the full order system. For notation's sake, the state space representation for the reduced order model is given:

$$\dot{z}(t) = F_g z(t) + G_g u(t) \tag{3.1}$$
$$y(t) = H_g z(t) + D_g u(t).$$

Traditionally, for LQG controlled systems, the reduced model is integrator augmented. The controlled state space becomes

$$\underline{A} = \begin{bmatrix} 0 & 0 \\ G_g & F_g \end{bmatrix} \ , \ \underline{B} = \begin{bmatrix} I \\ 0 \end{bmatrix} \ , \ \underline{C} = \begin{bmatrix} D_g & H_g \end{bmatrix} \tag{3.2}$$

Kappos gives the open loop full order and reduced order state space matrices A_g, B_g, C_g,

D_g, F_g, G_g and H_g in the Appendix of his paper. These are used for the controller design.

The traditional LQG controller is composed of a linear quadratic regulator for optimal control and a Kalman filter for noise reduction [2]. The state space equations for the model are

$$
\begin{aligned}
\dot{x}(s) &= A_g x(s) + B_g u(s) & (3.3) \\
y(s) &= C_g x(s) \\
\dot{\hat{x}}(s) &= \underline{A}\hat{x}(s) + \underline{B}u(s) + K_f(y(s) - \hat{y}(s)) + K_f r(s) \\
\hat{y} &= \underline{C}\hat{x}(s) \\
u(s) &= -K_c \hat{x}(s).
\end{aligned}
$$

where $x(s)$ and $y(s)$ are the physical states and ouptuts and $\hat{x}(s)$ and $\hat{y}(s)$ are the estimated states and outputs, for an input $u(s)$. $r(s)$ is the reference input.

The objective of loop shaping, as specified in [36], is to select K_f such that the singular values of $G_f(s) = \underline{C}(sI - \underline{A})^{-1}K_f$ have bandwidths between 2 rad/s and 12 rad/s, meeting the demands of a fast controller while filtering the estimated noise.

The Kalman filter gain matrix is computed $K_f = \Sigma \underline{C}^T N^{-1}$ where N is a tuning parameter and Σ is the solution to the algebraic matrix Ricatti equation

$$
\underline{A}\Sigma + \Sigma \underline{A}^T + \Gamma \Gamma^T - \Sigma \underline{C}^T N^{-1} \underline{C} \Sigma^T = 0 \tag{3.4}
$$

where Γ is a second tuning parameter. In the absence of noise data, N and Γ are free to vary as tuning parameters. Let $N = \mu I$. This way, different values of μ shift the singular values of $G_f(s)$ to different band widths. Furthermore, let $\Gamma = \begin{bmatrix} G(\omega_p)^{-1} \\ 0 \end{bmatrix}$. This will pinch the singular values of $G_f(s)$ around ω_p. Trial and error led to $\mu = 5e - 3$ and $\omega_p = 3$ rad/s. Figure 3-2 shows the resulting singular value plot of $G_f(s)$. The bandwidth of the singular values are between 3.5 and 8.4 rad/s.
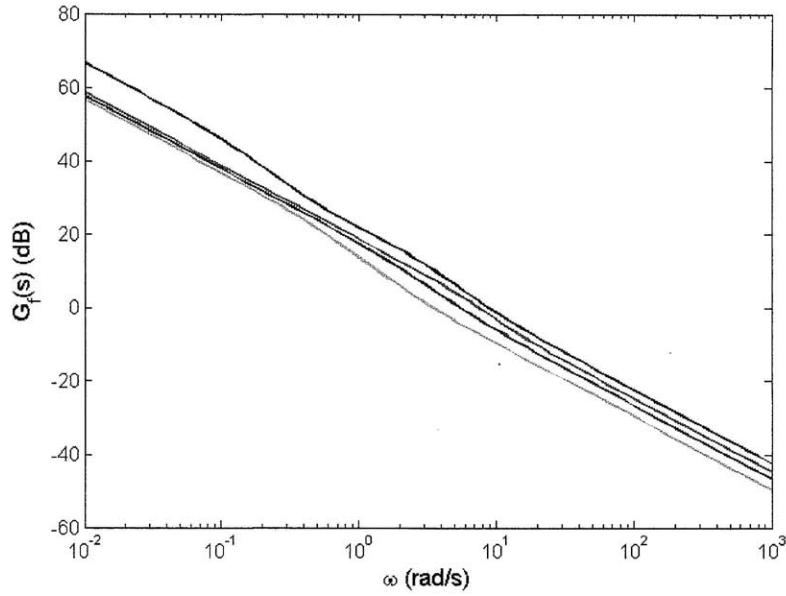
Figure 3-2: Singular value plot for Kalman loop transfer function after loopshaping.

The goal of loop transfer recovery is to select the LQR gain matrix K_c such that Kalman loop transfer function is recovered for the aggregate compensator transfer function $K(s)$.

$$K(s) = -K_c(sI - \underline{A} + \underline{B}K_c + K_f\underline{C})^{-1}K_f\underline{C}(sI - \underline{A})^{-1}\underline{B}. \tag{3.5}$$

The LQR gain is computed $K_c = R^{-1}\underline{B}^T P$ where R is a tuning parameter and P is the solution to algebraic matrix Ricatti equation

$$\underline{A}^T P + P\underline{A} + Q - P\underline{B}R^{-1}\underline{B}^T P = 0 \tag{3.6}$$

where Q is a second tuning parameter.

LTR methodology prescribes that $R = I$ and $Q = H^T H$ where $H = q\underline{C}$. In this framework, as q is increased, $K(s)$ will converge to $G_f(s)$.

Finally, it can be shown from Eq. 3.3 that the compensator matrices become

$$
\begin{aligned}
A_k &= \underline{A} - \underline{B}K_c - K_f\underline{C} \\
B_k &= K_f \\
C_k &= K_c
\end{aligned}
\tag{3.7}
$$

3.1.2 Numerical Results Comparison

With the controller designed, one can look at the open loop singular value plot $\frac{Y(s)}{E(s)} = G(s)\frac{I}{s}K(s)$ and the closed loop command-following singular value plot $\frac{Y(s)}{R(s)} = [I + G(s)\frac{I}{s}K(s)]^{-1}G(s)\frac{I}{s}K(s)$. Figure 3-3 shows the results presented in the Kappos thesis. Figure 3-4 shows the results of this thesis.
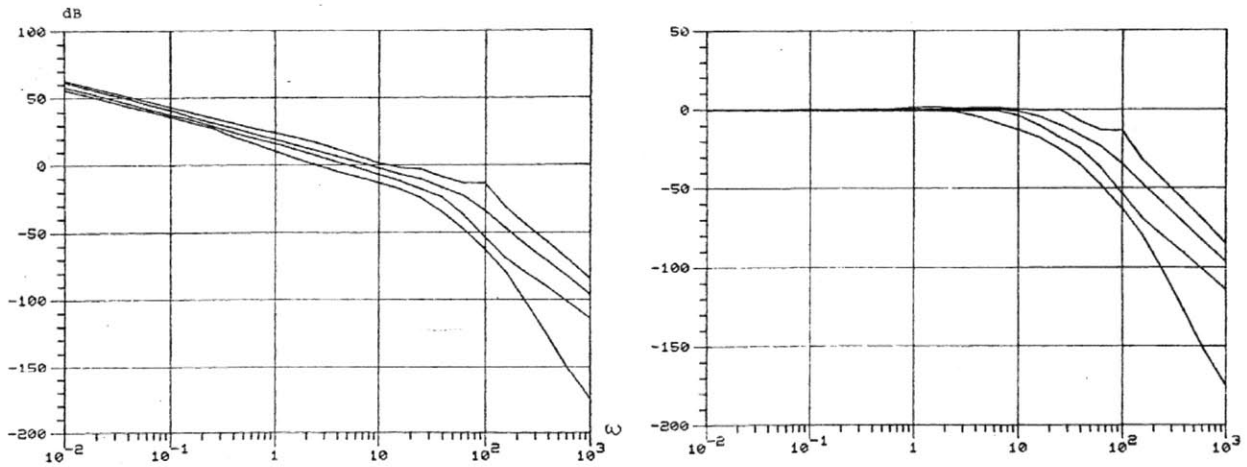
Figure 3-3: Singular values for Kappos' open and closed loop transfer functions.

To derive the closed loop state space model, start by defining the state vector $X = [X_{plant} \ X_{com} \ X_{int}]'$, where X_{plant} is a vector of the 23 engine model states, X_{com} is a vector of the 17 compensator states, and X_{int} is a vector of the integrals of the four compensator outputs. By this convention the linear equations are written
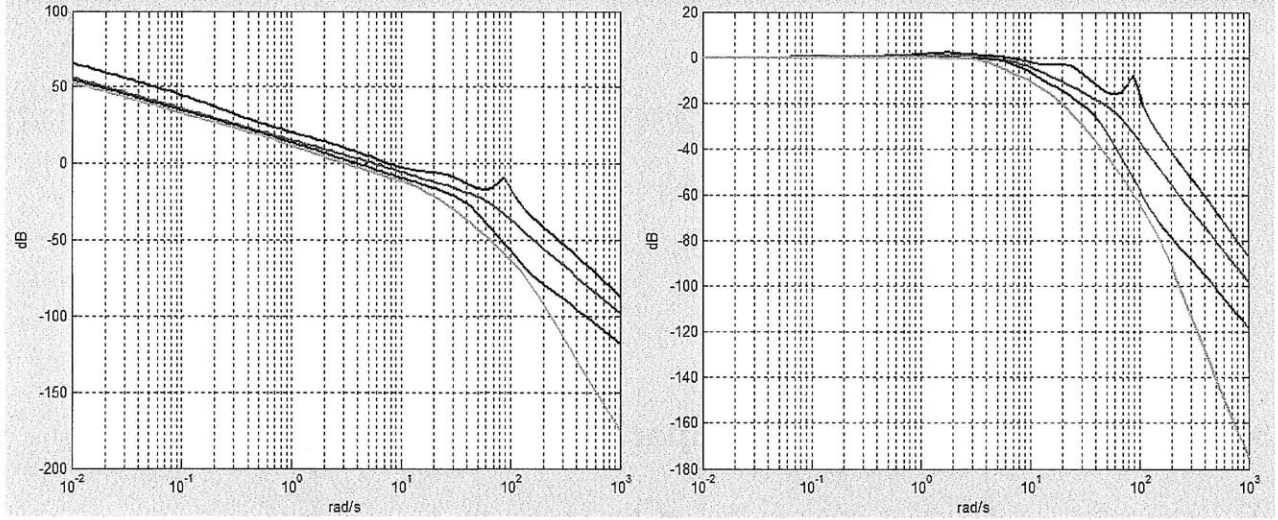
Figure 3-4: Singular values for this thesis's open and closed loop transfer functions.

$$
\begin{aligned}
\dot{X}_{plant} &= A_g X_{plant} + B_g U \\
\dot{X}_{com} &= A_k X_{com} + B_k E \\
\dot{X}_{int} &= dU
\end{aligned}
\tag{3.8}
$$

where E is the error vector, U is the plant input, and dU is the time derivative of the plant input. After the substitution for E, dU and U, the discretized equations are

$$
\begin{aligned}
\dot{X}_{plant} &= A_g X_{plant,n} + B_g X_{int,n+1} \\
\dot{X}_{com} &= A_k X_{com,n} + B_k (R - C_g X_{plant,n}) \\
\dot{X}_{int} &= C_k X_{com,n+1}
\end{aligned}
\tag{3.9}
$$

Kappos Appendix	Kappos Body	Schmitt
-0.473	$-0.475 \pm j1.83E - 3$	$-0.474 \pm j2.5E - 3$
-0.548	$-0.649 \pm j6E - 4$	$-0.649 \pm j6E - 4$
-0.649	$-1.482 \pm j1.40$	$-1.755 \pm j1.62$
-0.926	-2.122	-2.122
-2.128	-2.127	-2.127
$-2.25 \pm j1.03$	$-4.37 \pm j4.08$	$-3.56 \pm j2.98$
$-2.38 \pm j15.90$	$-5.34 \pm j87.60$	$-5.14 \pm j5.80$
$-4.01 \pm j12.27$	$-5.72 \pm j7.71$	$-6.29 \pm j87.96$
4.605	$-8.31 \pm j25.85$	$-7.35 \pm j4.41$
$-5.19 \pm j3.83$	$-8.58 \pm j7.09$	$-9.43 \pm j23.67$
$-5.50 \pm j87.37$	$-11.77 \pm j1.94$	$-11.78 \pm j1.20$
$-11.59 \pm j22.67$	-13.57	-12.71
$-11.82 \pm j3.93$	-16.44	-17.02
-13.73	$-17.92 \pm j4.82$	$-17.83 \pm j4.79$
-16.41	$-18.08 \pm j6.28$	$-18.73 \pm j6.42$
$-16.82 \pm j3.13$	-19.85	-19.82
$-19.74 \pm j0.86$	$-21.38 \pm j0.842$	$-21.36 \pm j0.757$
-20.42	$-21.95 \pm j0.560$	$-22.17 \pm j0.208$
-20.87	$-24.56 \pm j35.05$	$-22.85 \pm j34.34$
-21.34	-41.62	-41.41
$-21.60 \pm j38.03$	-50.00	-49.98
$-29.26 \pm j5.52$	$-50.21 \pm j28.25$	$-50.02 \pm j27.30$
-42.44	-93.83	-85.35
-50.00	-177.24	-177.73
$-50.44 \pm j29.30$	-577.02	-577.02
-94.33	-764.24	-763.28
-177.22	-777.35	-7774.9
-577.02	-7710.2	-77104
-764.26	-25075	-250750
-7773.7		
-77101		
-2.507e5		

Table 3.1: Closed loop eigenvalue comparison for F100 state space models.

Using a first order finite difference approximation for the $n + 1$ terms, with step size h, the matrix form is attained

$$\begin{bmatrix} I & 0 & -hB_g \\ 0 & I & 0 \\ 0 & -hC_k & I \end{bmatrix} \frac{d}{dt} \begin{bmatrix} X_{plant} \\ X_{com} \\ X_{int} \end{bmatrix} = \begin{bmatrix} A_g & 0 & B_g \\ -B_k C_g & A_k & 0 \\ 0 & C_k & 0 \end{bmatrix} \begin{bmatrix} X_{plant} \\ X_{com} \\ X_{int} \end{bmatrix} + \begin{bmatrix} 0 \\ B_k \\ 0 \end{bmatrix} R \quad (3.10)$$

$$\text{with } Y = \begin{bmatrix} 0 & C_g & 0 \end{bmatrix} \begin{bmatrix} X_{plant} \\ X_{com} \\ X_{int} \end{bmatrix}.$$

By setting h to zero one attains the closed loop continuous state space model. In Table 3.1, ordered eigenvalues are given for three closed loop A matrices: 1) the A matrix formed from the plant and compensator matrices given in Kappos's Appendix, 2) eigenvalue results presented by Kappos in the body of the paper, and 3) results from this thesis's re-derivation. Notice that the matrices given in Kappos's Appendix lead to a slightly different eigen-footprint that includes an instable pole (4.605).

The new closed loop state space matrices for the LQG-LTR compensator are given in Appendix B. The B matrix is structured to input the four input commands and the C matrix to return the four outputs.

3.1.3 From Jet Turbine Model to Electrical Generation Model

It would be a shame to let the F100 data go to waste. Here the use of an altered F100 model for a gas turbine model to be used with the AES simulator is speculated.

First is a comparison of the power output of the F100 model and the LM2500. The dry thrust of the a F100 engine is 79.1 kN with an exit diameter of approximately 1 m^2 [58]. If it is assumed that the gas turbine captures most of the jet turbine exhaust, one gets a rough number for the power of the hypothetical converted F100 gas turbine of 18.6 MW. This is comparable to the LM2500.

Physically speaking, the significant difference between a jet turbine and a gas turbine is the addition of a third stage of compensators that are designed to turn the thrust energy of the exhaust into rotational energy. In fact, many jet turbines are modified this way after their lifetime on a plane expires. The actuated inputs and measured outputs used by the F100 model are realistic for a gas turbine, however turbine shaft speed would invariably be included in the feedback control [37].

The method suggested in this thesis is to augment the full plant model with a state for

the turbine shaft speed

$$I_t \dot{\omega}_t = Q_t - Q_g \qquad (3.11)$$

where Q_t is an algebraic function of the jet turbine states cleverly chosen to be physically realistic. For instance, if one could gather data for the compressor turbine and nozzle geometry on the F100, one could approximate the exhaust velocity algebraically from the compressor speed using classical turbine mechanics [37]. Then, assuming a gas turbine blade geometry, one could approximate the torque Q_t from the exhaust velocity. I_t could then be selected to meet an operating speed of 60 Hz. The dynamics that would be lost would be for fluid flow states likely to be much faster than the dominant mechanical states. Then, instead of using compressor speed feedback, one would could turbine speed feedback.

With this new augmented model, all the steps of Kappos's thesis would need to be repeated including model reduction, Kalman filter loopshaping, and LTR.

3.2 Advanced Propeller Modeling Techniques

Candidly, the propeller model is the weak point of the model discussed in Chapter 2. Its generality and lack of dynamics compromise the usefulness of the program. An obvious next step in the development of the AES simulator is augmentation of the propeller model. For completeness, here is a discussion of some key additions that could be made.

3.2.1 Vortex Lattice Line Method

OpenPropV2.3 is the latest version of a state of the art propeller design and analysis tool developed at MIT [18]. The numerical model is based on the vortex lattice lifting line methods [38]. The design optimization method accepts a propeller geometry and inflow properties, partitions the propeller into blade elements, and solves for circulation and induced velocities of each element such that the torque is minimized for a specific thrust. Details are outside of the scope of this thesis but can be garnered in the references above.

The impressive potential of the program is its large design space including propeller geometry and inflow parameters. Figure 3-5 shows the user interface for the single propeller design

feature of the program.

6	Number of Blades	
200	Propeller Speed (RPM)	
2	Propeller Diameter (m)	

Hub Image Flag (Check for YES) ☑
Ducted propeller (Check for YES) ☐

1	Thrust Ratio
1	Duct Diameter/Prop Diameter
0.008	Duct Section Drag Coefficient

40000	Required Thrust (N)
5	Ship Velocity (m/s)
0.4	Hub Diameter (m)
20	Number of Vortex Panels over the Radius
10	Max. Iterations in Wake Alignment
1	Hub Vortex Radius/Hub Radius
0	Hub Unloading Factor: 0=Optimum
0	Tip Unloading Factotr: 1=Reduced Loading
1	Swirl Cancellation Factor: 1=No Cancellation
1025	Water Density (kg/m^3)

Meanline Type: NACA a=0.8
Thickness Form: NACA 65A010

r/R	c/D	Cd	Va/Vs	Vt/Vs	f0/c	t0/c	Skew	Xs/D
0.2	0.16	0.008	1	0	0.0174	0.2056	0	0
0.3	0.1818	0.008	1	0	0.0195	0.1551	0	0
0.4	0.2024	0.008	1	0	0.0192	0.1181	0	0
0.5	0.2196	0.008	1	0	0.0175	0.0902	0	0
0.6	0.2305	0.008	1	0	0.0158	0.0694	0	0
0.7	0.2311	0.008	1	0	0.0143	0.0541	0	0
0.8	0.2173	0.008	1	0	0.0133	0.0419	0	0
0.9	0.1806	0.008	1	0	0.0125	0.0332	0	0
0.95	0.1387	0.008	1	0	0.0115	0.0324	0	0
1	0.001	0.008	1	0	0	0	0	0

3	Shaft Centerline Depth (m)
0.3	Inflow Variation (m/s)
1.54	Ideal Angle of Attack (degrees)
20	Number of Points over the Chord

Filename Prefix
OpenProp

Run OpenProp

Figure 3-5: Input screen for OpenProp2.2.

There are base level geometry parameters like diameter and blade number, but also specific considerations like the thickness, camber, and chord as a function of blade radius, for example. Furthermore, the program allows for the specification of axial and traverse flow into the propeller which as discussed previously can be responsible for performance losses.

OpenProp v2.3 does not have a feature to derive k_T and k_Q curves from geometry alone. As of the date of this thesis publication, that feature has been developed, and it is planned to be released in future versions of the code. As soon as this faculty is added, it is recommended that OpenProp is used as a subroutine of the AES simulator to allow from a rich propeller design space.

3.2.2 Modern Cavitation Methods

Another area where the propeller model could improve is cavitation prediction accuracy. Cavitation is a modeling nightmare due to its viscous two-phase nature, its unpredictable stability, and its multiple formation mechanisms and manifestations.

As discussed in Chapter 2, the AES simulator uses first order approximation for cavitation losses. This three parameter model is demonstrated in [65] to be viable against physical results. The three key parameters are the h/R ratio where cavitation losses begin, the h/R

ratio where cavitation losses reach their maximum, and the maximum cavitation loss factor. Ideally, these three parameters could be estimated for any propeller shape and speed, though right now we settle for generic values.

An analytical approximation for cavitation prediction can be achieved after solving the vortex lattice lifting line equations. By comparing the minimum pressure coefficient on the propeller surface to the cavitation index, one can predict the onset of cavitation on propeller blades [38]. It should be noted that these predictions are far from perfect, but would allow less general parameter selection for the three parameter cavitation model discussed above.

Some attempts to numerically study cavitation ambitiously employ finite element methods including a propeller surface mesh, a fluid mesh, and a free surface mesh. Some studies with CFD program Fluent have shown correspondence for surface piercing propellers, but cavitation prediction for fully submerged propellers has proven unsuccessful so far [8].

Chapter 4

Stability Analysis of the MVDC Integrated Power System

This chapter presents a multi-purpose computational tool for performance and stability analysis of a MVDC IPS; in this study the MVDC IPS is modeled after the Purdue MVDC Testbed [4]. An austere approach to stability analysis is taken: nonlinear models are defined, steady state operating points are solved, and small displacement theory is used to linearize the system about the operating point and assess the performance and stability for open loop operation. Closed loop analysis is explored but not entirely resolved.
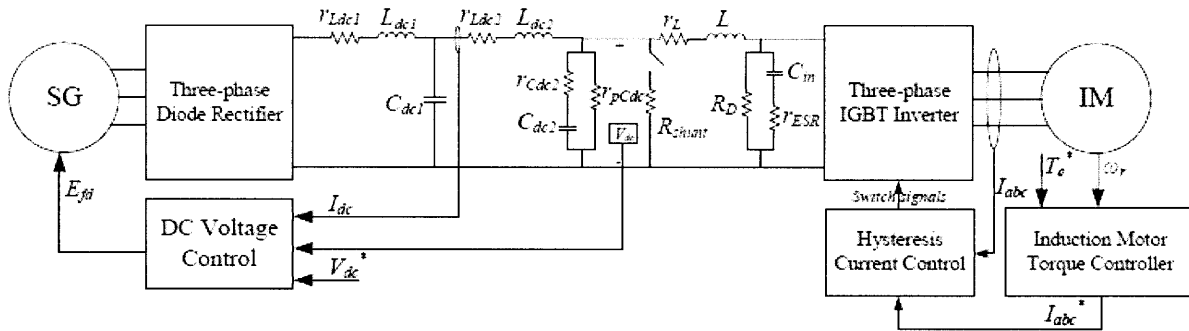
Figure 4-1: A schematic of the Purdue MVDC Testbed [49].

Let's briefly review the Purude MVDC Testbed (featured in Figure 4-1). In this study, the generator has been augmented with a linear gas turbine model and the motor with a quadratic propeller model, both presented in Chapter 2. Accordingly, the inputs of system

are target turbine speed, target DC bus voltage, and target torque. The measured states used in feedback control are DC voltage, DC current, motor torque, and motor current magnitude. The actuatable states are the synchronous generator field voltage and the inverter switching pattern. This analysis is made more tractable by splitting the generator side from the induction motor side, eliminating the coupling between the sides at the inverter. Accordingly, the study poses the question: "if the generator is running at operation conditions, what is the stability and performance of the motor side, and visa versa?" For generator side analysis, the motor side is modeled as a current sink with magnitude I. For the motor side analysis, the generator side is modeled as a voltage source v_{dc}. A method for combining the generator and motor sides is given in [64].

The capabilities of this tool include but are not limited to time-averaged models for generator and motor sides (Section 4.1), steady-state solvers for system equilibrium points and linearization about these points with small displacement theory (Section 4.2), stability/performance analysis for the open loop systems (Section 4.3), and in some capacity, the closed loop systems (Section 4.4). A high fidelity, unaveraged, Purdue MVDC Testbed model, is incorporated to check results throughout [49].

4.1   Description of IPS Models

"The Purdue [MV]DC Testbed is a voltage and power scaled DC power system with strong architectural similarities to power systems being investigated for future Navy ships" [4]. It includes a 59kW wound rotor synchronous machine and a 4-pole, 460 V, 50 Hp, 60Hz induction motor interfaced through a 3 phase, passive diode rectifier and IGBT inverter. The generator side is managed by PI droop control of the DC voltage and the motor current supply is controlled by current hysteresis control.

In this section, descriptions are given for the system components and time-averaged nonlinear equations are presented for the use in stability analysis.

4.1.1 Generator Side Models

A process flow diagram for the generator side is shown in Figure 4.1.1. The main components are a PI controlled gas turbine, a three phase SM, a passive rectifier, a passive filter, and DC voltage droop control.

Figure 4-2: Turbine-Generator side process flow diagram.

As will be detailed below, the resulting open loop model involves an eight state set of differential algebraic equations with five SM current states ($i_{g,qs}$ $i_{g,ds}$ $i_{g,qr}$ $i_{g,dr}$ i_{fd}), electrical rotor speed ω, and distribution voltage and current (v_{dc} i_{dc}). The nonlinear constraints are a product of the time averaged rectifer model, as will be shown. The inputs are the SM field voltage v_{fd} and the turbine speed command ω_t^* (note, the closed loop turbine control is included in the open loop model). A third input is the current sink magnitude I reflective of the operating condition for the induction motor; however, in this analysis, it will be assumed that I cannot be actuated. I can be approximated to meet some operating condition for the motor side by applying the power conservation equation across the inverter: $v_dcI = \omega_{rm}Q_m$.

For the closed loop system, a feedback state is introduced, the time derivative of the droop control feedback. The input becomes the command DC voltage v_{dc}^*.

Generator Equations

The SM mathematical equations in the rotor DQ reference frame [40] are

$$p\lambda_{g,qs} = v_{g,qs} + r_{g,s}i_{g,qs} - \omega\lambda_{g,ds} \qquad (4.1)$$

$$p\lambda_{g,ds} = v_{g,ds} + r_{g,s}i_{g,ds} + \omega\lambda_{g,qs}$$

$$p\lambda_{g,qr} = v_{g,qr} - r_{g,qr}i_{g,qr}$$

$$p\lambda_{g,dr} = v_{g,dr} - r_{g,dr}i_{g,dr}$$

$$p\lambda_{fd} = v_{fd} - r_{fd}i_{fd}$$

$$\lambda_{g,qs} = -L_{ls}i_{g,qs} + L_{mq}(-i_{g,qs} + i_{g,qr}) \qquad (4.2)$$

$$\lambda_{g,ds} = -L_{ls}i_{g,ds} + L_{md}(-i_{g,ds} + i_{fd} + i_{g,dr})$$

$$\lambda_{g,qr} = L_{g,qr}i_{g,qr} + L_{mq}(-i_{g,qs} + i_{g,qr})$$

$$\lambda_{fd} = L_{fd}i_{fd} + L_{md}(-i_{g,ds} + i_{fd} + i_{g,dr})$$

$$\lambda_{g,dr} = L_{g,dr}i_{g,dr} + L_{md}(-i_{g,ds} + i_{fd} + i_{g,dr})$$

where λ are magnetic fluxes, v are voltages, and i are currents. r and L are resistances and inductances, respectively. The subscript denotes the d or q reference frame and the stator (s), rotor (r), mutual (m), or field (fd).

After manipulation, these can be stated as a system of ordinary differential equations with current states ($i_{g,qs}$ $i_{g,ds}$ $i_{g,qr}$ $i_{g,dr}$ i_{fd}) (these are nonlinear equations due to the freedom of ω, the electrical rotor speed, to vary).

$$\frac{d}{dt}\begin{bmatrix} i_{g,qs} \\ i_{g,ds} \\ i_{g,qr} \\ i_{g,dr} \\ i_{fd} \end{bmatrix} = M_g^{-1}A_g \begin{bmatrix} i_{g,qs} \\ i_{g,ds} \\ i_{g,qr} \\ i_{g,dr} \\ i_{fd} \end{bmatrix} + M_g^{-1}\begin{bmatrix} 1 & 0 & 0 \\ 0 & 1 & 0 \\ 0 & 0 & 0 \\ 0 & 0 & 0 \\ 0 & 0 & 1 \end{bmatrix}\begin{bmatrix} v_{g,qs} \\ v_{g,ds} \\ v_{fd} \end{bmatrix} \qquad (4.3)$$

where

$$
M_g = \begin{bmatrix}
-(L_{ls} + L_{mq}) & 0 & L_{mq} & 0 & 0 \\
0 & -(L_{ls} + L_{mq}) & 0 & L_{md} & L_{md} \\
-L_{mq} & 0 & L_{g,qr} + L_{mq} & 0 & 0 \\
0 & -L_{md} & 0 & L_{md} & L_{g,dr} + L_{md} \\
0 & -L_{md} & 0 & L_{fd} + L_{md} & L_{md}
\end{bmatrix}
\tag{4.4}
$$

and

$$
\Lambda_g = \begin{bmatrix}
r_s & \omega(L_{ls} + L_{md}) & 0 & -\omega L_{md} & -\omega L_{md} \\
-\omega(L_{ls} + L_{mq}) & r_s & \omega L_{mq} & 0 & 0 \\
0 & 0 & -r_{g,qr} & 0 & 0 \\
0 & 0 & 0 & -r_{g,dr} & 0 \\
0 & 0 & 0 & 0 & -r_{fd}
\end{bmatrix} .
\tag{4.5}
$$

Turbine Equations

The equation for the mechanical speed of the rotor shaft stated generally is

$$
I_t \frac{d}{dt} \omega_t = Q_t - Q_g
\tag{4.6}
$$

where the rotor electrical speed is related to the mechanical speed through a pole multiple $\omega = \frac{P_g}{2} \omega_t$.

Some control is requred to maintain the shaft speed about an operating point; as in Chapter 2, PI feedback control will be used. Here, torque is actuated instead of throttle but this is analogous to actuating the throttle in the linear operating region. After substitution of the PI control and the SM electromagnetic torque equation [40] into 4.6, the equation becomes

$$I_t \frac{d}{dt}\omega_t = K_{p,t}(\omega_t^* - \omega_t) + K_{i,t} \int (\omega_t^* - \omega_t)dt \tag{4.7}$$

$$+ \frac{3P_g}{4}\left[(L_{mq} - L_{md})i_{g,qs}i_{g,ds} + L_{md}i_{g,qs}i_{g,dr} + L_{md}i_{g,qs}i_{fd} - L_{mq}i_{g,ds}i_{g,qr}\right].$$

Rectifier Equations

The time-averaged equations for the 6-phase rectifier are adapted from [57]. The first equation quantifies the average output of a 6-phase converter

$$\tilde{v_{dc}} = \frac{3\sqrt{3}}{\pi}\sqrt{v_{g,qs}^2 + v_{g,ds}^2}\cos\alpha - \frac{3}{\pi}X_{co}i_{dc}. \tag{4.8}$$

where X_{co} represents the commutating reactance of the left side of the rectifier and α is the firing angle which will be approximated as 0. The value of the parameter X_{co} is not known apriori and will be estimated from results with the unaveraged rectifier model; this procedure is discussed in the next section.

Two other equations impose the conservation of real and reactive power.

$$v_{g,qs}i_{g,qs} + v_{g,ds}i_{g,ds} = \frac{2}{3}\tilde{v_{dc}}i_{dc}\cos\phi \tag{4.9}$$

$$v_{g,qs}i_{g,ds} - v_{g,ds}i_{g,qs} = \frac{2}{3}\tilde{v_{dc}}i_{dc}\sin\phi \tag{4.10}$$

where $\phi = \cos^{-1}\frac{\pi}{3\sqrt{3}}\frac{\tilde{v_{dc}}}{\sqrt{v_{g,qs}^2 + v_{g,ds}^2}}$ is the power factor of the rectifier.

Filter Equations

The filter model used here is fourth order in voltage and captures the essential frequency behavior of the actual sixth order filter used in the Purdue MVDC Testbed. R_3 is an auxiliary load drawing off the bus for experiments with subsystem loads. The equations for the filter, derived with Kirchoff's laws, are:

$$K_{vv}^{(4)} \frac{d^4}{dt^4} v_{dc} + K_{vv}^{(3)} \frac{d^3}{dt^3} v_{dc} + K_{vv}^{(2)} \frac{d^2}{dt^2} v_{dc} + K_{vv}^{(1)} \frac{d}{dt} v_{dc} + K_{vv}^{(0)} v_{dc} = \tilde{v_{dc}} - (R_1 + R_2) \quad (4.11)$$

$$K_{ii}^{(1)} \frac{d}{dt} i_{dc} + K_{ii}^{(0)} i_{dc} + K_{iv}^{(2)} \frac{d^2}{dt^2} v_{dc} + K_{iv}^{(1)} \frac{d}{dt} v_{dc} + K_{iv}^{(0)} v_{dc} = \tilde{v_{dc}} + R_2 I$$

$$(4.12)$$

where

$$
\begin{aligned}
K_{vv}^{(4)} &= [C_1 C_2 L_1 L_2] \\
K_{vv}^{(3)} &= [C_1 C_2 L_2 R_1 + C_1 C_2 L_1 R_2 + C_1 L_1 L_2 / R_3] \\
K_{vv}^{(2)} &= [C_1 C_2 R_1 R_2 + C_1 L_2 R_1 / R_3 + C_1 L_1 R_2 / R_3 + C_1 L_1 + C_2 L_1 + C_2 L_2] \\
K_{vv}^{(1)} &= [C_1 R_1 R_2 / R_3 + R_1 C_1 + R_1 C_2 + L_1 / R_3 + R_2 C_2 + L_2 / R_3] \\
K_{vv}^{(0)} &= [R_1 / R_3 + R_2 / R_3 + 1] \\
K_{ii}^{(1)} &= L_1 \\
K_{ii}^{(0)} &= R_1 \\
K_{iv}^{(2)} &= C_2 L_2 \\
K_{iv}^{(1)} &= C_2 R_2 + L_2 / R_3 \\
K_{iv}^{(0)} &= R_2 / R_3 + 1.
\end{aligned}
$$

DC Voltage Droop Control Equations

A robust solution to DC voltage management is PI droop control pictured in Figure 4-3. In this strategy, some current feedback is added to the voltage feedback to effectively preclude instability due to the control while accepting a small stationary voltage error. This method is especially effective with multiple generating units in parallel. The control also includes anti-windup at saturation.

Ignoring the anti-windup control and the control bias, the equation for the actuation of
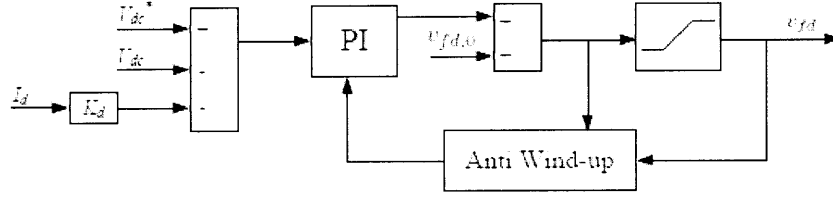
Figure 4-3: DC bus voltage droop control [49].

the field voltage is

$$\frac{d}{dt}v_{fd} = K_{p,v}(v_{dc}^* - v_{dc} - K_d i_{dc}) + K_{i,v} \int (v_{dc}^* - v_{dc} - K_d i_{dc})dt \qquad (4.13)$$

4.1.2 Motor Side Models

A process flow diagram for the system is shown in Figure 4.1.2. The main components are a three phase IM, IM torque control, an IGBT inverter, and a propeller.
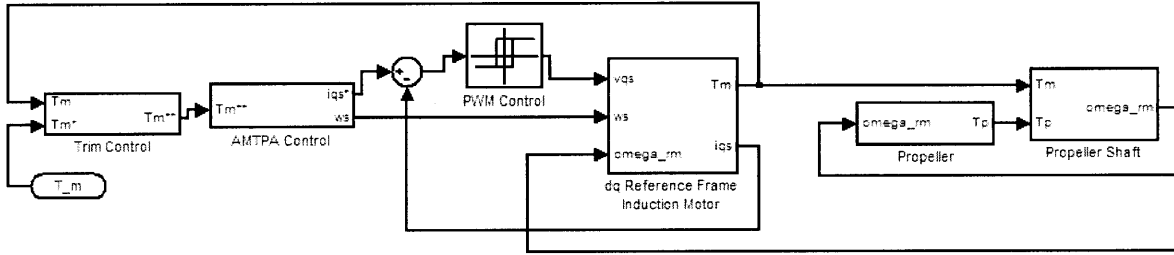
Figure 4-4: Motor-Propeller side process flow diagram.

As will be detailed below, the resulting open loop model involves a five state set of ordinary differential equations including 4 IM current states ($i_{m,qs}$ $i_{m,ds}$ $i_{m,qr}$ $i_{m,dr}$) and the propeller shaft speed ω_{rm}. The input to the system is the average voltage magnitude seen by the IM from the rectifier v_{qs}. A second adjustable input is the voltage source v_{dc} reflective of the operating condition for the generator side; however, in this analysis, it will be assumed that v_{dc} cannot be actuated.

For the closed loop system, one state is added, the time derivative of the measured torque. The input becomes user specified torque command T_m^*.

71

Motor Equations

The IM mathematical equations in the rotor DQ reference frame [40] are

$$p\lambda_{m,qs} = v_{m,qs} - r_s i_{m,qs} - \omega_e \lambda_{m,ds} \qquad (4.14)$$

$$p\lambda_{m,ds} = v_{m,ds} - r_s i_{m,ds} + \omega_e \lambda_{m,qs}$$

$$p\lambda_{m,qr} = -r_r i_{m,qr} - w_s \lambda_{m,dr}$$

$$p\lambda_{m,dr} = -r_r i_{m,dr} + w_s \lambda_{m,qr}$$

$$\lambda_{m,qs} = L_s i_{m,qs} + L_m i_{m,qr} \qquad (4.15)$$

$$\lambda_{m,qs} = L_s i_{m,ds} + L_m i_{m,dr}$$

$$\lambda_{m,qs} = L_r i_{m,qr} + L_m i_{m,qs}$$

$$\lambda_{m,qs} = L_r i_{m,dr} + L_m i_{m,ds}.$$

where λ are magnetic fluxes, v are voltages, and i are currents. r and L are resistances and inductances, respectively. The subscript denotes the d or q reference frame and the stator (s) or rotor (r).

After manipulation, the equations can be stated with current states as

$$\frac{d}{dt}\begin{bmatrix} i_{m,qs} \\ i_{m,ds} \\ i_{m,qr} \\ i_{m,dr} \end{bmatrix} = M_m^{-1} A_m \begin{bmatrix} i_{m,qs} \\ i_{m,ds} \\ i_{m,qr} \\ i_{m,dr} \end{bmatrix} + M_m^{-1} \begin{bmatrix} 1 \\ 0 \\ 0 \\ 0 \end{bmatrix} v_{m,qs} \qquad (4.16)$$

where

$$M_m = \begin{bmatrix} L_s & 0 & L_m & 0 \\ 0 & L_s & 0 & L_m \\ L_m & 0 & L_r & 0 \\ 0 & L_m & 0 & L_r \end{bmatrix} \tag{4.17}$$

and

$$A_m = \begin{bmatrix} -r_s & -\omega_e L_s & 0 & -\omega_e L_m \\ \omega_e L_s & -r_s & \omega_e L_m & 0 \\ 0 & -\omega_s L_m & -r_r & -\omega_s L_r \\ \omega_s L_m & 0 & \omega_s L_r & -r_r \end{bmatrix}. \tag{4.18}$$

In these equations, the IM excitement frequency is $\omega_e = \omega_r + \omega_s$, where $\omega_r = \frac{P_m}{2}\omega_{rm}$ is the electrical rotor frequency and ω_s is the slip frequency. For this stability analysis, the actuation dynamics of ω_s via the IGBT inverter will be assumed much faster than the system so the actual slip frequency is set equivalent to the command slip freuqency from the AMTPA control: $\omega_s \equiv \omega_s^*$.

Note: equation 4.16 is formulated assuming the our rotating reference frame is offset such that the stator d-reference frame voltage $v_{m,ds}$ is always zero [57].

Propeller Equations

A traditional quadratic model is used for the propeller.

$$T_p = k_{q0}\rho D^5 n_p^2 \tag{4.19}$$

Here, $k_{q0} = 0.05$ is the zero speed, open water, torque coefficient for a Waginingen B-Series propeller. n_p is the propeller shaft speed, in Hz. D is the propeller diameter.

The governing equation for the propeller shaft speed, with the IM torque equation substituted [40], is

$$I_p \frac{d\omega_{rm}}{dt} = T_m - T_p = \frac{3P_m}{4} L_m (i_{m,qs} i_{m,dr} - i_{m,qr} i_{m,ds}) - T_p \tag{4.20}$$

where I_p is selected to preserve similitude with respect to the dimensionless propeller number $\rho D_5 / I_p$, as compared to generic marine propeller data on hand.

Induction Motor Torque Control Equations

The control of the induction motor torque is accomplished in three parts. Torque trim control, AMTPA control, and current hysteresis control.

The torque trim control, Figure 4-5, uses the integral of torque feedback error to adjust the torque reference signal T_m^{**}, ensuring tracking between the measured torque T_m and the command torque T_m^*. The control also includes anti-windup control at saturation.
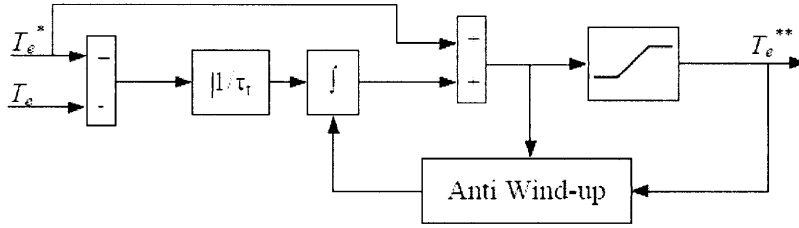
Figure 4-5: Torque trim controller [49].

Without anti-windup control, the control equation is

$$\tau \frac{d}{dt} T_m^{**} = -\frac{1}{\tau} \left(\frac{3P_m}{4} L_m (i_{m,qs} i_{m,dr} - i_{m,qr} i_{m,ds}) \right) + \frac{1}{\tau} T_m^* + \frac{d}{dt} T_m^*. \tag{4.21}$$

Based on the torque reference signal T_m^{**}, the AMTPA control computes the current reference magnitude signal I^* and the slip frequency ω_s^*, informed by the inverse of the induction motor equations. The current reference signal is computed

$$I^* = \sqrt{i_{m,qs}^* + i_{m,ds}^*} = \sqrt{\frac{4 T_m^{**} (r_r'^2 + (\omega_s L_r')^2)}{3 P_m \omega_s L_m'^2 r_r'}} \tag{4.22}$$

74

where the prime symbol denotes that the parameter is estimated from existing knowledge of the IM.

The slip frequency is set as a constant $\omega_{s,set}$ when $T_m^{**} < T_{m,thres}$, where

$$T_{m,thres} = \frac{3P_m}{2}\frac{\omega_{s,set}\lambda_{r,max}^2}{r_r'} \tag{4.23}$$

with $\lambda_{r,max}$ as the maximum allowable rotor flux. For operating conditions requiring a reference torque signal beyond the torque threshold, the slip frequency is altered according to

$$\omega_s^* = \frac{2T_m^{**}r_r'}{3\lambda_{r,max}^2}. \tag{4.24}$$

Current hysteresis control is used to control the voltage feeding the motor. Current hysteresis is a modern technique for delivering power in variable magnitudes and wave forms by alternating the power source from fully ON and fully OFF extremely rapidly [52]; in general, the bandwidth of the load is far lower than that of the power electronics which execute the switching, and so the load experiences the average voltage output.

In the case of the Purdue MVDC Testbed, three phase control is required. The inverter is fed by a DC voltage source and the six IGBT bridge topology allows for the independent control of each phase. Specifically, some acceptable error δ_h is specified. When a measured current phase exceeds the reference signal phase by δ_h, the voltage to that phase is adjusted such that the current changes direction; the same is true for when the reference signal phase exceeds the measured current phase by δ_h. δ_h determines the switching frequency of the IGBTs. Figure 4-6 shows the voltage and current dynamics for a single phase during simulation of the high fidelity model.

4.2 Steady State Linearization

In this section, procedures are outlined for solving for open loop equilibrium points of the generator and motor sides, for any given input values. Then, small displacement theory is employed to linearize the system equations about the equilibrium point. The open loop linear state space matrices are presented in Section 4.3.
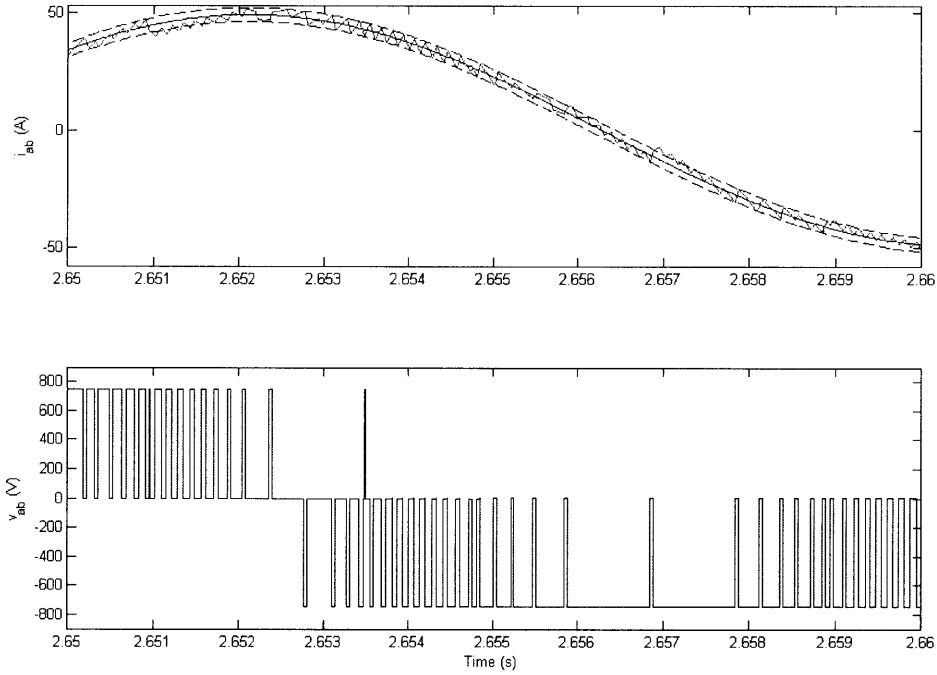
Figure 4-6: Dynamics of current hysteresis control for a phase: a) Resulting induction motor current for a single phase and b) the stator voltage for the same phase.

4.2.1 Generator Side Linearization

A steady-state solution is found for the generator side nonlinear DAEs by setting all time derivatives to zero and solving. The subscript 0 will be used to denote the steady states. The solution requires input values for command rotor electrical speed ω^*, SM field voltage v_{fd}, and the inverter current sink I.

For this tool, steady state solutions are found at a user-specified constant rotor speeds assuming that the PI control will effectively reach it ($\omega_{t0} \equiv \omega_t^*$) and the controlled turbine dynamics are taken into account in the linearization stages to follow. The generator equations

4.3 become

$$
M_g^{-1} A_g(\omega_{t0})
\begin{bmatrix}
i_{g,qs0} \\
i_{ds0} \\
i_{g,qr0} \\
i_{g,dr0} \\
i_{fd0}
\end{bmatrix}
= -M_g^{-1}
\begin{bmatrix}
1 & 0 & 0 \\
0 & 1 & 0 \\
0 & 0 & 0 \\
0 & 0 & 0 \\
0 & 0 & 1
\end{bmatrix}
\begin{bmatrix}
v_{g,qs0} \\
v_{g,ds0} \\
v_{fd}
\end{bmatrix}.
\tag{4.25}
$$

The rectifier equations must be satisfied:

$$
v_{\tilde{dc}0} = \frac{3\sqrt{3}}{\pi} \sqrt{v_{g,qs0}^2 + v_{ds0}^2} \cos\alpha - \frac{3}{\pi} X_{co} i_{dc0}
\tag{4.26}
$$

$$
v_{g,qs0} i_{g,qs0} + v_{ds0} i_{ds0} = \frac{2}{3} v_{\tilde{dc}0} i_{dc0} \cos\phi
$$

$$
v_{g,qs0} i_{ds0} - v_{ds0} i_{g,qs0} = \frac{2}{3} v_{\tilde{dc}0} i_{dc0} \sin\phi.
\tag{4.27}
$$

The filter equations 4.12 reduce to

$$
\begin{bmatrix}
R_1/R_3 + R_2/R_3 + 1 & 0 \\
R_2/R_3 + 1 & R_1
\end{bmatrix}
\begin{bmatrix}
v_{dc0} \\
i_{dc0}
\end{bmatrix}
=
\begin{bmatrix}
1 & -(R_1 + R_2) \\
1 & R_2
\end{bmatrix}
\begin{bmatrix}
v_{\tilde{dc}0} \\
I
\end{bmatrix}.
\tag{4.28}
$$

This set of equations can be solved with MATLAB's *fsolve* command which implements a trust region dogleg algorithm for square nonlinear systems of equations.

Table 4.1 compares the filtered/averaged results for a Purdue MVDC Testbed simulation with the steady-state solution of this tool for a baseline condition, $\omega^* = 377$ rad/s, $v_{fd} = 28.5$V, and $I = 45$A. The error is likely due to the higher order harmonics involved in the high fidelity simulation.

The value of X_{co} is estimated numerically, adjusting it until the the predicted steady state voltage pair (v_{fd}, v_{dc0}) matches the results with the high fidelity simulator. At the baseline condition, X_{co} was found to be 0.323 Ω. For operating conditions far from this baseline condition, X_{co} can be re-estimated but testing has shown only a few percentage error in the

	High Fidelity Simulation Results	Steady-State Solution
$\sqrt{v_{g,qs}^2 + v_{g,ds}^2}$	450.49 V	457.74 V
$\sqrt{i_{g,qs}^2 + i_{g,ds}^2}$	46.82 A	48.81 A
i_{fd}	107.28 A	108.75 A
$\tilde{v}_{dc}$	743.73	743.17 V
i_{dc}	42.54	45.09 A
$\cos\phi$	1.000	0.982

Table 4.1: Comparison of generator side steady state solutions for analytical tool and high fidelity simulation.

steady state solution if X_{co} is held at 0.323 Ω, for a variety of operating conditions.

The nonlinear nature of generator model and the power conservation constraints across the rectifier impedes the use of traditional stability analysis methods. To overcome this, the stability analysis is conducted about a linearized operating condition justified by small displacement theory [43]. Let Δ be used to denote small displacements from the steady state. The generator equations combined with the controlled turbine equations become:

$$
\begin{bmatrix}
& & & & & 0 & 0 \\
& & & & & 0 & 0 \\
& & M_g & & & 0 & 0 \\
& & & & & 0 & 0 \\
& & & & & 0 & 0 \\
\hline
0 & 0 & 0 & 0 & 0 & I_{shaft} & 0 \\
0 & 0 & 0 & 0 & 0 & 0 & 1
\end{bmatrix}
\frac{d}{dt}
\begin{bmatrix}
\Delta i_{g,qs} \\
\Delta i_{g,ds} \\
\Delta i_{g,qr} \\
\Delta i_{g,dr} \\
\Delta i_{fd} \\
\hline
\Delta \omega_t \\
\int \Delta \omega_t dt
\end{bmatrix}
\qquad (4.29)
$$

$$
=
\begin{bmatrix}
& & & & & K_{i_{g,qs}\omega} & 0 \\
& & & & & K_{i_{g,ds}\omega} & 0 \\
& & A_g(\omega_{t0}) & & & 0 & 0 \\
& & & & & 0 & 0 \\
& & & & & 0 & 0 \\
\hline
K_{\omega i_{g,qs}} & K_{\omega i_{g,ds}} & K_{\omega i_{g,qr}} & K_{\omega i_{g,dr}} & K_{\omega i_{fd}} & -K_{p,t} & -K_{i,t} \\
0 & 0 & 0 & 0 & 0 & 1 & 0
\end{bmatrix}
\begin{bmatrix}
\Delta i_{g,qs} \\
\Delta i_{g,ds} \\
\Delta i_{g,qr} \\
\Delta i_{g,dr} \\
\Delta i_{fd} \\
\hline
\Delta \omega_t \\
\int \Delta \omega_t dt
\end{bmatrix}
$$

$$
+
\begin{bmatrix}
1 & 0 & 0 \\
0 & 1 & 0 \\
0 & 0 & 0 \\
0 & 0 & 0 \\
0 & 0 & 1 \\
0 & 0 & 0
\end{bmatrix}
\begin{bmatrix}
\Delta v_{g,qs} \\
\Delta v_{g,ds} \\
\Delta v_{fd}
\end{bmatrix}
$$

where

$$K_{i_{g,qs}\omega} = \frac{P_g}{2}\left(i_{ds0}(L_{ls} + L_{md}) - (i_{g,qr0} + i_{fd0})L_{md}\right)$$

$$K_{i_{g,ds}\omega} = \frac{P_g}{2}\left(-i_{g,qs0}(L_{ls} + L_{mq}) + i_{g,dr0}L_{mq}\right)$$

$$K_{\omega i_{g,qs}} = -\frac{3P_g}{4}\left(i_{ds0}(L_{mq} - L_{md}) + (i_{g,dr0} + i_{fd0})L_{md}\right)$$

$$K_{\omega i_{g,ds}} = -\frac{3P_g}{4}\left(i_{g,qs0}(L_{mq} - L_{md}) - i_{g,qr0}L_{mq}\right)$$

$$K_{\omega i_{g,qr}} = \frac{3P_g}{4}i_{ds0}L_{mq}$$

$$K_{\omega i_{g,dr}} = -\frac{3P_g}{4}i_{g,qs0}L_{md}$$

$$K_{\omega i_{fd}} = -\frac{3P_g}{4}i_{g,qs0}L_{md}$$

and $A_g(\omega_0)$ is the matrix in Eq. 4.5 with $\omega = \omega*$.

The filter model matrices do not change because of the inherent linearity of the circuit; however, the states become small displacements from the operating steady state and the I terms disappear because I is assumed constant.

Finally, the rectifier constraint equations 4.8-4.10 need to be linearized and solved so as to replace $[\Delta \tilde{v}_{dc}, \Delta v_{g,qs}, \Delta v_{g,ds}]$ with linear functions of $[\Delta i_{g,qs}, \Delta i_{g,ds}, \Delta i_{dc}]$. Sparing no detail, the result is

$$
\begin{bmatrix}
K_{\tilde{v}_{dc}1} & K_{v_{g,qs}1} & K_{v_{g,ds}1} \\
K_{\tilde{v}_{dc}2} & K_{v_{g,qs}2} & K_{v_{g,ds}2} \\
K_{\tilde{v}_{dc}3} & K_{v_{g,qs}3} & K_{v_{g,ds}3}
\end{bmatrix}
\begin{bmatrix}
\Delta \tilde{v}_{dc} \\
\Delta v_{g,qs} \\
\Delta v_{g,ds}
\end{bmatrix}
=
\begin{bmatrix}
0 & 0 & -\frac{3}{\pi}X_{co} \\
v_{g,qs0} & v_{ds0} & -\frac{2}{3}\tilde{v}_{dc0}\cos\phi_0 \\
-v_{ds0} & v_{g,qs0} & -\frac{2}{3}\tilde{v}_{dc0}\sin\phi_0
\end{bmatrix}
\begin{bmatrix}
\Delta i_{g,qs} \\
\Delta i_{g,ds} \\
\Delta i_{dc}
\end{bmatrix}
\quad (4.30)
$$

where

$$K_{v_{\tilde{dc}}1} = 1$$

$$K_{v_{g,qs}1} = -\frac{3\sqrt{3}}{\pi}V_0^{-1/2}v_{g,qs0}$$

$$K_{v_{g,ds}1} = -\frac{3\sqrt{3}}{\pi}V_0^{-1/2}v_{ds0}$$

$$K_{v_{\tilde{dc}}2} = \frac{4}{3}i_{dc0}\cos\phi_0$$

$$K_{v_{g,qs}2} = -i_{g,qs0} - \frac{2\pi}{9\sqrt{3}}i_{dc0}v_{\tilde{dc}0}{}^2 v_{g,qs0}/V_0^{3/2}$$

$$K_{v_{g,ds}2} = -i_{g,qs0} - \frac{2\pi}{9\sqrt{3}}i_{dc0}v_{\tilde{dc}0}{}^2 v_{ds0}/V_0^{3/2}$$

$$K_{v_{\tilde{dc}}3} = \frac{2}{3}i_{dc0}\sin\phi_0 - \frac{2\pi^2}{81}i_{dc0}v_{\tilde{dc}0}{}^2 \sin^{-1}(\phi_0)/V_0$$

$$K_{v_{g,qs}3} = -i_{ds0} + \frac{2\pi^2}{81}i_{dc0}v_{\tilde{dc}0}{}^3 \sin^{-1}(\phi_0)v_{g,qs0}/V_0^2$$

$$K_{v_{g,ds}3} = i_{g,qs0} + \frac{2\pi^2}{81}i_{dc0}v_{\tilde{dc}0}{}^3 \sin^{-1}(\phi_0)v_{ds0}/V_0^2$$

where

$$V_0 = v_{g,qs0}^2 + v_{g,ds0}^2$$

$$\phi_0 = \cos^{-1}\left(\frac{\pi}{3\sqrt{3}}\frac{v_{\tilde{dc}0}}{\sqrt{V_0}}\right).$$

After solving this set of linear equations, substitution can be made into the generator and filter small displacement equations and linear state space matrices can constructed. These will be assessed in Section 4.3.

4.2.2 Motor Side Linearization

The steady state solution for the IM side is less straightfoward than the generator side because it attempts to solve for the steady state of system with the influence of closed loop torque control. The solution requires input values for the command torque T_m^* and the constant DC

bus voltage v_{dc}. A step-by-step procedure is described here.

I Assume that at steady state the torque command is reached due to the integral control of the torque trim controller. With this assumption, the steady state rotor speed can be computed:

$$k_{q0}\rho D^5 \left(\frac{\omega_{rm0}}{\pi P_m}\right)^2 = T_m^*. \tag{4.31}$$

II With a torque signal T_m^{**}, the AMTPA control equations are used to compute the desired command slip frequency and stator current magnitude, ω_s^* and I^*. For the first iteration, use the guess $T_m^{**} = T_m^*$.

III Then, it is assumed that the current hysteresis is such that ω_s^* and I^* are attained at steady state (in a time averaged sense), enforced by the state constaints

$$
\begin{aligned}
i_{m,qs0}^2 + i_{m,ds0}^2 &= I^{*2} \\
\omega_{e0} &= \omega_s^* + \frac{P_m}{2}\omega_{rm0}
\end{aligned}
\tag{4.32}
$$

IV Now, with all time derivatives set to zero in Eq. 4.16, the IM steady states can be solved for.

$$A_m(\omega_{e0}, \omega_{s0}) \begin{bmatrix} i_{m,qs0} \\ i_{m,ds0} \\ i_{m,qr0} \\ i_{m,dr0} \end{bmatrix} = \begin{bmatrix} 1 \\ 0 \\ 0 \\ 0 \end{bmatrix} v_{m,qs} \tag{4.33}$$

where $A_m(\omega_{e0}, \omega_{s0})$ is Eq. 4.18 computed at ω_{e0} and ω_{s0}.

Recall, only the q-axis stator voltage is used because the reference frame is offset such that $v_{m,ds}(t) = 0$ for all t. The solved value for $v_{m,qs}$ is the continuous time averaged value of the actual signal.

V Finally, compute the measured torque at the predicted steady state, T_{m0}. If it is not equal to the command torque, T_m^{**} must be adjusted and steps are repeated from step II. If the AMTPA parameter estimates are identical to the IM parameters, no iteration should be required.

Table 4.2 shows a comparison between results for this steady state solver and the filtered results from the Purdue MVDC Testbed, for a torque command of 100 Nm. Notice the error in the voltage applied to the motor; this is a product of the assumption of a continuous voltage as compared to the discontinuous signal in the high fidelity model, leading to the exclusion of the effects of the square wave harmonics.

	High Fidelity Simulation Results	Steady State Solution
T_m^*	100.0 Nm	100.0 Nm
T_{m0}	99.33 Nm	100.0 Nm
T_{m0}^{**}	101.6 Nm	100.0 Nm
ω_{r0}	377.0 rad/s	377.0 rad/s
ω_{s0}	1.667 rad/s	1.667 rad/s
$\sqrt{i_{m,qs0}^2 + i_{m,ds0}^2}$	47.78 A	47.80
$\sqrt{i_{m,qr0}^2 + i_{m,dr0}^2}$	32.23 A	32.38
$\sqrt{v_{m,qs0}^2 + v_{m,ds0}^2}$	431.06 V	411.91

Table 4.2: Comparison of motor side steady state solutions for analytical tool and high fidelity simulation.

Since both ω_r and ω_s can be time variant, the IM equations in 4.16 are second-order non-linear. Again, to overcome this, the stability analysis is conducted about the solved linearized operating condition justified by small displacement theory.

The lineared current equations become

$$M_m \frac{d}{dt} \begin{bmatrix} \Delta i_{qs} \\ \Delta i_{ds} \\ \Delta i_{qr} \\ \Delta i_{dr} \end{bmatrix} = A_m(\omega_{e0}, \omega_{s0}) \begin{bmatrix} \Delta i_{qs} \\ \Delta i_{ds} \\ \Delta i_{qr} \\ \Delta i_{dr} \end{bmatrix} \tag{4.34}$$

$$+ \begin{bmatrix} -\frac{P_m}{2}(L_s i_{m,ds0} + L_m i_{m,dr0}) & -(L_s i_{m,ds0} + L_m i_{m,dr0}) \\ \frac{P_m}{2}(L_s i_{m,qs0} + L_m i_{m,qr0}) & (L_s i_{m,qs0} + L_m i_{m,qr0}) \\ 0 & -(L_m i_{m,ds0} + L_r i_{m,dr0}) \\ 0 & (L_m i_{m,qs0} + L_r i_{m,qr0}) \end{bmatrix} \begin{bmatrix} \Delta \omega_{rm} \\ \Delta \omega_s \end{bmatrix}$$

The linearized propeller equation is

$$I_p \frac{d}{dt} \Delta \omega_{rm} = \frac{3P_m}{4} L_m \big(i_{m,dr0} \Delta i_{m,qs} - i_{m,qr0} \Delta i_{m,ds} - i_{m,ds0} \Delta i_{m,qr} \tag{4.35}$$

$$+ \; i_{m,qs0} \Delta i_{m,dr} \big) - 2 k_{q0} \rho D^5 \left(\frac{1}{2\pi} \right)^2 \omega_{rm0} \Delta \omega_{rm}.$$

The governing equation for torque trim control reference signal becomes

$$\frac{d}{dt} \Delta T_m^{**} = -\frac{1}{\tau} \frac{3P_m}{4} L_m (i_{m,dr0} \Delta i_{m,qs} - i_{m,qr0} \Delta i_{m,ds} - i_{m,ds0} \Delta i_{m,qr} + i_{m,qs0} \Delta i_{m,dr}) + \frac{1}{\tau} \Delta T_m^* + \Delta \frac{d}{dt} T_m^*. \tag{4.36}$$

The linearized AMTPA current magnitude control is

$$\Delta I^* = \begin{cases} (T_{m0}^{**})^{-1/2} \sqrt{\frac{r_r'^2 + (\omega_{s,set} L_r')^2}{3 P_m \omega_{s,set} L_m'^2 r_r'}} \Delta T_m^{**}, & \text{if } T_m^{**} \leq T_{m,thres} \\ \frac{4 L_r'^2}{9 P_m^2 L_m' \lambda_{r,max}^2} \left(\lambda_{r,max}^2 + \frac{4 L_r'^2}{9 P_m^2 \lambda_{r,max}} T_{m0}^{**} \right)^{-1/2} T_{m0}^{**} \Delta T_m^{**}, & \text{if } T_m^{**} > T_{m,thres}. \end{cases} \tag{4.37}$$

and

$$\Delta\omega_s^* = \begin{cases} 0, & \text{if } T_m^{**} \leq T_{m,thres} \\[2ex] \frac{2r_r'}{3P_m\lambda_{r,max}^2}\Delta T_m^{**}, & \text{if } T_m^{**} > T_{m,thres}. \end{cases} \tag{4.38}$$

4.3 Open Loop Analysis

In this section, the linearized equations are combined to create open loop state space matrices for both the generator and motor sides. Analytical transfer functions, $G(s) = C(sI - A)^{-1}B$, are visualized with Bode magnitude plots. For comparison, frequency response plots have been attained from high fidelity simulation at discrete frequencies.

4.3.1 Generator Side Open Loop Analysis

Equations 4.29 and 4.30 can be combined with the linearized version of Eq. 4.11 to produce a linear state space model for the generator side:

$$\begin{aligned} \frac{d\Delta x}{dt} &= A_{g,ol}\Delta x + B_{g,ol}\Delta u \\ y &= C_{g,ol}\Delta x \end{aligned} \tag{4.39}$$

$$x = \begin{bmatrix} i_{g,qs} & i_{g,ds} & i_{g,qr} & i_{g,dr} & i_{g,fd} & \omega_t & \int \omega_t dt & v_{dc}^{(3)} & v_{dc}^{(2)} & v_{dc}^{(1)} & v_{dc} & i_{dc} \end{bmatrix} \tag{4.40}$$

where $v_{dc}^{(i)}$ denotes the ith time derivative of the bus voltage.

If $u = v_{fd}$, the B matrix is

$$B_{g,ol} = \begin{bmatrix} M_g^{-1} \begin{bmatrix} 0 \\ 0 \\ 0 \\ 0 \\ \frac{n_s}{n_{fd}} \end{bmatrix} \\ \mathbf{0_{7x1}} \end{bmatrix}. \tag{4.41}$$

If y is the droop feedback, the C matrix is

$$C_{g,ol} = \begin{bmatrix} 0 & 0 & 0 & 0 & 0 & 0 & 0 & 0 & 0 & 1 & K_D \end{bmatrix} \tag{4.42}$$

A Bode plot of the resulting transfer function is shown in Figure 4-7, for a baseline condition of $T_m^* = 100$ Nm. The stars show results of the high fidelity simulation; this baseline trial provides a very good argument for the validity of the model presented in this report.
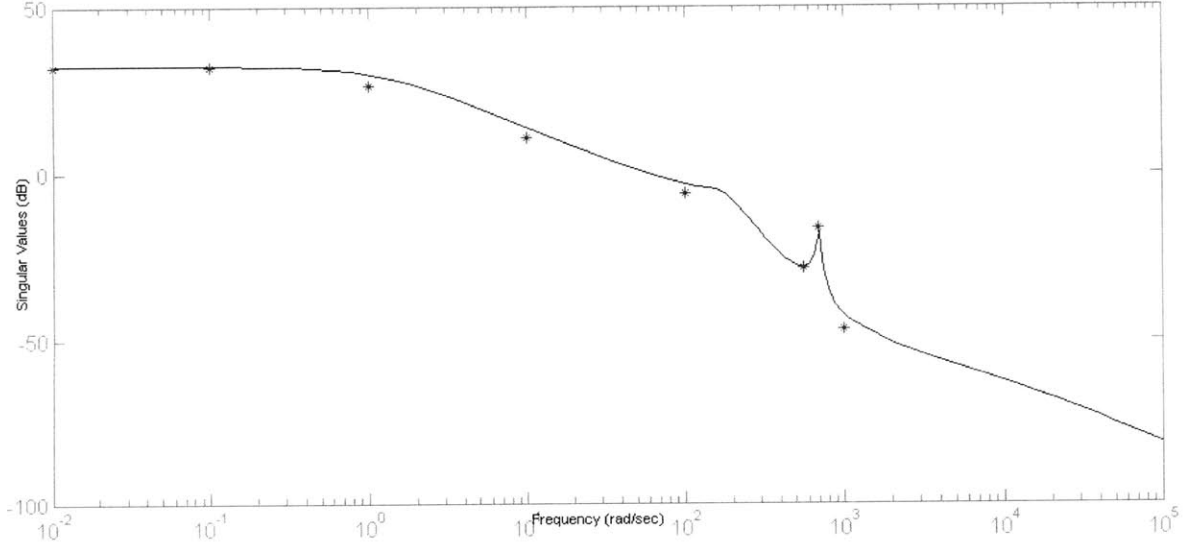

Figure 4-7: Bode plot for the generator side with field voltage input and droop feedback output for baseline operating conditions, $T_m^* = 100$ Nm. Stars indicate high fidelity simulation results.

4.3.2 Motor Side Open Loop Analysis

Equations 4.34 and 4.35 can be combined to produce a linear state space model for the motor side when the torque command does not exceed the torque threshold. When the torque threshold is exceeded, Equations 4.36 and 4.38 must be incorporated to include the dynamics of the IM slip frequency. The general linear state space model is

$$\frac{d\Delta x}{dt} = A_{m,ol}\Delta x + B_{m,ol}\Delta u \tag{4.43}$$
$$y = C_{m,ol}\Delta x.$$

where u is the the stator voltage magnitude and y is the current magnitude feedback.

When $T_m^{**} \leq T_{m,thres}$, the states are $x = [\ i_{m,qs} \quad i_{m,ds} \quad i_{m,qr} \quad i_{m,dr} \quad \omega_{rm} \ ]$ and the A matrix is

$$A_{m,ol} =
\begin{bmatrix}
& & & 0 \\
& M_m & & 0 \\
& & & 0 \\
& & & 0 \\
\hline
0 & 0 & 0 & 0 & I_p
\end{bmatrix}^{-1}
\tag{4.44}$$

$$
\begin{bmatrix}
& & & -\frac{P_m}{2}\left(L_s i_{m,ds0} + L_m i_{m,dr0}\right) \\
& A_m(\omega_{e0}, \omega_{s0}) & & \frac{P_m}{2}\left(L_s i_{m,qs0} + L_m i_{m,qr0}\right) \\
& & & 0 \\
& & & 0 \\
\hline
\frac{3P_m L_m}{4}i_{m,dr0} & -\frac{3P_m L_m}{4}i_{m,qr0} & -\frac{3P_m L_m}{4}i_{m,ds0} & \frac{3P_m L_m}{4}i_{m,qs0} & -2k_{q0}\rho D^5\left(\frac{1}{2\pi}\right)^2\omega_{rm0}
\end{bmatrix}.
$$

The B matrix for the input $\Delta v_{m,qs}$ is

$$
B_{m,ol} = \left[\begin{array}{cccc|c} & & & & 0 \\ & \multicolumn{3}{c}{M_m} & 0 \\ & & & & 0 \\ & & & & 0 \\ \hline 0 & 0 & 0 & 0 & I_p \end{array}\right]^{-1} \left[\begin{array}{c} 1 \\ 0 \\ 0 \\ 0 \\ 0 \end{array}\right] \tag{4.45}
$$

The feedback for the system is the magnitude of the stator current $\sqrt{i_{m,qs}^2 + i_{m,ds}^2}$. For the linearized system, the open loop C matrix is $C_{m,ol} = (i_{m,qs0}^2 + i_{m,ds0}^2)^{-1/2}[i_{m,qs} \; i_{m,ds} \; 0 \; 0 \; 0]$.

When $T_m^{**} > T_{m,thres}$, a state is added for the trim control, T_m^{**}. The A matrix is

$$
A_{m,ol} = \left[\begin{array}{cccccc} & & & & 0 & 0 \\ & \multicolumn{3}{c}{M_m} & 0 & 0 \\ & & & & 0 & 0 \\ & & & & 0 & 0 \\ 0 & 0 & 0 & 0 & I_p & 0 \\ 0 & 0 & 0 & 0 & 0 & \tau \end{array}\right]^{-1} \tag{4.46}
$$

$$
\left[\begin{array}{cccc} & & & -\frac{P_m}{2}(L_s i_{m,ds0}+L_m i_{m,dr0}) \quad -\frac{2r_r'}{3P_m\lambda_{r,max}^2}(L_s i_{m,ds0}+L_m i_{m,dr0}) \\ & A_m(\omega_{e0},\omega_{s0}) & & \frac{P_m}{2}(L_s i_{m,qs0}+L_m i_{m,qr0}) \quad \frac{2r_r'}{3P_m\lambda_{r,max}^2}(L_s i_{m,qs0}+L_m i_{m,qr0}) \\ & & 0 & -\frac{2r_r'}{3P_m\lambda_{r,max}^2}(L_m i_{m,ds0}+L_r i_{m,dr0}) \\ & & 0 & \frac{2r_r'}{3P_m\lambda_{r,max}^2}(L_m i_{m,qs0}+L_r i_{m,qr0}) \\ \frac{3P_m L_m}{4}i_{m,dr0} \; -\frac{3P_m L_m}{4}i_{m,qr0} \; -\frac{3P_m L_m}{4}i_{m,ds0} \; \frac{3P_m L_m}{4}i_{m,qs0} & -2k_{q0}\rho D^5\left(\frac{1}{2\pi}\right)^2\omega_{rm0} & 0 \\ \frac{3P_m L_m}{4}i_{m,dr0} \; -\frac{3P_m L_m}{4}i_{m,qr0} \; -\frac{3P_m L_m}{4}i_{m,ds0} \; \frac{3P_m L_m}{4}i_{m,qs0} & 0 & 0 \end{array}\right].
$$

Assuming that the torque command T_m^* is held constant, the B matrix is only augmented by one zero

$$
B_{m,ol} = \left[\begin{array}{cccc|c|c} & & & & 0 & 0 \\ & \multicolumn{3}{c}{M_m} & 0 & 0 \\ & & & & 0 & 0 \\ & & & & 0 & 0 \\ \hline 0 & 0 & 0 & 0 & I_p & 0 \\ \hline 0 & 0 & 0 & 0 & 0 & \tau \end{array}\right]^{-1} \left[\begin{array}{c} 1 \\ 0 \\ 0 \\ 0 \\ 0 \\ 0 \end{array}\right]. \tag{4.47}
$$

The C matrix in augmented with one zero $C_{m,ol} = (i_{m,qs0}^2 + i_{m,ds0}^2)^{-1/2}[i_{m,qs} \; i_{m,ds} \; 0 \; 0 \; 0 \; 0]$.

Figure 4-8: Bode plot for motor-propeller with stator voltage input and stator current magnitude feedback for the output, for a 100 Nm operating condition. Stars indicate Purdue MVDC Testbed model results.

For validation purposes, a Bode plot is shown in Figure 4.3.2 for the operating point open loop transfer function, for a baseline torque command of 100 Nm. Figure 4.3.2 shows the results for a torque command of 200 Nm. Notice that the five state model does not capture the frequency domain behavior exactly when operating above the torque command threshold.

4.4 Closed Loop Analysis

This section investigates methods for closed loop analysis of the generator and motor sides. Generator analysis is trivial due to its PI compensation. The motor side deserves more attention due to its more complex compensator. One method is introduced for this analysis.

4.4.1 Generator Side Closed Loop Analysis

In the case of PI control, the closed loop A matrix becomes [33]

$$A_{g,cl} = \begin{bmatrix} A_{g,ol} - B_{g,ol}K_{p,v}C_{g,ol} & B_{g,ol}K_{i,v} \\ -C_{g,ol} & 0 \end{bmatrix} \tag{4.48}$$
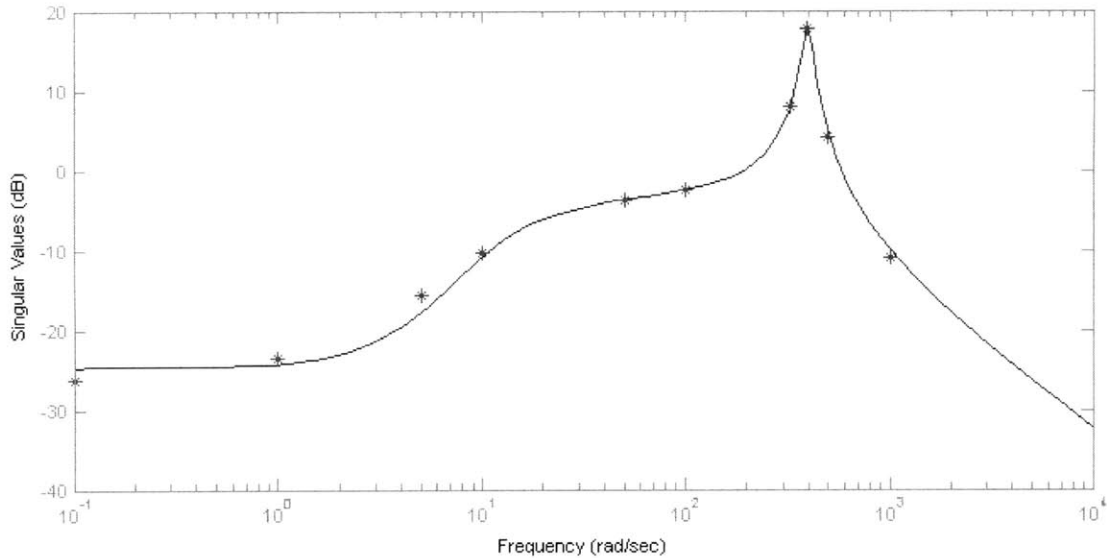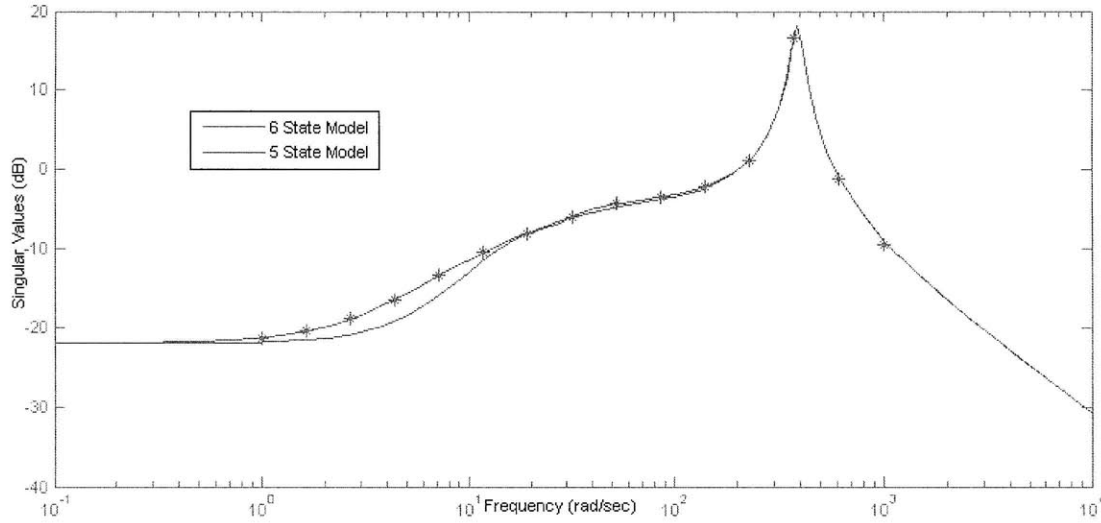
89

Figure 4-9: Bode plot for motor-propeller with stator voltage input and stator current magnitude feedback for the output, for a 200 Nm operating condition. Stars stars indicate Purdue MVDC Testbed model results.

where $K_{p,v}$ and $K_{i,v}$ are the droop gains.

Note that this representation introduces a new state derivative to the system: the integral of the feedback combination. This can be used to inspect the poles of the closed loop system.

As an example of frequency domain analysis, one can examine the closed loop command following transfer function $H(s) = K(s)G(s)/(1 + K(s)G(s))$, where $K(s)$ is the compensator transfer function. The classic PI compensator, $K(s) = \frac{K_p s + K_i}{s}$, is the default for the Purdue MVDC Testbed droop control.

For more results, see [64].

4.4.2 Motor Side Closed Loop Analysis

Methods for the closed loop analysis of the motor side require a more novel approach due to the hysteretic relays in the control loop. The three phase current hysteresis control is shown in Figure 4-10.

The three phase control problem is intractable for several reasons, the primary of which is that the open loop model was developed in the dq reference frame. Instead, a generalized combined phase, or current magnitude, hysteresis control will be used in place of the three phase control, see Figure 4-11. The current magnitude is the feedback from the open loop
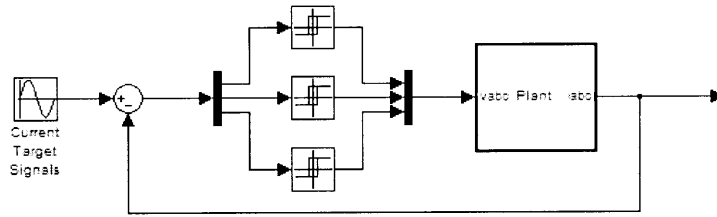
Figure 4-10: Three phase hysteresis current control for IM torque management.
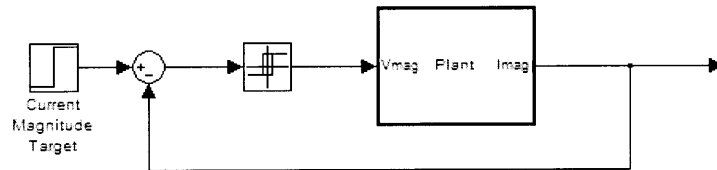

Figure 4-11: A generalized combined phase hysteresis control.

models developed in the previous section, the voltage magnitude is simply $v_{m,qs}$ because of how the rotating reference frame was defined in Section 4.1. This approximation may not capture all of the dynamics of the three phase compensation, but it is used here as a starting point.

The combined phase feedback model falls into the control theory category of sliding mode control [39]. Work during this thesis and other studies have shown that traditional describing function methods [27], with their first order approximations, are not reliable for for this type of compensation [17]. Two methods are presented in [64] for analysis of this system type. Here, only one is developed.

"The classical approach to analysing the closed-loop response of a system under sliding-mode control is to seek a smooth control law that approximates the effects of the rapidly switching control observed under digital implementation" [12]. Several different approaches can be taken to attain the equivalent control law. In the method presented here, $v_{m,qs}$ is instantaneously set to the value predicted by the inverse steady IM equations, to satisfy a torque command of T_m^{**}. This is a continuous analog to the rapid adjustment being made by the hysteresis control to keep the current states near their target. Mathematically, this is stated

$$\begin{bmatrix} v_{m,qs} \\ 0 \\ 0 \\ 0 \end{bmatrix} = A_m \begin{bmatrix} i_{m,qs} \\ i_{m,ds} \\ i_{m,qr} \\ i_{m,dr} \end{bmatrix} \qquad (4.49)$$

$$i_{m,qs}^2 + i_{m,ds}^2 = \Theta T_m^{**}.$$

where $\Theta = \frac{4(r_r'^2 + (\omega_s L_r')^2)}{3 P_m \omega_s L_m'^2 r_r'}$.

After solving for $v_{m,qs}$ and linearizing with small displacements, the result when $T_m^{**} \leq T_{m,thres}$ is

$$\Delta v_{m,qs} = \left[K_{ids} - L_s \left(\frac{P_m}{2} \omega_{rm0} + \omega_{s,set} \right) \right] \Delta i_{m,ds} + \left[-L_m \left(\frac{P_m}{2} \omega_{rm0} + \omega_{s,set} \right) \right] \Delta i_{m,dr} \quad (4.50)$$

$$+ \left[-\frac{P_m}{2} (L_s i_{m,ds0} + L_m i_{m,dr0}) \right] \Delta \omega_{rm} + K_T \Delta T_m^{**}$$

where

$$K_{ids} = r_s i_{m,ds0} (\Theta_0 T_{m0}^{**} - i_{m,ds0}^2)^{-1/2} \qquad (4.51)$$

$$K_T = -\frac{r_s}{2} \Theta_0 (\Theta_0 T_{m0}^{**} - i_{m,ds0}^2)^{-1/2}$$

and Θ_0 is Θ such that $\omega_s \equiv \omega_{s,set}$.

When $T_m^{**} > T_{m,thres}$, the equation for $\Delta v_{m,qs}$ accounts for the changing slip frequency:

$$\Delta v_{m,qs} = \left[K_{ids} - L_s(\frac{P_m}{2}\omega_{rm0} + \omega_{s0}) \right] \Delta i_{m,ds} + \left[-L_m(\frac{P_m}{2}\omega_{rm0} + \omega_{s0}) \right] \Delta i_{m,dr} \qquad (4.52)$$

$$+ \left[-\frac{P_m}{2}(L_s i_{m,ds0} + L_m i_{m,dr0}) \right] \Delta\omega_{rm} + K_T \Delta T_m^{**}$$

where

$$K_{ids} = r_s i_{m,ds0}(\frac{\lambda_{r,max}^2}{L_m^2} + \Theta_1 T_{m0}^{**2} - i_{m,ds0}^2)^{-1/2} \qquad (4.53)$$

$$K_T = -r_s \Theta_1 (\frac{\lambda_{r,max}^2}{L_m^2} + \Theta_1 T_{m0}^{**2} - i_{m,ds0}^2)^{-1/2} - \frac{2r_r'}{3P_m \lambda_{r,max}^2}(L_s i_{m,ds0} + L_m i_{m,dr0})$$

and $\Theta_1 = \frac{2L_r'^4}{9L_m'^2 P_m^2 \lambda_{r,max}^2}$.

With $\Delta v_{m,qs}$ as a linear function of the other states, one can substitute it into Eq. 4.43 to attain a closed loop A matrix. For closed loop system analysis, the T_m^{**} state is required so the open loop A matrix in Eq. 4.46 is used. When $T_m^{**} \leq T_{m,thres}$ the entries the 6th column must be removed because the slip frequency is held constant.

The closed loop B matrix allows for the input of torque command $B_{m,cl} = [0\ 0\ 0\ 0\ 0\ 1]'$. Notice that the trim control described in Eq. 4.21 has torque command input $\frac{1}{\tau}T_m^* + \frac{d}{dt}T_m^*$.

The closed loop C matrix gives output for the measured torque

$$C_{m,cl} = \frac{3P_m L_m}{4}[\ i_{m,dr0} \quad -i_{m,qr0} \quad -i_{m,ds0} \quad i_{m,qs0} \quad 0 \quad 0 \ ].$$

Finally, for the sake of validation, results are given in Figure 4.4.2 for the closed loop transfer function, at $T_m^* =100$ Nm, for two different trim control gains. Results are shown for the high fidelity simulation where the three phase current hysteresis control was replaced with combined current hysteresis. The lack of fidelity at higher frequencies was expected because of the use of a continuous control law in place of the ON/OFF switching, for analysis purposes. The results seem to correspond intimately up to and beyond the cutoff frequency, so at the very least a command following design tool has been provided.

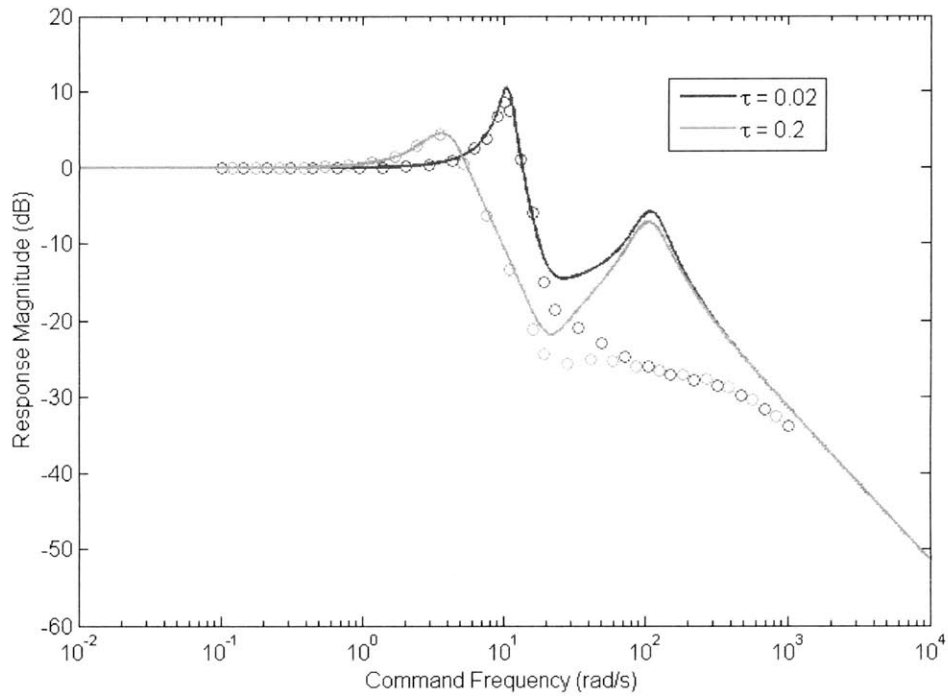Figure 4-12: Bode plot for closed loop motor-propeller system using instantaneous voltage assumption, for $T_m^* = 100$ Nm.

It is too soon to say whether or not the closed loop A matrix derived here is effective for stability prediction with Hurwitz stability critereon, both for the combined phase and three phase control. A more accurate equivalent control law should be sought for this guarantee.

Chapter 5

Simulation Results with AES Model

In this chapter, the capacity of this AES simulator is demonstrated with simulation experiments. Many of the examples shown are straightfoward, for deterministic instances, and are meant for verification of the system model as much as for demonstration of capability. In Section 5.1, power conservation of the IPS during ship startup in shown. In Sections 5.2 and 5.3 simulations for maneuvering in calm seas and random seas, respectively, are carried out.

Section 5.4, explores the some statistical behaviors of the AES using Monte Carlo simulation techniques.

In this chapter, the full scale DDG-type AES model, as depicted in 2-1, is used. The operation scheme for the prime movers is to share the power loads equally; this is an inefficient scheme, but it does not detract from the demonstrative results given. The baseline parameters, mechanical and electrical, are given in Tables 5.1-5.5 for the sake of repeatability. A DDG51 offset was used for the seakeeping model with bilge keel data. 38MW motors are used with parameters defined in Table 2.1. All parameters are adjustable via an input file in the AES simulator.

Displaced Mass m=7e6 $[kg]$	Propeller Diameter D=4.5 $[m]$	Wetted Area A_w=5200 $[m^2]$
Wake Fraction w= 0.1	Thrust Coefficient t=0.1	Pitch Ratio P/D=1.0 [ ]
Propeller Shaft Moment of Inertia I_m=1.33e5 $[kg - m^2]$	Hull Drag Coefficient C_r=3e-3	Fluid Density ρ=1025 $[kg/m^3]$

Table 5.1: Ship surge parameters taken from DDG51 information or [60].

Full Locking Torque	No Load Speed	Turbine Shaft Moment of Inertia
Q_{lock}=123 [kN-m]	$n_{t,max}$=6875 [rpm]	I_t=400 [kg − m²]

Table 5.2: Gas turbine parameters chosen to represent GE's LM2500 [26].

Stator Resistance	Stator Inductance	Mutual Inductance	Pole Number
R_{sg}=2.27e-2 [Ω]	L_{sg}=0.391 [mH]	M_g=18.0 [mH]	P_g=2

Table 5.3: SM parameters selected to provide 4160 V_{l-l} for a rotor speed of 60 Hz.

DC Bus Capacitance	Notching Resistance
C=0.037 [F]	R_p=.05 [Ω]

Table 5.4: Rectifier/inverter parameters. Capacitor sized to store the peak capacity of the power plant for one cycle of the fundamental frequency.

Ship Length	COG to Rudder	Rudder Face Area
L=180.0 [m]	x_p=75.0 [m]	A_r=20.0 [m²]
Rudder Lift Coefficient	Rudder Drag Coefficient	Rudder Swing Rate
C_L=3.31 [ ]	C_D=0.46 [ ]	Δ_r=0.1 [rad/s]

Table 5.5: Maneuvering parameters for DDG-type ship. Rudder parameters informed by [42].

5.1 Conservation of Power across IPS

In this section, power conservation across the IPS is demonstrated in an attempt to validate the system model. The trial presented is a startup from idle to 25 knots, in calm seas. The nonlinear maneuvering model is not used here because its accuracy is compromised below its speed of linearization, approximately 22 knots. Instead, the translational surge model presented in 2.16 is employed.

Power is inventoried at the output of the turbines, the SMs, the inverters, the IMs, and the ship hull. The equations for these powers are given in Table 5.6 using notation from Chapter 2.

Turbine	Generator	Inverter	Motor	Ship
$\sum\limits^{n=4} 2\pi Q_t n_t$	$\sum\limits^{n=4} 3\text{Re}\left\{E_a i_s^*\right\}$	$\sum\limits^{n=2} 3\text{Re}\left\{v_m i_{in}^*\right\}$	$\sum\limits^{n=2} 2\pi Q_m n_p$	$\sum\limits^{n=1} R_{sp} u$

Table 5.6: Power equations.

Figure 5-1 shows the time evolution of the propeller speed and ship speed during startup.
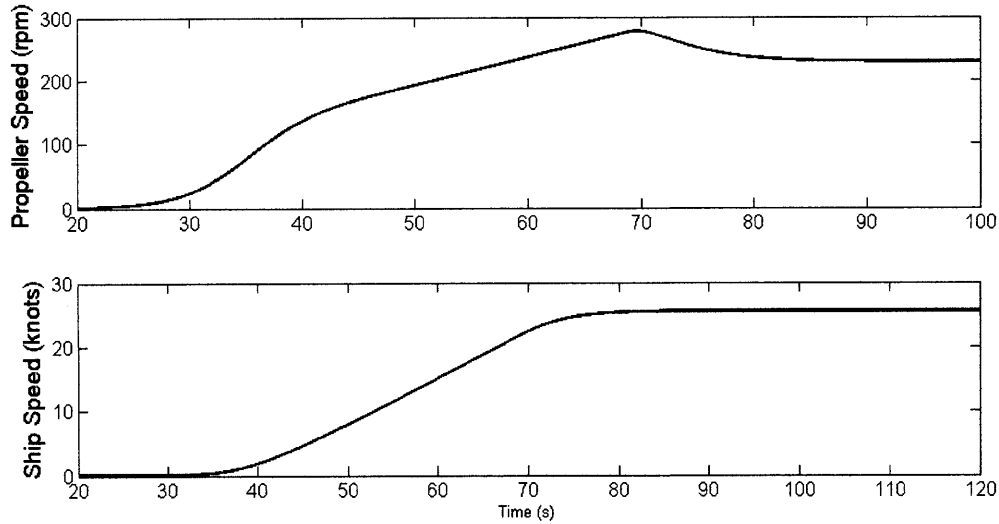
Figure 5-1: Time evolution of propeller speed and ship speed for startup.

The most notable characteristic is that the propeller speed at 25 knots is approximately 225 rpm (and can be shown to be approximately 300 rpm at full-ahead). While the motor selected is rated for rotor speeds up to 300 rpm, these speeds are rather large for conventional marine propellers and could lead to significant cavitation. Propeller diameter is likely to be larger than 4.5 m, as used in this simulation, to achieve full-ahead at lower propeller speeds.

Figure 5-2 shows the time evolution of the inventoried power outputs, during startup. Table 5.7 shows the efficiency of the different componentry at steady conditions. As expected, high efficiency is observed through the IPS. The efficiency of the generator varies between 95 % and 97 % near rated conditions but drops off for lower power generation. The power electronic efficiencies are around 99 %. The IM efficiency seems rather large; traditionally one would expect 3-5 % loss. However, motors of this magnitude, 38 MW, should be even less lossy than conventional propulsion motors - by how much is a question for those researching the development of these high power IMs. η_m in Eq. 2.5 can be altered to reflect other losses such as friction.

The propeller used is 70 % efficient at steady state; this could perhaps be improved with a higher pitch ratio or an innovative propeller design.

Not shown are the turbine thermal efficiencies because the model does not have capability to predict them accurately. From practice, it is expected that the efficiencies would improve
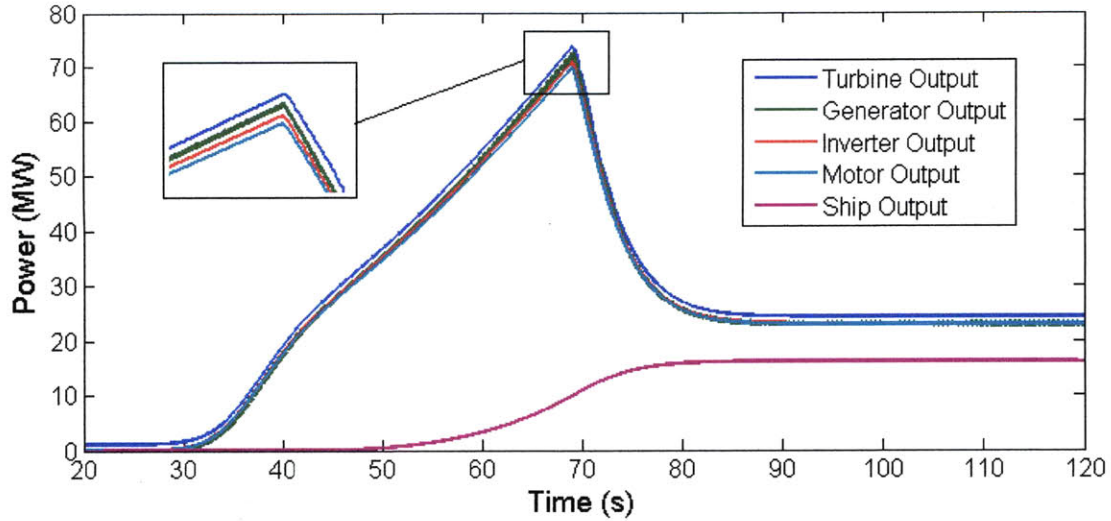
Figure 5-2: Power outputs for different components in AES for startup.

	20 knots	25 knots	30 knots
Synchronous Generator	0.909	0.950	0.971
Power Electronics	0.991	0.992	0.988
Induction Motor	0.993	0.992	0.991
Propeller	0.705	0.703	0.702

Table 5.7: Efficiencies of AES components for different operating conditions.

to as high as 37 % as their rated power (21.5 MW) is approached and would drop off to about 28 % at half the rated power [53].

5.2   IPS Performance during Routine Maneuvering

In this section, maneuvering trials and the corresponding effects on the bus voltage and prime mover speed are examined. The trials are purposefully tutorial to clearly demonstrate the type of studies that can be achieved with the AES simulator. Three fundamental maneuvers will be studied and discussed in this section: acceleration, braking, and heading changes. Other hydrodynamic results for this maneuvering model are given in [51] for those readers interested. The section concludes with a demonstration of second order forces and their effect on maneuvering and fuel consumption.

5.2.1 Acceleration

Here, employing the nonlinear maneuvering model from Section 2.4, is a computational study involving the acceleration of the notional AES from 25 knots to full-ahead using a step command. The resulting propeller and ship speed are shown in 5-3. Notice that the motor operates at speeds beyond its rated speed, 300 rpm; the propellers would need to be resized or given a higher pitch ratio.
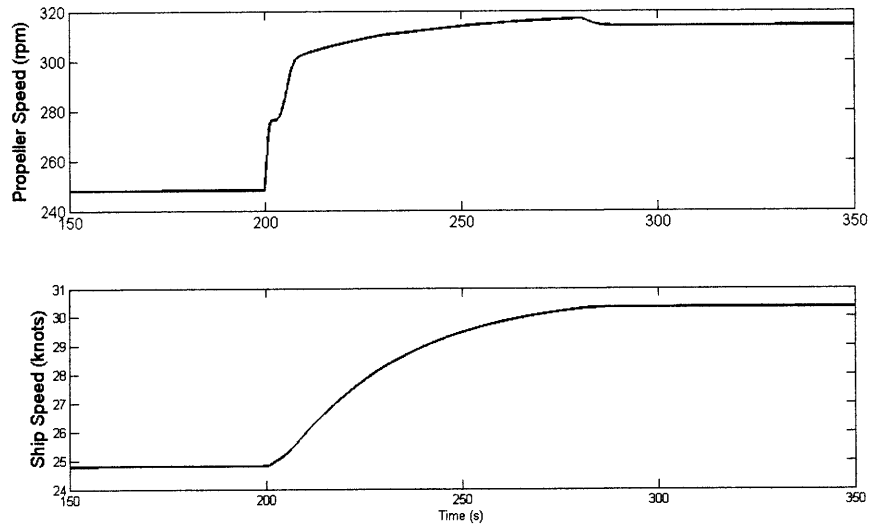
Figure 5-3: Time evolution of propeller speed and ship speed for acceleration from approximately 25 knots to full-ahead.

Figure 5-4 shows the effect of the acceleration on the bus voltage and the prime mover. As the motor demands more power, the prime mover is subject to more emf torque from the generator, it slows down and in effect the bus voltage is reduced. With the baseline controls, the gas turbine sustains an approximately 20 % loss of speed and operates away from its rated speed for approximately 20 seconds. The field control of the bus voltage acts slightly to mitigate voltage drop (without independent control, one would expect the p.u. DC voltage to be identical to the p.u. turbine speed)

Figure 5-5 shows the bus voltage and turbine speed for a different set of field voltage control gains. Still, this is not a satisfactory design. An interesting problem is the joint optimal control of the turbine throttle and field voltage.
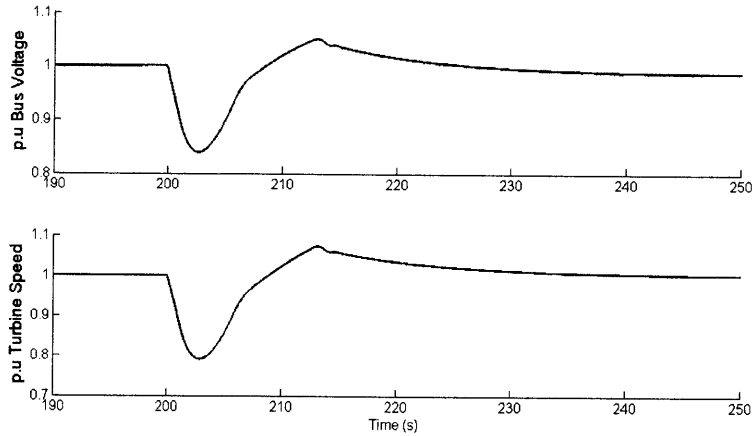
Figure 5-4: Per unit bus voltage and turbine speed during acceleration ($K_{p,v}$=0.0001 and $K_{i,v}$=0.0005).
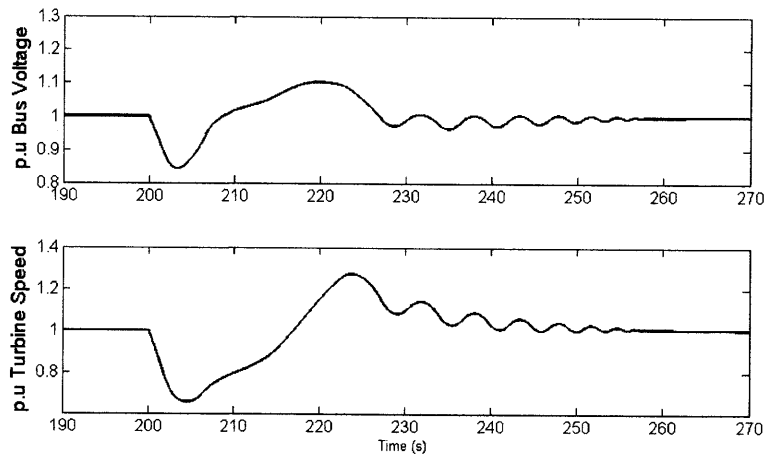
Figure 5-5: Per unit bus voltage and turbine speed during acceleration for higher gains ($K_{p,v}$=0.0003 and $K_{i,v}$=0.001).

5.2.2 AC Braking

AES braking can be accomplished by 1) switching off power to the IM and coasting, 2) locking the motor to increase drag, 3) AC braking and 4) crashback. The AC braking and crashback procedures spell the largest demands for the IPS. In crashback, the IM is brought to zero speed and then reversed; this requires a control protocol more sophisticated than volts per Hertz and is not implemented here. In AC braking, the IM, or more generally the asynchronous machine, is excited with negative slip such that it behaves like a generator. In effect, the ships translational power is converted back to electrical power, much like a water turbine, and the emf torque acts to slow the propeller. The energy that gets forced back into the drive system

must be stored, for instance by capacitors or flywheels, or dissipated. The management and possible harvesting of this braking energy is an important problem in AES design.

To conduct this type of simulation, small alterations were required for the propeller and IM models. First, a propeller model was required that gave thrust and torque coefficients at large advance coefficients where torque and thrust reverse directions. Rubis's empirical four-quadrant model provides this [60]. Also, an offset discontinuity was inserted to prevent the singularity that occurs at zero slip with the equivalent circuit IM model.

The propeller speed and ship speed are shown in Figure 5-6 for the AC braking procedure. Water brakes are likely to be used at lower speeds to bring the ship to a complete halt.
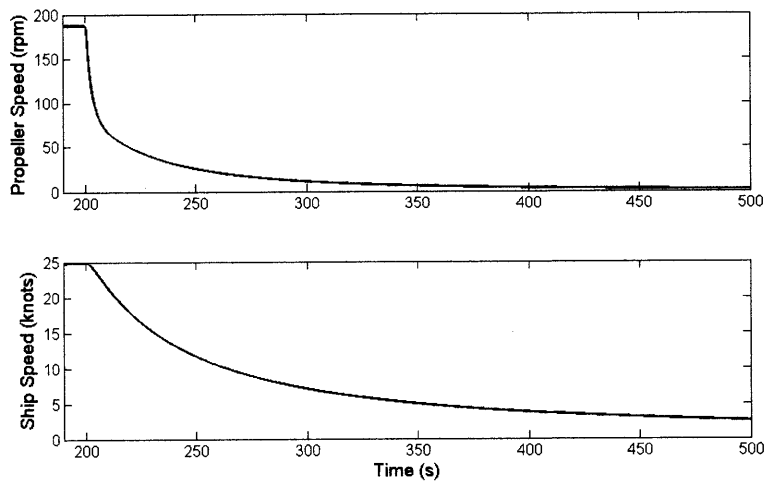
Figure 5-6: Propeller and ship speed during AC braking.

The following is a description of the power transients in the IPS during the AC braking procedure. First, the induction machines generate electrical power and it flows back into the IPS and congregates in the capacitors. Immediately after braking, the IM demands no further energy, so the energy is stuck in the IPS and must be dissipated or stored. In the ideal case, switching is used to open up exigency loads to expire the excess energy and buffer the prime movers from the power surge, and with no major loads to service, the prime movers reduce their throttle to idling. Figure 5-7 shows an example of the bus voltage and turbine speed perturbations during AC braking in ideal power management. These are acceptably controlled responses but bear in mind that the "ideal" power management for the AES requires the containment or dissipation of most of the ship's kinetic energy, about 10 MJ in each power

plant.
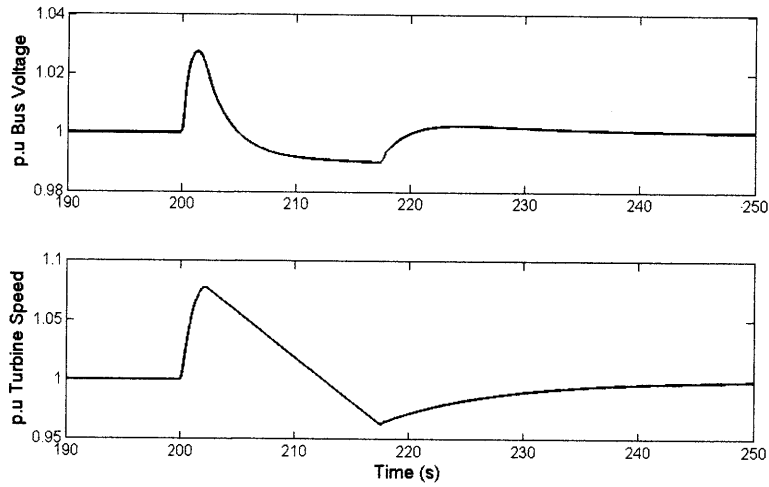
Figure 5-7: Per unit bus voltage and turbine speed during AC braking with ideal power management.

Figure 5-8: Per unit bus voltage and turbine speed during AC braking without planned dissipation.

Figure 5-8 shows an example of the bus voltage and turbine speed perturbations during AC braking when power goes mostly unbuffered from the prime movers. The excess power causes the turbine to reach harmful speeds despite the control adjusting the throttle to zero.
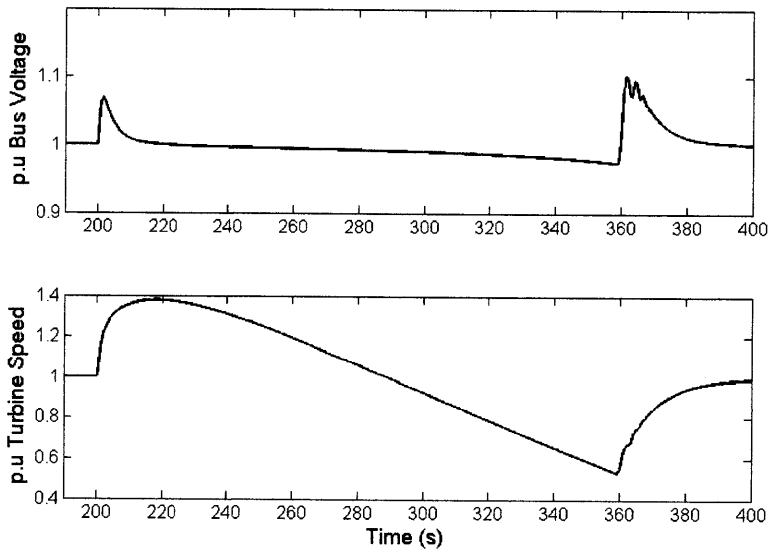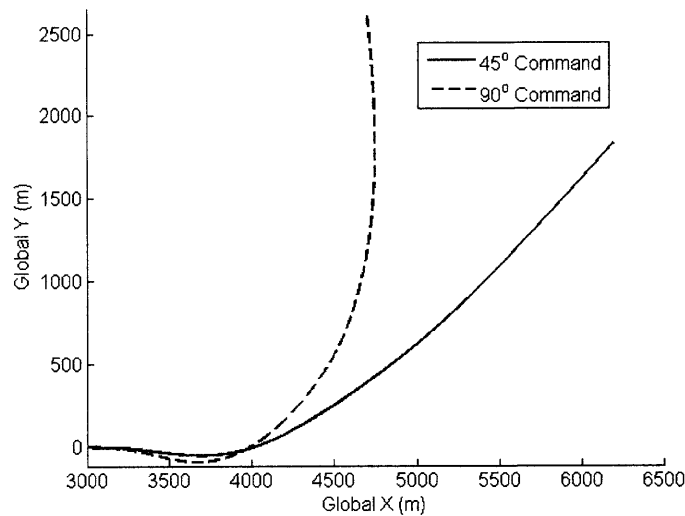
Figure 5-9: Global positions for heading change trials with 45° and 90° commands.

5.2.3 Heading Changes

Turning at high speeds can have a profound effects on the IPS that must be managed. First, while making a turn, the ship becomes less streamlined in its direction of travel and more power is required to keep it up to speed. Secondly, the propeller operation is altered due to changes in the axial and traverse inflow. Both at the onset and egress of the turn, these cause load fluctuations that are of concern to IPS operation.

Figure 5-9 shows the global position of a ship for a 45° and 90° heading change. The trajectories match well with theory.

Figure 5-10 demonstrates the two key effects relevant to propulsion management that occur when making a turn. The first subfigure shows the increase in required power to maintain speed. For the 45° turn there is approximately a 6 % increase in required power and for the 90° turn there is approximately a 15 % increase in required power. In the second subfigure, the loss of propeller efficiency due to altered inflow velocity is demonstrated.

5.2.4 Second Order Forces

Figure 5-11 shows the maneuvering states for simulations in sea state 3 (SS3) and state state 6 (SS6) to illustrate the effects of the added resistance and drift forces. These effects are essential in ship design, for example, in assessing fuel consumption or designing global

103
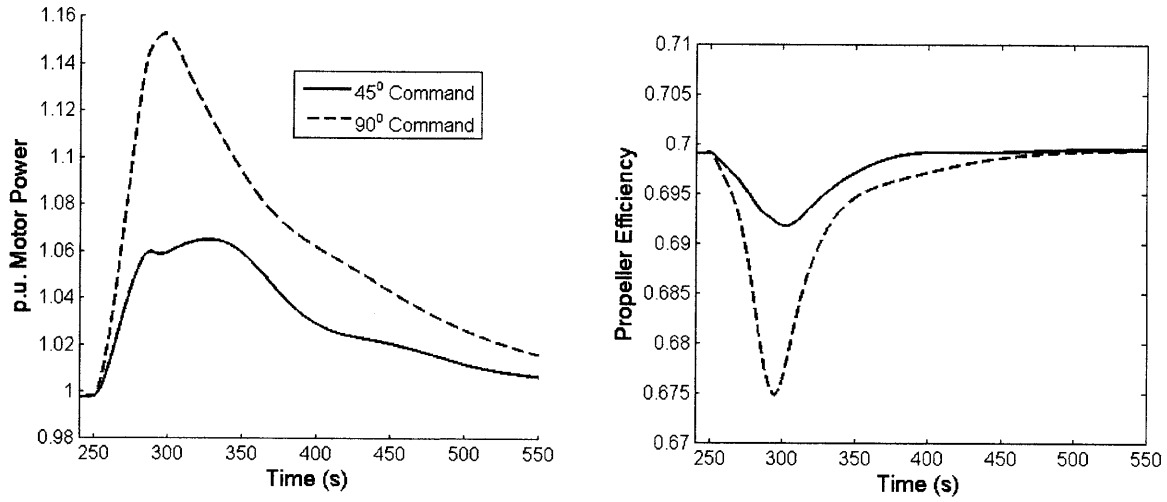
Figure 5-10: Fluctuation in a) motor power draw, and b) propeller efficiency, during heading change.

positioning management.
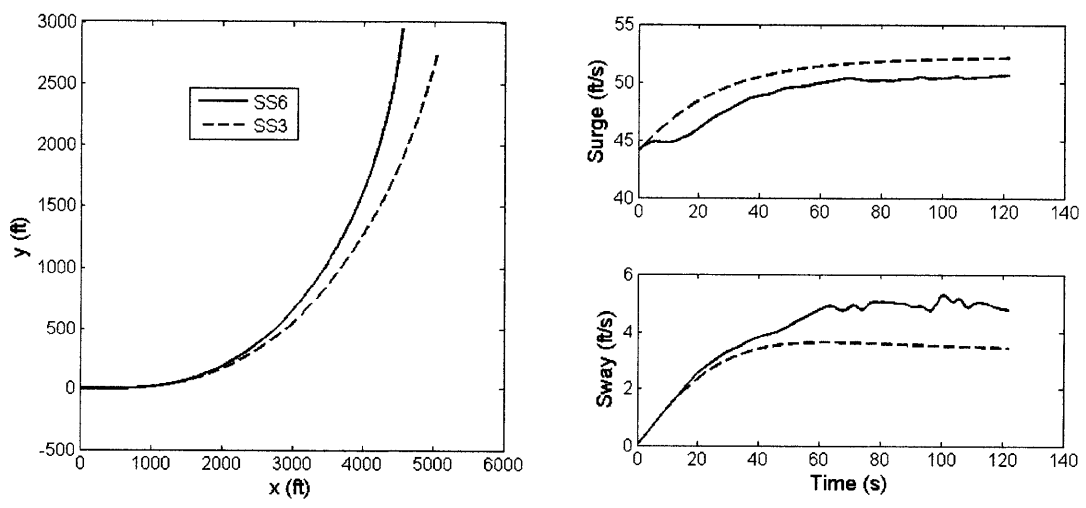
Figure 5-11: Added resistance results for quarter turn.

Figure 5-12 shows the fuel power consumption of a single prime mover for an AES traveling in discrete seas of varying frequency, heading, and amplitude (from 1 to 5 feet). The fuel power consumption was computed from turbine output power with a generic gas turbine efficiency curve [53]; the efficiency of each turbine is low due to the lack of an intelligent scheme for prime mover operation.
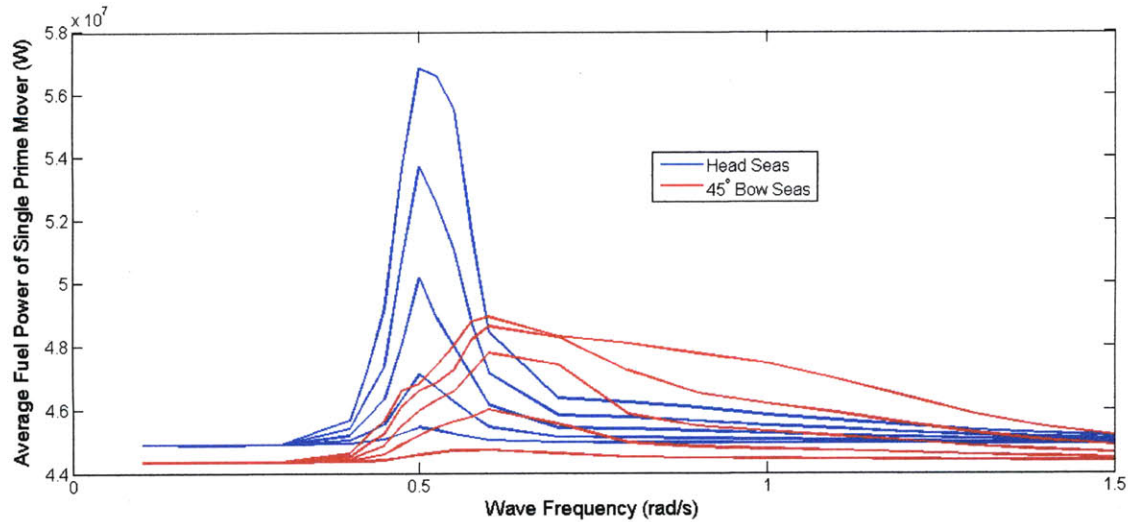
Figure 5-12: Fuel power consumption for travel in discrete seas of amplitude varying from 1 to 5 ft, for bow and head sea travel.

5.3 IPS Performance in Random Sea Environments

This section examines the coupling between seakeeping and the IPS. While this can occur due to lateral movement of and wave interaction with the propeller, focus here is on surface effects, like cavitation and out-of-water conditions. The models for these losses are discussed in Section 2.3. A static hub distance h_0 of 6.0 meters is selected for these trials, informed by [42].

Surface effects among other things result in rapid losses in propeller loading followed by rapid load recovery at reemergence. For traditional propulsion systems, this poses less of a problem due to the large inertia of the drive system. For the electrical drive, the unloading would theoretically result in rapid acceleration of the rotor and potentially large power transients. This is imagined as one of the most challenging problems when conceptualizing the distribution and IM controls.

As seakeeping involves a random wave process, the analysis should factor in uncertainty quantification to understand the average behaviors and the bounded behaviors of surface effects. This will be addressed in Section 5.4. In the present section, results of single instance simulations are provided and discussed to clearly show the utilities of this AES simulator. The first subsection examines travel in head seas. The second subsection examines the execution of 360° turn.

5.3.1 Seakeeping in Head Seas

This simulation in head seas is for a DDG51 type hull shape with a target ship speed of 25 knots, in SS6. Results are shown for 80 seconds, or approximately 6 fundamental wave periods (defined as the period of the peak frequency in the spectrum). Figure 5-13 shows the wave height at the stern and the distance from the propeller hub to the mean water line. Figure 5-14 shows the h/R plot and the corresponding thrust and torque losses. Figure 5-15 shows the propeller speed and the corresponding per unit power transients at the IM, where the normalizing IM power is that which gives steady 25 knots operation with a fully submerged propeller.

In these results very frequent cavitation and occasional emergence are observed. In the cases of emergence, only a small fraction of the propeller comes out of the water. Note: in higher seas states, it is possible to see the majority of the propeller come out of the water resulting nearly in a no load condition on the IM that can be especially harmful; these higher sea states are not simulated here because linear seakeeping approximations in high sea states tends to lose accuracy.

With the specific parameters chosen, a 50 rpm propeller speed perturbation and a 25 % IM power pertubration are observed. If operating at full-ahead, these transients would result in the exceeding of IM limitations.

5.3.2 Seakeeping during 360 Degree Maneuver

This section presents results for the simulation of an AES completing a 360° turn in SS6, with a ship speed command of 25 knots, beginning in head seas. The turn is achieved by sending a ramp command to the heading control; the slope of the ramp command is set so that the rudder reaches its maximum angle before stall. Figure 5-16 shows the birds eye view of the ship executing the turn; time markers are given so that heading information can be deduced when viewing the time evolution plots. The radius of the turn is approximately three ship lengths. This is about what one would expect from a DDG type ship at 25 knots [42].

Figure 5-17 shows the h/R evolution during the maneuver with domains indicating cavitation, propeller out of water, and hub out of water conditions. This shows that head seas tend to be the most threatening to load perturbation. In following seas at 25 knots, the ship
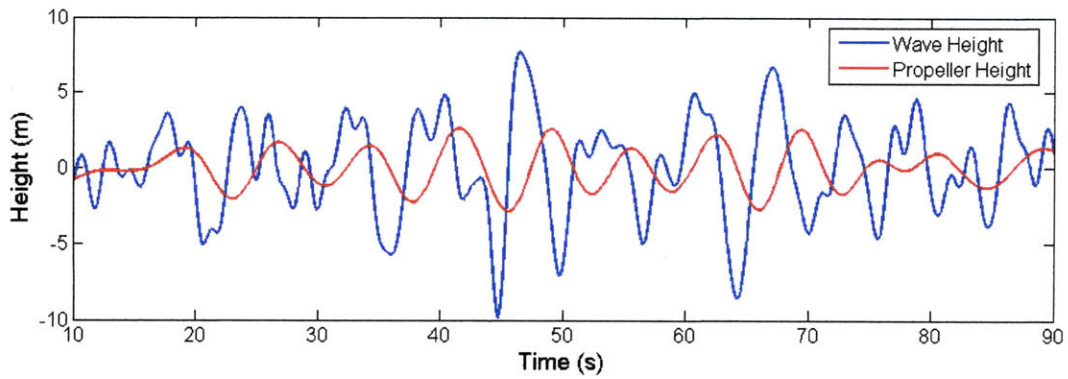
Figure 5-13: The wave height and propeller height at the stern during seakeeping in head seas.
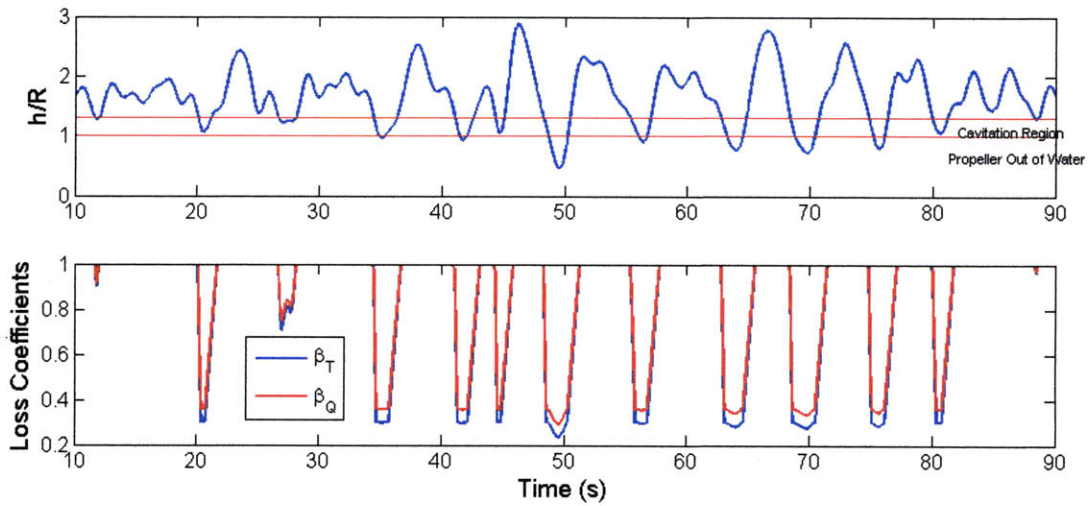
Figure 5-14: The h/R plot (top) and the propeller losses (bottom) during seakeeping in head seas.
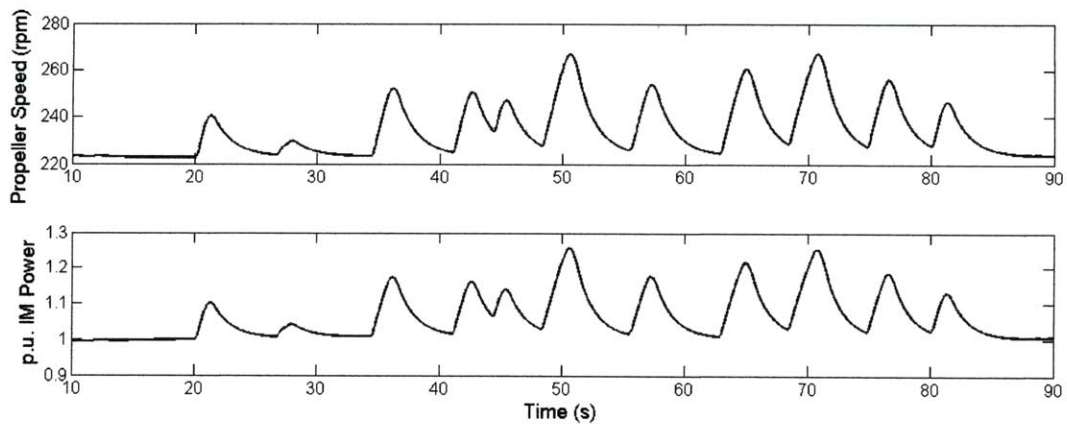
Figure 5-15: The propeller speed (top) and the IM power transients (bottom) during seakeeping in head seas.
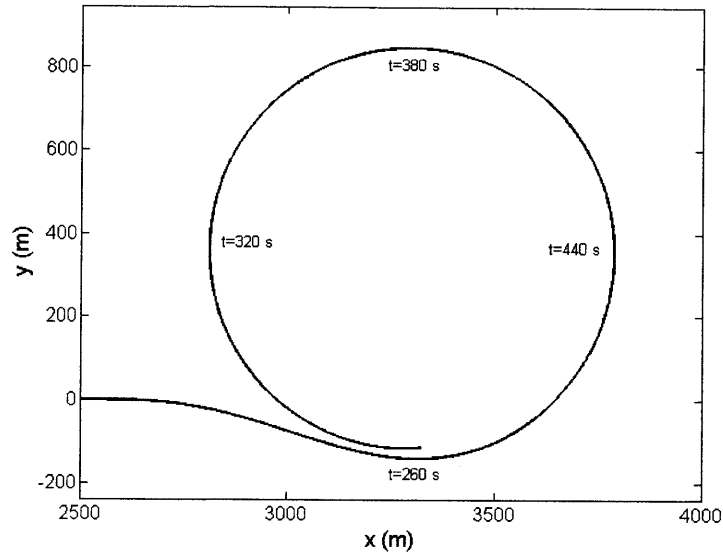
Figure 5-16: Global position of ship during full turn.

is excited very little in heave and pitch.

Figure 5-18 shows the propeller and ship speeds during the maneuver. To maintain 25 knots during the low radius turn, approximately 255 rpm are required with transients leading to speeds upwards of 300 rpm. This exceeds the rated speed for the motor is is likely to lead to damage or inefficiency. Note also that in addition to the haphazard seakeeping motions, the thrust transients leads to rapid 2-3 % changes in surge speed, which may or may not be perceptible onboard.

Figure 5-19 shows the per unit IM power during the maneuver. To keep up to 25 knots during the turn, about 160 % of the unit motor power is required with transients exceeding 200 % of the unit power requirement.

5.4 Stochastic Simulation with AES Simulator

The examples given in the previous sections serve as system model validation, but they do not get at the heart of the AES simulator's utilities. The AES simulator has been run in under real time on the author's Dell M1530 laptop, programmed in MATLAB and Simulink, and run with Simulink's Rapid Accelerator mode [50]. The speed of the simulator makes it a likely candidate for studies requiring iterations. Here, as an example, high effort Monte Carlo

108
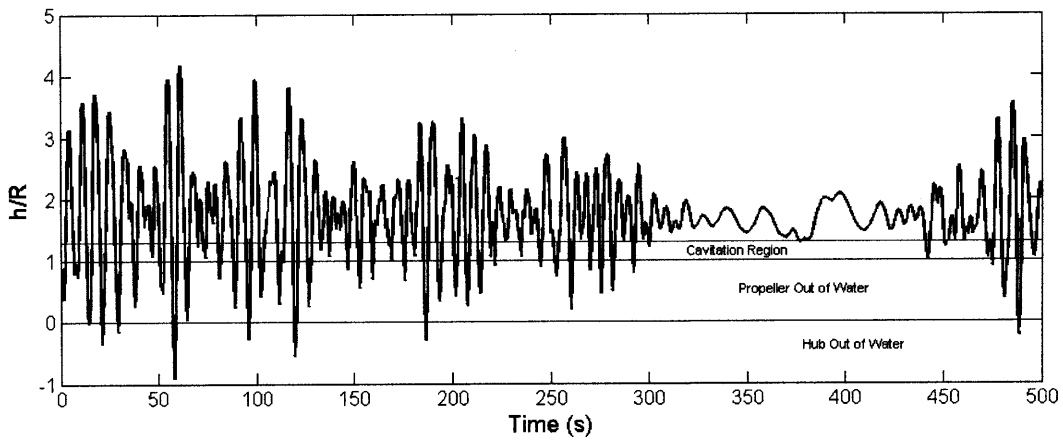
Figure 5-17: h/R plot during 360° turn.
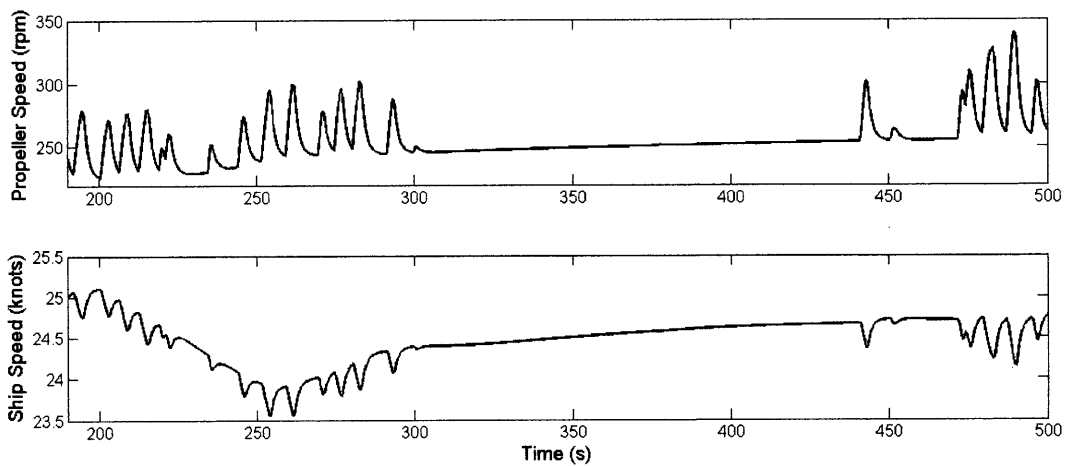
Figure 5-18: Propeller speed (top) and ship speed (bottom) during 360° turn.
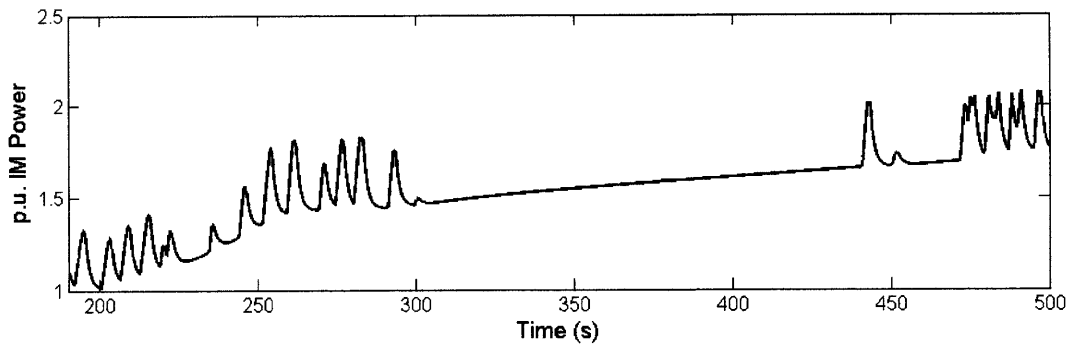
Figure 5-19: p.u. IM power during 360° turn.

109

methods are used to quantify uncertainty [44] using the random wave sampling procedure described in Section 2.5.4.

Addressing random ocean environments is a topic as important as any within the naval engineering discipline; understanding the characteristics of random seas and quantifying their effects is a necessary step in the design of any naval system. In this subsection, the focus is on quantifying uncertainty in AES propulsion, specifically the behavior, likelihood, and severity of surface effects on the propeller, IM, and IPS.

The first subsection will explore methods for assessing uncertainty during frequent surface effects and the second section will explore methods for assessing infrequent surface effects.

5.4.1   Statistics of High Frequency Surface Effects

Uncertainty quantification methods like Monte Carlo simulation become convenient for propagating uncertainty across nonlinear mappings, as between ship motions and IPS states, and evaluating average and bounded dynamics. To illustrate the uncertainty analysis here, IM energy and power are used, though any other IPS state/variable could be used.

The following studies were conducted with a target ship speed of 25 knots in head seas, SS6. To elicit high frequency surface effects, a propeller diameter of 4.8 meters and a poor static length, $h_0 = 4.0$ m, were used. 100 Monte Carlo trials were used to achieve acceptable convergence, with each trial lasting 80 seconds.
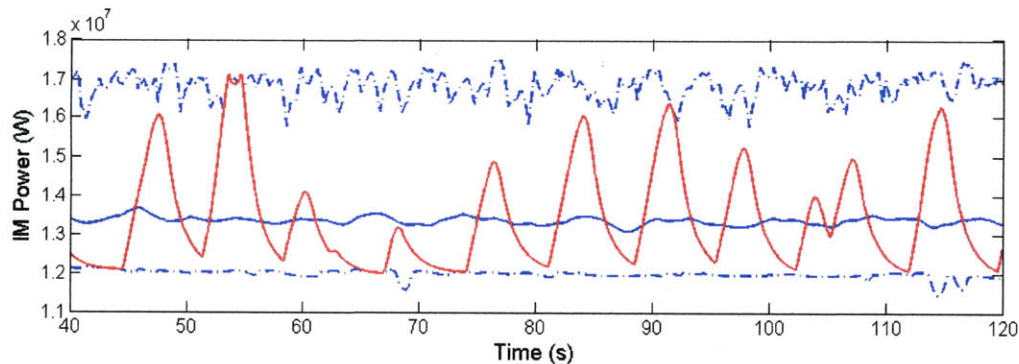
Figure 5-20: A single realization of IM power in random seas (red), the averaged behavior over 100 MC trials (blue), and the minimum/maximum bounds over 100 MC trials (blue-dashed).

Figure 5-20 shows one realization of the IM power evolution in random seas. The plot

110
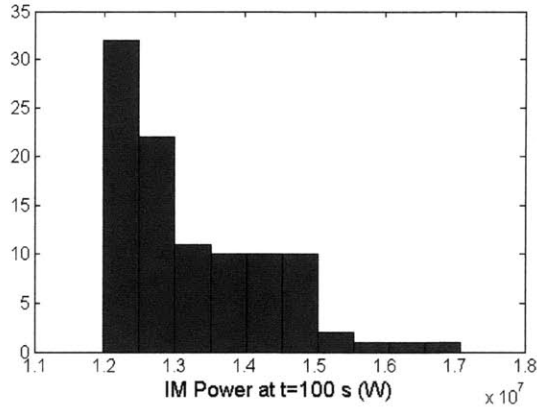
Figure 5-21: Histogram of IM power at t=100 s.
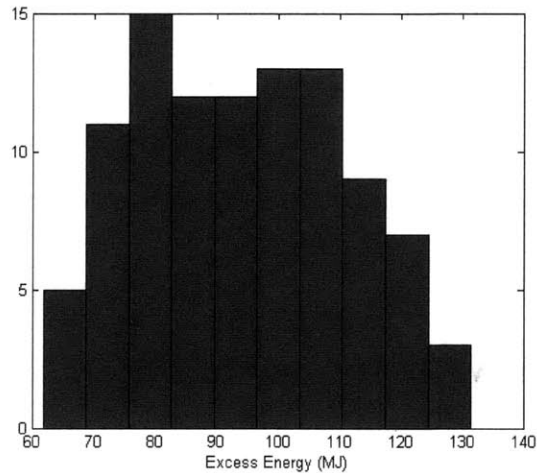
Figure 5-22: Histogram of excess power due to propeller emergence for 80 seconds travel in head seas, SS6.

also includes the average value and the maximum and minimum values observed over the 100 simulations. Standard deviations were not used to define the bounds as the instantaneous probability distribution function (pdf) for any given time is heavily skewed toward the minimum; this is illustrated in Figure 5-21, a histogram of IM power values at t=100 s.

Figure 5-22 shows a histogram of the excess energy drawn by one of the IMs due to propeller emergence, over the entire 80 second simulation. As expected by the central limit theorem, the pdf looks to have a normal distribution. The average excess energy is approximately 94.1 ± 33.3 MJ, or the average excess power drawn by the IM is 1.18 MW.

Another approach is to look at the spectral content of the power transients. Welch's method was used to produce the periodogram in Figure 5-23 [72]. Again, maximas and minimas over
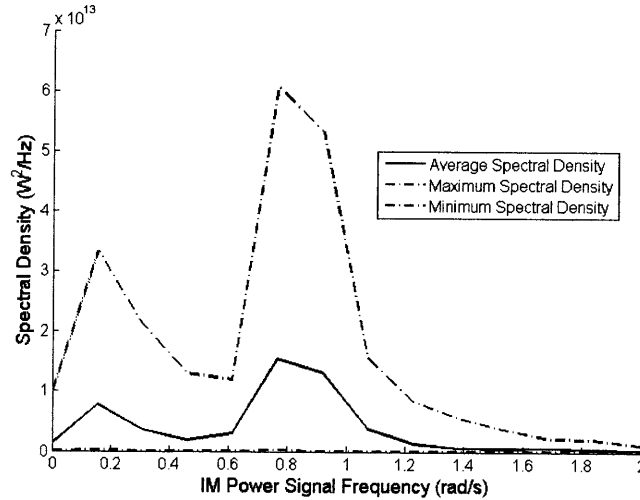
Figure 5-23: Periodogram illustrating the spectral content of the IM power transients during 25 knots travel in head seas, SS6.

the 100 trails were used to illustrate the bounded behavior. This periodiogram can be used to predict statistical moments and furthermore occurrence rates. There will be more on this in the next subsection.

5.4.2 Statistics of Low Frequency Surface Effects

In the case of high frequency surface effects, the analysis focused on wave forms and their statistical behavior. In the case of low frequency surface effects, the analysis will focus on rate of occurrence and severity of an individual occurrence. First this section will compare analytical and numerical predictions for surface effect occurrence rate. Then, it will attempt to quantify the variation of a surface effect instance.

The following studies were conducted with a target ship speed of 25 knots in head seas, SS6. To elicit lower frequency surface effects, a propeller diameter of 4.8 meters and a larger static distance, $h_0 = 6.0$ m, were used. At least 100 Monte Carlo trials were used to achieve acceptable convergence.

One can predict the rate of occurrence of surface effects a priori with frequency domain methods. The response spectrum $S_y(\omega)$ of an input-output event defined by transfer function

$H(\omega)$, with input spectrum $S(\omega)$, can be found:

$$S_y(\omega) = |H(\omega)|^2 S(\omega). \tag{5.1}$$

In the study of surface effects in random seas, the input is the random wave spectrum and the output of concern is the distance from the propeller hub to the free surface, defined by the transfer function

$$\hat{H}_p(\omega) = e^{ikx_s} - \hat{H}_3(\omega) + x_s\hat{H}_5(\omega). \tag{5.2}$$

Given the response spectrum, the frequency of exceeding a distance Z, denoted $\eta(Z)$, can be computed using the spectral moments of the response:

$$
\begin{aligned}
\eta(Z) &= \frac{1}{2\pi}\sqrt{\frac{M_2}{M_0}}e^{-Z^2/(2M_0)} \\
M_0 &= \int_0^\infty S^+(\omega)d\omega \\
M_2 &= \int_0^\infty S^+(\omega)\omega^2 d\omega.
\end{aligned}
\tag{5.3}
$$

Recall for surface effects study, the Z of interest is the one where h/R becomes less than 1.3, when cavitation sets in. For the parameters given at the beginning of this subsection, Z can be calculated as 3.88 m or 12.73 ft. Given this value and the response spectrum, the prediction of surface effect occurrence frequency is 0.044 times per second; average arrival time of 22.64 seconds. The distribution of arrival times is expected to have an approximately exponential distribution with a rate parameter $\lambda = 0.044$ [13]. Statistical values for this distribution are given in Table 5.8.

To compare these analytical results with experiment, MC simulations were run. These simulations were structured to terminate when a surface event occurred (when $\beta_T \neq 1$), and return the time of occurrence; the arrival time. Figure 5-24 shows the arrival rate histogram for 189 MC trials with the analytically predicted exponential distribution pdf (scaled to fit the histogram at the left side of its support). Table 5.8 gives the analytically and numerically

113
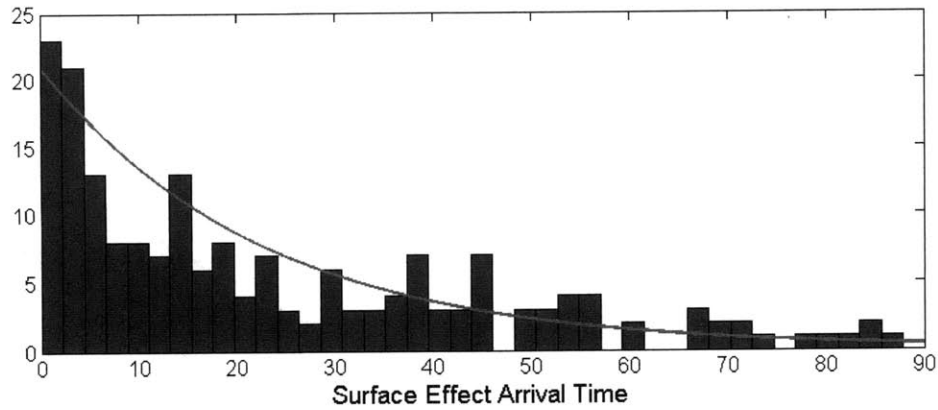
Figure 5-24: Histogram of surface effect arrival times with analytically predicted exponential distribution for 25 knots travel in head seas, SS6.

Mean	Standard Deviation	Skewness	Kurtosis	Median	Mode
22.64	22.64	2	9	15.69	0
23.67	22.11	1.00	3.13	15.46	0.0217

Table 5.8: Analytically and numerically predicted statistical parameters for arrival time of surface effecs for 25 knots travel in head seas, SS6.

predicted statistical parameters. The error in skewness and kurtosis is attributable to the neglect of 'long-tail events' in order to accelerate the computational analysis; all simulations were terminated at 90 seconds if no arrival had occurred, theoretically eliminating 2 % of the events.
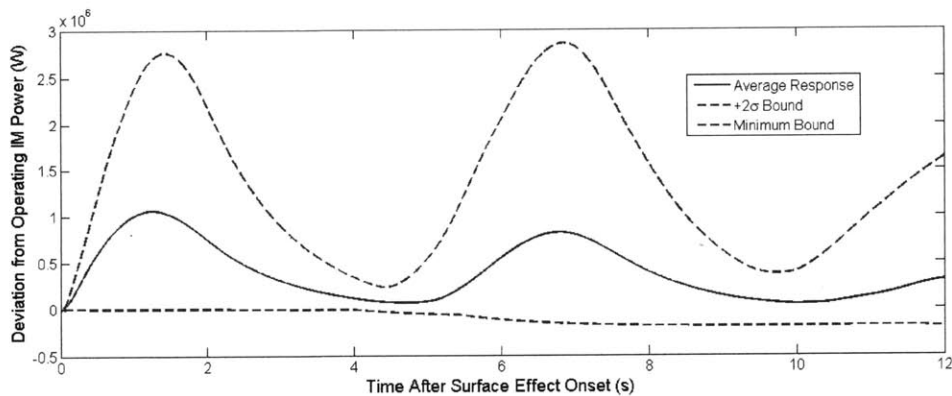
Figure 5-25: Statistical behavior of IM power transients after onset of surface effect, for 25 knots travel in head seas, SS6.

Finally, Figure 5-25 shows the average and bounded behavior of IM power transients during a surface effect event, for 100 MC trials, attained by storing data for 12 seconds after the

onset of the first surface effect. The two standard deviation bound was found to be the most descriptive for the upper bound and the minimum the most descriptive for the lower bound. An interesting trend presents itself: surface effects often occur very close together. This should not be explained by the well-known memorylessness of the Poisson process because the surface effect events are *not* independent of each other [13]. On the contrary, this plot emphasizes the correlative nature of surface effect events, a correlation that should not be ignored in the design of feedback control systems for the IPS.

Chapter 6

Conclusions and Future Research

This Masters thesis presents and validates 1) a full-scale, end-to-end model of the notional AES and 2) an analytical toolbox for the performance and stability assessment of a scale IPS, the Purdue MVDC Testbed, similar to the MVDC distribution that is a candidate for the AES propulsion architecture.

Chapter 2 gives a full mathematical description of the representative, albeit low order, models for prime movers, controlled IPS machinery, IPS converters, and propellers. Chapter 3 recommends the use of higher order models for more complex studies, including a revision of the 23 state, LQG-LTR controlled jet turbine presented in [36]. Together, these chapters offer a full review of modeling techniques for electrical ship propulsion.

Sections 2.4 and 2.5 introduce a 6DOF time domain maneuvering/seakeeping subprogram with the inclusion of second order wave forces. The seakeeping model allows for the input of an arbitrary hull shape. This capability is important for AES simulation because it provides for prediction of load perturbations, and the resulting (megawatt) power transients, due to surface and inflow effects. Combating random power transients of this magnitude is one of the largest challenges for IPS design. Results are given for ship trials in calm and random seas, including Monte Carlo simulations to assess the statistical nature of the power transients.

Chapter 4 gives a full tutorial for the IPS performance and stability assessment program. First, time averaged nonlinear equations are presented for all of the IPS subcomponents and procedures are described for locating operating equilibriums. Small displacement theory is used to derive linear models about the equilibrium. The analytical expression for these linear

state space matrices are given. These state space models are validated against simulation of the high fidelity Purdue MVDC Testbed model [49]. Then, for the generator side, closed loop state space matrices are easily derived for the PI feedback control employed.

The ultimate challenge for the stability analysis of the IPS is the hysteretic current control employed for induction motor torque control. Describing function methods, with their first order approximation, have proved inaccurate for this system. A method is introduced which attempts to analyze hysteretic feedback control by replacing the discontinuous actuation with an equivalent continuous control law. The equivalent control law suggested actuates the stator voltage magnitude continuously to achieve the current magnitude command by following the inverse steady state equations of the IM. Results are given to show correspondence with high fidelity simulation at frequencies below the command following cutoff frequency.

6.1   Recommended Research and Studies

This thesis makes several contributions in the area of computational AES design and analysis, but leaves some open problems requiring immediate attention. Information has been disseminated as clearly as possible in the preceding thesis, and code has been provided in a commented form, so as to allow for efficient inheritance of the work.

The largest weakness of the fully-coupled AES simulator is the lack of a more sophisticated propeller model to be coupled with the maneuvering/seakeeping model. As discussed, Open-Prop is on the cusp of publishing a program that would allow for the computation of thrust and torque curves for arbitrary propeller geometry and inflow. This would allow for a richer propeller design space and more accurate simulation. Only then would the hydrodynamics of the ship be coupled to the IPS in a wholly reliable manner.

From a system level standpoint, two important additions should be made to the AES model to enhance its capability. First, it is critical that other ship loads, converters, and distribution branches are incorporated off of the main power bus to assess how propulsion load changes effect other subsystems, see [9]. Secondly, a more intelligent operating schedule should be devised for the four prime mover power source to optimize efficiency over the ship's entire operating range.

Concerning the IPS stability tool, work is far from over. While this thesis provides reliable open loop prediction tools, instability of concern is likely a product of the control loop. This thesis gives tools for closed loop performance prediction, but these tools have not been verified to be capable of answering the question "is the IPS stable under conditions X at operating point Y?"

Appendix A: Strip Theory Coefficients

The strip theory used in this thesis is taken verbatim from [62]. The superscript 0 refers to the zero speed terms; the integration of the sectional coefficients over the hull. The superscript A refers to the aftmost section of the ship. The inclusion of these aftmost terms have been validated against experimental results, even for transom sterns where the sectional gradient of the ship should in theory hurt the performance of the strip theory approximation. x_A is the distance from the origin to the aftmost section. ξ is a dummy parameter for integration over the ships length.

The derived added mass coefficients are

$$A_{22} = \int a_{22} d\xi - \frac{U}{\omega^2} b_{22}^A \tag{1}$$

$$A_{24} = A_{42} = \int a_{24} d\xi - \frac{U}{\omega^2} b_{24}^A \tag{2}$$

$$A_{26} = \int \xi a_{22} d\xi + \frac{U}{\omega^2} B_{22}^0 - \frac{U}{\omega^2} x_A b_{22}^A + \frac{U^2}{\omega^2} a_{22}^A \tag{3}$$

$$A_{33} = \int a_{33} d\xi - \frac{U}{\omega^2} b_{33}^A \tag{4}$$

$$A_{35} = -\int \xi a_{33} d\xi - \frac{U^2}{\omega^2} B_{33}^0 + \frac{U}{\omega^2} x_A b_{33}^A - \frac{U^2}{\omega^2} a_{33}^A \tag{5}$$

$$A_{44} = \int a_{44} d\xi \frac{U}{\omega^2} b_{44}^A \tag{6}$$

$$A_{46} = \int \xi a_{24} d\xi + \frac{U}{\omega^2} B_{24}^0 - \frac{U}{\omega^2} x_A b_{24}^A + \frac{U^2}{\omega^2} a_{24}^A \tag{7}$$

$$A_{53} = -\int \xi a_{33} d\xi + \frac{U}{\omega^2} B_{33}^0 + \frac{U}{\omega^2} x_A b_{33}^A \tag{8}$$

$$A_{55} = \int \xi^2 a_{33} d\xi + \frac{U^2}{\omega^2} A_{33}^0 - \frac{U}{\omega^2} x_A^2 b_{33}^A + \frac{U^2}{\omega^2} x_A a_{33}^A \tag{9}$$

$$A_{62} = \int \xi a_{22} d\xi - \frac{U}{\omega^2} B_{22}^0 - \frac{U}{\omega^2} x_A b_2 2^A \tag{10}$$

$$A_{64} = \int \xi a_{24} d\xi - \frac{U}{\omega^2} B_{24}^0 - \frac{U}{\omega^2} x_A b_{24}^A \tag{11}$$

$$A_{66} = \int \xi^2 a_{22} d\xi + \frac{U^2}{\omega^2} A_{22}^0 - \frac{U}{\omega^2} x_A^2 b_{22}^A + \frac{U^2}{\omega^2} x_A a_{22}^A . \tag{12}$$

The added damping coefficients are

$$B_{22} = \int b_{22} d\xi + U a_{22}^A \tag{13}$$

$$B_{24} = B_{42} = \int b_{24} d\xi + U a_{24}^A \tag{14}$$

$$B_{26} = \int \xi b_{22} d\xi - U A_{22}^0 + U x_A a_{22}^A + \frac{U^2}{\omega^2} b_{22}^A \tag{15}$$

$$B_{33} = \int b_{33} d\xi + U a_{33}^A \tag{16}$$

$$B_{35} = -\int \xi b_{33} d\xi + U A_{53}^0 - U x_A a_{33}^A - \frac{U^2}{\omega^2} b_{33}^A \tag{17}$$

$$B_{44} = \int b_{44} d\xi + U a_{44}^A + B_{44}^* \tag{18}$$

$$B_{46} = \int \xi b_{24} d\xi - U A_{24}^0 + U x_A a_{24}^A + \frac{U^2}{\omega^2} b_{24}^A \tag{19}$$

$$B_{53} = -\int \xi b_{33} d\xi - U A_{33}^0 - U x_A a_{33}^A \tag{20}$$

$$B_{55} = \int \xi^2 b_{33} d\xi + \frac{U^2}{\omega^2} B_{33}^0 + U x_A^2 a_{33}^A + \frac{U^2}{\omega^2} x_A b_{33}^A \tag{21}$$

$$B_{62} = \int \xi b_{22} d\xi + U A_{22}^0 + U x_A a_{22}^A \tag{22}$$

$$B_{64} = \int \xi b_{24} d\xi + U A_{24}^0 + U x_A a_{24}^A \tag{23}$$

$$B_{66} = \int \xi^2 b_{22} d\xi + \frac{U^2}{\omega^2} B_{22}^0 + U x_A^2 a_{22}^A + \frac{U^2}{\omega^2} x_A b_{22}^A \tag{24}$$

where B_{44}^* is the nonlinear roll damping term.

The complex wave excitement magnitudes are

$$F_2 = \rho \alpha \int (f_2 + h_2) d\xi + \rho \alpha \frac{U}{i\omega} h_2^A \tag{25}$$

$$F_3 = \rho \alpha \int (f_3 + h_3) d\xi + \rho \alpha \frac{U}{i\omega} h_3^A \tag{26}$$

$$F_4 = \alpha \rho \int (f_4 + h_4) d\xi + \rho \alpha \frac{U}{i\omega} h_4^A \tag{27}$$

$$\tag{28}$$

$$F_5 = -\rho\alpha \int \left[\xi(f_3 + h_3) + \frac{U}{i\omega}h_3 \right] d\xi - \rho\alpha\frac{U}{i\omega}x_A h_3^A \tag{29}$$

$$F_6 = \rho\alpha \int \left[\xi(f_2 + h_2) + \frac{U}{i\omega}h_2 \right] d\xi + \rho\alpha\frac{U}{i\omega}x_A h_2^A. \tag{30}$$

where ρ is density and α is wave amplitude.

Finally, the restoring forces are

$$C_{33} = \rho g \int b\, d\xi \tag{31}$$

$$C_{35} = C_{53} = -\rho g \int \xi b\, d\xi \tag{32}$$

$$C_{44} = \rho g V (GM) \tag{33}$$

$$C_{55} = \rho g \int \xi^2 b\, d\xi \tag{34}$$

where g is the gravitational constant, V is the displaced volume of the ship, and GM is the metacentric height.

Appendix B: LQG-LTR Gas Turbine Compensator State Space

<u>A Matrix</u>

[-1.36317e5   -7.56291e4   2.24193e2   -5.77313e4   1.41082e4   -1.11746e2

2.93269e4   2.18779e4   1.19697e3   -5.11421e2   -6.26967e2   -1.15643e2

-1.07955e3   -4.19324e2   -3.78154e2   -1.15555e2   1.21817e2

$\underbrace{\qquad\qquad\qquad\qquad\qquad\qquad\qquad\qquad\qquad\qquad\qquad}$

Row 1

-7.56263e4   -1.64457e5   -4.90732e3   -4.40861e4   9.35596e3   -5.52698e2

1.86929e4   1.43170e4   1.30483e3   -8.43400e2   -4.81956e2   1.43457e2

-8.29807e2   -2.53615e2   -2.63092e2   -4.04982e1   6.86222e1

$\underbrace{\qquad\qquad\qquad\qquad\qquad\qquad\qquad\qquad\qquad\qquad\qquad}$

Row 2

2.22616e2   -4.90572e3   -1.00186e3   -7.15575e0   4.12691e2   -3.84770e2

1.35749e3   1.53740e3   5.67946e2   -7.10643e2   -3.48538e2   3.21057e2

-5.30251e2   5.34130e1   -9.56373e1   6.26606e1   -1.24606e1

-5.77303e4   -4.40870e4   -6.30928e0   -3.46857e4   -7.05868e3   -6.70158e2

-1.45717e4   -1.06601e4   -1.66914e2   3.84800e2   4.27050e2   6.49161e0

4.71910e2   2.17085e1   1.36010e2   1.15349e0   -7.00744e0

-8.96817e1   -4.97541e1   6.04479e0   -6.53553e-1   -1.29007e0   -2.82732e-2

-2.39179e0   -1.77339e0   -7.33036e-2   4.60049e-2   4.08249e-2   1.65662e-2

8.67164e-2   5.16909e-2   3.48956e-2   1.93479e-2   -1.46204e-2

-8.52011e1   -5.09812e1   5.87131e0   6.82095e-1   -7.50560e-1   -6.96289e-1

-1.62015e0   -1.18638e0   -2.51284e-2   3.16516e-2   2.63812e-2   1.49417e-2

6.13472e-2   4.28639e-2   2.54808e-2   1.69775e-2   -1.17656e-2

-4.89945e2   -3.65155e2   4.31686e1   1.16514e1   -6.14972e-1   -4.66819e-1

-3.00847e0   -6.95477e-1   3.69664e-1   -1.02637e-1   -7.11738e-2   1.22578e-1

-2.80760e-2   1.52510e-1   2.41076e-2   8.38884e-2   -3.88365e-2

3.81422e2   2.95671e2   -3.43787e1   -1.78622e1   -1.99480e-1   4.48511e-1

-4.30597e-1   -2.49852e0   -4.17271e-1   1.01103e-1   7.85546e-2   -9.58420e-2

5.68715e-2   -1.13440e-1   -5.86166e-3   -6.50812e-2   2.74218e-2

1.58796e3   1.25337e3   -1.00880e2   -4.95560e2   -1.27063e1   5.00807e0

-2.74278e1   -2.26532e1   -7.75444e0   -3.07213e-1   6.41952e-2   -1.60489e-1

-4.15923e-1   -7.55237e-1   -1.38296e-1   -3.15868e-1   1.40577e-1

-6.50763e3   6.54147e3   3.94127e2   3.12976e1   -1.14219e2   -3.17682e0

-2.46553e2   -1.81043e2   -4.15778e0   -9.55558e0   9.39474e0   4.37996e0

1.30819e1   3.57632e0   4.95820e0   -3.53127e-1   -1.02119e0

1.98133e3   -1.07056e4   2.20907e3   -1.54432e3   2.02038e2   -7.27440e-1

4.36118e2   3.35230e2   2.24180e1   -2.80435e1   -2.76093e1   5.57476e0

-3.51725e1   -6.61745e0   -1.02175e1   3.29884e-1   1.76017e0

-1.67144e4   3.06588e3   9.46778e1   7.65938e2   -1.48833e2   -5.32347e0

-3.21270e2   -2.40013e2   -8.29345e0   8.97544e0   1.31075e1   -9.12367e0

2.23065e1   5.73616e0   7.30589e0   9.97463e-2   -1.53802e0

3.82787e2   -3.30635e2   -2.63489e3   2.02624e2   -3.67322e1   6.03039e0

-7.92899e1   -6.87991e1   -1.35575e1   1.88407e1   5.29614e0   -7.19306e0

-2.61179e0   8.94441e-1   1.78975e0   2.71070e-1   -2.23982e-1

-3.62200e3   -1.39242e3   2.00181e3   -1.90224e3   7.69126e0   -2.04382e-1

1.66023e1   1.67395e1   4.01861e0   -1.11726e1   -3.43161e0   4.26481e0

-6.14798e0   -1.84894e1   3.61223e0   -8.43531e-2   1.21722e-1

-8.13921e3   -9.83880e3   2.80868e3   -5.95949e2   5.67584e1   -3.27628e0

1.22518e2   9.60949e1   9.42092e0   -8.89398e0   -5.52364e0   2.47021e0

-9.16720e0   -6.10083e0   -2.03132e1   1.46755e-1   3.75213e-1

-1.97888e3   3.24868e3   -1.40270e3   -2.84442e3   -6.69323e1   7.08851e0

-1.44480e2   -1.13095e2   -1.28464e1   6.43206e0   4.12505e0   -1.63816e0

6.65259e0   8.80035e-1   1.95008e0   -2.13870e1   4.92849e-1

4.60768e2   6.31139e2   8.72154e2   1.05599e3   1.62752e1   -3.66577e0

3.51315e1   2.92859e1   5.59118e0   -4.01960e0   -1.04473e0   1.58754e0

-1.72108e0   1.52147e-2   -3.19137e-1   -8.48886e-1   -2.13009e1]

B Matrix

[1.29674e-1   1.13568e-1   1.11324e0   5.16370e-1

-1.20641e0   9.55107e-1   -2.72098e0   -8.99678e-1

-8.96470e0   3.68070e0   -3.49988e0   8.56021e-1

6.62556e-1   -5.84756e0   1.89355e-1   1.34022e0

-3.87728e0   -3.26135e0   5.99098e0   -6.00364e0

-3.21274e0   -6.03087e0   6.23437e0   -4.06676e0

-2.55223e1   -5.27942e1   4.70611e1   -3.33210e0

1.89339e1   5.23846e1   -3.87782e1   -1.08084e0

-2.02993e1   6.76094e2   -1.77869e2   -6.88467e1

-1.09886e3   8.22379e2   -2.02415e3   -6.18874e2

-1.40667e3   5.74499e2   1.99734e3   1.09470e3

$$\begin{array}{cccc}
-1.73200e2 & -2.05103e2 & -1.78074e3 & -8.06422e2 \\
1.77662e3 & -7.46668e2 & 7.32626e2 & -1.99026e2 \\
-1.09326e3 & 8.50472e2 & -3.18401e2 & 4.16735e1 \\
-5.91203e2 & -3.65534e1 & 3.88125e2 & 3.07534e2 \\
3.32767e2 & 6.55729e2 & -2.55542e2 & -3.62659e2 \\
-3.64031e2 & -1.37986e2 & -1.70413e2 & 8.81838e1]
\end{array}$$

C Matrix

$$\begin{array}{cccccc}
[1.36316e5 & 7.56272e4 & -2.24253e2 & 5.77308e4 & -1.41081e4 & 1.11749e2 \\
-2.93267e4 & -2.18777e4 & -1.19697e3 & 5.11415e2 & 6.26959e2 & 1.15642e2 \\
1.07954e3 & 4.19320e2 & 3.78149e2 & 1.15555e2 & -1.21816e2 &
\end{array}$$

$\underbrace{\qquad\qquad\qquad\qquad\qquad\qquad}$
Row 1

$$\begin{array}{cccccc}
7.56272e4 & 1.64461e5 & 4.90745e3 & 4.40867e4 & -9.35613e3 & 5.52694e2 \\
-1.86933e4 & -1.43172e4 & -1.30484e3 & 8.43399e2 & 4.81969e2 & -1.43452e2 \\
8.29827e2 & 2.53620e2 & 2.63099e2 & 4.04978e1 & -6.86237e1 &
\end{array}$$

$\underbrace{\qquad\qquad\qquad\qquad\qquad\qquad}$
Row 1

$$\begin{array}{cccccc}
-2.24253e2 & 4.90745e3 & 1.00193e3 & 6.25884e0 & -4.12533e2 & 3.84740e2 \\
-1.35715e3 & -1.53709e3 & -5.67881e2 & 7.10550e2 & 3.48513e2 & -3.21021e2 \\
5.30206e2 & -5.34163e1 & 9.56291e1 & -6.26615e1 & 1.24614e1 &
\end{array}$$

$$\begin{array}{cccccc}
5.77308e4 & 4.40867e4 & 6.25884e0 & 3.46863e4 & 7.05893e3 & 6.70114e2 \\
1.45723e4 & 1.06606e4 & 1.66971e2 & -3.84802e2 & -4.27054e2 & -6.49210e0 \\
-4.71913e2 & -2.17078e1 & -1.36012e2 & -1.15349e0 & 7.00793e0]
\end{array}$$

125

Bibliography

[1] ABKOWITZ, M. A. *Stability and Motion Control of Ocean Vehicles.* MIT Press, 1969.

[2] ALBERTOS, P., AND SALA, A. *Multivariable Control Systems: An Engineering Approach*, 1st ed. Springer, 2003.

[3] ANDRUS, M. Rtds notional e-ship model technical guide-version 2.1a. Tech. rep., FSU - Center for Advanced Power Systems, July 2006.

[4] BASH, M., ET AL. A medium voltage dc testbed for ship power system research. In *IEEE Electric Ship Technologies Symposium* (Baltimore MD, Apr. 2009).

[5] BECK, R., AND MAGEE, A. Time-domain analysis for predicting ship motions. In *The Dynamics of Marine Vehicles and Structures in Waves.* Elsevier Science Ltd, 1991.

[6] BERNITSAS, M., RAY, D., AND KINLEY, P. Kt, kq and efficiency curves for the wageningen b-series propellers. Tech. Rep. 237, The University of Michigan. Dept. of Naval Architecture, May 1981.

[7] BISHOP, R., PRICE, W., AND TAM, P. Hydrodynamic coefficients of some heaving cylinders of arbitrary shape. *International Journal for Numerical Methods in Engineering 13* (1978), 17–33.

[8] CALIFANO, A., AND STEEN, S. Analysis of different propeller ventillation mechanisms by means of rans simulations. In *First International Symposium on Marine Propulsors* (Trondheim, Norway, June 2009).

[9] CHALFANT, J., CHRYSSOSTOMIDIS, C., AND ANGLE, M. Study of parallel ac and dc electrical distribution in the all-electric ship. In *Proceedings of the 2010 Grand Challanges in Modeling and Simulation* (Ottawa, Canada, Nov. 2010).

[10] CHEN, L., MIN, Y., XU, F., AND WANG, K.-P. A continuation-based method to compute the relevant unstable equilibrium points for power system transient stability analysis. *IEEE Transactions on Power Systems 24*, 1 (Feb. 2009), 165–172.

[11] CHOWDHURY, S., AND CROSSLY, P. *Microgrids and Active Distribution Networks*. Institution of Engineering and Technology, July 2009.

[12] CLARKE, F. Stability analysis of sliding-mode feedback control. *Control and Cybernetics 38*, 4 (2009), 1169–1192.

[13] DEGROOT, M., AND SCHERVISH, M. *Probability and Statistics*, 3rd ed. Addison-Wesley, Boston, MA, 2002.

[14] DENIS, M. S., AND PIERSON, W. On the motion of ships in confused seas. *SNAME Transl. 61* (1953).

[15] DOERRY, N., AND FIREMAN, H. Designing all electric ships. In *Proceedings of the Ninth International Marine Design Conference* (Ann Arbor, MI, May 2006).

[16] DOUGAL, R. Design tools for electric ship systems. In *Electric Ship Technologies Symposium* (July 2005), IEEE.

[17] ENGELBERG, S. Limitations of the describing function for limit cycle prediction. *IEEE Transactions of Automatic Control 47*, 11 (2002), 1887–1890.

[18] EPPS, B., CHALFANT, J., KIMBALL, R., TECHET, A., FLOOD, K., AND CHRYSSOSTOMIDIS, C. Openprop: An open-source parametric design and analysis tool for propellers. Tech. rep., Massachusetts Institute of Technology, 2009.

[19] ERICSEN, T. Electric ship research and development consortium background, 2007. http://esrdc.caps.fsu.edu/index.html.

[20] ERSELCAN, I. A frequency domain strip theory applied to the seakeeping of the zumwalt-class destroyer. Master's thesis, Massachusetts Institute of Technology, May 2010.

[21] ESRDC, May 2010. The 2010 ESRDC Annual Team Meeting.

[22] FOSSEN, T. I. A nonlinear unified state-space model for ship maneuvering and control in a seaway. *Journal of Bifurication and Chaos* (Sept. 2005).

[23] FOSSEN, T. I., AND FJELLSTAD, O.-E. Nonlinear modelling of marine vehicles in 6 degrees of freedom. *Journal of Mathematical Modelling of Systems 1*, 1 (1995).

[24] FRANK, W., AND SALVESEN, N. The frank close-fit ship motions computer program. Tech. Rep. 3289, NSRDC, June 1970.

[25] FRIEDMAN, N. *U.S Destroyers. An Illustrated Design History*. Naval Institute Press, 2004.

[26] G E MARINE. *LM2500 Marine Gas Turbine*, 2006.

[27] GELB, A. *Multiple-Input describing functions and nonlinear systems*. McGraw Hill Inc., 1968.

[28] GREYTAK, M. High performance path following for marine vehicles using azimuthing podded propulsion. Master's thesis, Massachusetts Institute of Technology, Feb. 2006.

[29] HOLMES, M. *Introduction to Perturbation Methods*. Springer-Verlag New York, Inc., 1995.

[30] HONG, Y. *Prediction of Motions of SWATH Ships in Following Seas*. David W Taylor Naval Ship Research and Development Center, 1981.

[31] HOVER, F., AND TRIANTAFYLLOU, M. System design for uncertainty: Concepts, equations, and examples, 2009. Lecture Notes.

[32] IKEDA, Y., HIMENO, Y., AND TANAKA, N. Components of roll damping of ship at forward speed. *Journal of the Society of Naval Architecture Japan 143* (1978).

[33] JOHNSON, M., AND MORADI, M. *PID Control: New Identification and Design Methods.* Springer, 2005.

[34] JONG, B. Computation of the hydrodynamic coefficients of oscillating cylinders. Tech. Rep. 145, Netherlands Research Center TNO, 1973.

[35] JULIAN, A., AND CUZNER, R. Design, modeling and stability analysis of an integrated shipboard dc power system. In *Electric Ship Technologies Symposium* (Baltimore MD, Apr. 2009), IEEE, pp. 428–432.

[36] KAPPOS, E. Robust multivariable control for the f100 engine. Master's thesis, Massachusetts Institute of Technology, 1983.

[37] KERREBROCK, J. L. *Aircraft Engines and Gas Turbines.* The MIT Press, Apr. 1992.

[38] KERWIN, J. 13.04 lecture notes: Hydrofoils and propellers, 2001. Lecture Notes.

[39] KHAHIL, H. *Nonlinear Systems*, 3rd ed. Prentice Hall, 2002.

[40] KRAUSE, P. C. *Analysis of Electric Machinery.* Institue of Electrical and Electronics Engineering, Jan. 1995.

[41] LEVEDAHL, W. Integrated electrical power supply system for propulsion and service control. United State Patent Dept., Nov. 1997. 5684690.

[42] LEWIS, E. V. Volume iii motions in waves and controllability. In *Principles of Naval Architecture*, 2nd ed. Society of Naval Architects and Marine Engineer, 1990.

[43] LIPO, T., AND KRAUSE, P. Stability analysis of a rectifier-inverter induction motor drive. *IEEE Transactions on Power Apparatus and Systems*, 1 (Jan. 1969).

[44] LIU, J. *Monte Carlo Strategies in Scientific Computing.* Springer, 2004.

[45] LOOP, B., SUDHOFF, S., ZAK, S., AND ZIVI, E. Estimating regions of asymptotic stability of power electronics systems using genetic algorithms. *IEEE Transactions on Control Systems Technology* (2009).

[46] LORENZ, R. D., AND HAINES, L. P. *Understanding Modern Power Conversion*, 3rd ed. University of Wisconsin, Jan. 2000.

[47] LOUKAKIS, T. A. Computer aided prediction of seakeeping performance in ship design. Tech. Rep. MA-RD-900-71-8, Massachusetts Institute of Technologoy, Dec. 1970.

[48] MALESCI, C. Use of seakeeping simulation capabilities in the preliminary phase of the design of multihull vessels. Master's thesis, Massachusetts Institute of Technology, June 2006.

[49] MARDEN, M., CHRYSSOSTOMIDIS, C., AND KARNIDAKAS, G. Mit model of the purdue dc testbed. Tech. rep., Massachusetts Institute of Technology, 2009.

[50] THE MATHWORKS. *Simulink User's Guide: Accelerating Modes*, 2010. http://www. mathworks.com/access/helpdesk/help/toolbox/simulink/simulink_product_page. html.

[51] MENARD, P. Prediction of performance and maneuvering dynamics for marine vehicles applied to ddg-1000. Master's thesis, Massachusetts Institute of Technology, May 2010.

[52] MOHAN, N., UNDELAND, T., AND ROBBINS, W. *Power Electronics, Converters, Applications and Design*. John Wiley and Sons Inc., 1995.

[53] MPT CONSULTANCY. *Gas Turbine Electric Drive LNG Carrier*, 2004. http://www. mptconsult.com/LNGC%20GTG.htm.

[54] NEWMAN, J. Second-order slowly-varying forces on vessels in irregular waves. In *International Symposium Dynamics of Marine Vehicles and Structures in Waves* (London UK, Apr. 1974).

[55] NSWC. *ASSET User's Manual*, 1990.

[56] O.M. FALTINSEN, K.J. MINSAAS, N. L., AND SKJORDAL, S. Prediction of resistance and propulsion of a ship in a seaway. In *Proceedings of the Thirteenth Symposium on Naval Hydrodynamics* (Tokyo, 1980).

[57] PETERSON, H., AND KRAUSE, P. A direct- and quadrature-axis representation of parallel ac and dc power system. *IEEE Transactions on Power Apparatus and Systems 85*, 3 (1966).

[58] PRATT AND WHITNEY. *Product:Military:F100*, 2010. `http://www.pw.utc.com/Products/Military/F100`.

[59] PREMPRANEERACH, P., KIRTLEY, J., CHRYSSOSTOMIDIS, C., TRIANTAFYLLOU, M., AND KARNIDAKAS, G. Design of the all-electric ship: Focus on integrated power system coupled to hydrodynamics. Tech. rep., Massachusetts Institute of Technology, 2008.

[60] RUBIS, C. Braking and reversing ship dynamics. *Naval Engineering Journal 82*, 1 (1970), 65–76.

[61] SALVESEN, N. Second-order steady-state forces and moment on surface ships in oblique regular waves. In *The Dynamics of Marine Vehicles and Structures in Waves*. Elsevier Science Ltd, 1975, pp. 212–226.

[62] SALVESEN, N., TUCK, E., AND FALTINSEN, O. Ship motions and sea loads. *SNAME Transl. 78* (1970).

[63] SCHANK, ET AL. *Acquisition and Competition Strategy for the DD(X). The U.S. Navy's 21st Century Destroyer.* The RAND Corporation, 2006.

[64] SCHMITT, K., AND TRIANTAFYLLOU, M. Modeling and simulation of the all electric ship in random seas including supplemental material. Tech. rep., Massachusetts Institute of Technology, 2010.

[65] SMOGELI, O. N. *Control of Marine Propellers. From Normal to Extreme Conditions.* PhD thesis, Norwegian University of Science and Technology, Sept. 2006.

[66] SOULTATISI, C. Systems modeling for electric ship design. Master's thesis, Massachusetts Institute of Technology, June 2004.

[67] STETTLER, J. W. *Steady and Unsteady Dynamics of an Azimuthing Podded Propulsor Related to Vehicle Maneuvering.* PhD thesis, Massachusetts Institute of Technology, May 2004.

[68] SUDHOFF, S., ET AL. Admittance space stability analysis of power electronic systems. *IEEE Transactions on Aerospace and Electronic Systems 36*, 3 (July 2000).

[69] TRIANTAFYLLOU, M. 2.22 design principles for ocean vehicles, 2010. Lecture Notes.

[70] TRIANTAFYLLOU, M., AND HOVER, F. Maneuvering and control of marine vehicles, 2002. Lecture Notes.

[71] VUGTS, J. The hydrodynamic coefficients for swaying, heaving and rolling cylinders in a free surface. Tech. Rep. 112S, Netherlands Research Center TNO, 1968.

[72] WELCH, P. The use of fast fourier transform for the estimation of power spectra: A method based on time averaging over short, modified periodograms. *IEEE Transactions on Audio Electroacoustics AU-15* (1967), 70–73.

[73] WELSH, M., Jul 2010. Interview Regarding the Challenges and Advantages of an All Electric Ship.